a-Si:H/c-Si heterojunction front- and back contacts for silicon solar cells with p-type base

Von der Fakultät Informatik, Elektrotechnik und Informationstechnik
der Universität Stuttgart zur Erlangung der Würde eines
Doktor-Ingenieurs (Dr.-Ing.) genehmigte Abhandlung

Vorgelegt von

Philipp Johannes Rostan

geboren am 19.06.1975 in Stuttgart

Hauptberichter: Prof. Dr. rer. nat. habil. J. H. Werner
Mitberichter: Prof. Dr.-Ing. N. Frühauf

Tag der Einreichung: 24.06.2008
Tag der mündlichen Prüfung: 21.12.2009

Institut für Physikalische Elektronik der Universität Stuttgart
2010

Contents

Abstract

This thesis reports on low temperature amorphous silicon back and front contacts for high-efficiency crystalline silicon solar cells with a p-type base. The back contact uses a sequence of intrinsic amorphous (i-a-Si:H) and boron doped microcrystalline (p-μc-Si:H) silicon layers fabricated by Plasma Enhanced Chemical Vapor Deposition (PECVD) and a magnetron sputtered ZnO:Al layer. The back contact is finished by evaporating Al onto the ZnO:Al and altogether prepared at a maximum temperature of 220 °C. Analysis of the electronic transport of mobile charge carriers at the back contact shows that the two high-efficiency requirements *low back contact series resistance* and *high quality c-Si surface passivation* are in strong contradiction to each other, thus difficult to achieve at the same time. The preparation of resistance- and effective lifetime samples allows one to investigate both requirements independently. Analysis of the majority charge carrier transport on complete Al/ZnO:Al/a-Si:H/c-Si back contact structures derives the resistive properties. Measurements of the effective minority carrier lifetime on a-Si:H coated wafers determines the back contact surface passivation quality. Both high-efficiency solar cell requirements together are analyzed in complete photovoltaic devices where the back contact series resistance mainly affects the fill factor and the back contact passivation quality mainly affects the open circuit voltage. The best cell equipped with a diffused emitter with random texture and a full-area a-Si:H/c-Si back contact has an independently confirmed efficiency $\eta = 21.0$ % with an open circuit voltage $V_{\mathrm{oc}} = 681$ mV and a fill factor $FF = 78.7$ % on an area of 1 cm^2. An alternative concept that uses a simplified a-Si:H layer sequence combined with Al-point contacts yields a confirmed efficiency $\eta = 19.3$ % with an open circuit voltage $V_{\mathrm{oc}} = 655$ mV and a fill factor $FF = 79.5$ % on an area of 2 cm^2. Analysis of the internal quantum efficiency shows that both types of back contacts lead to effective diffusion lengths in excess of 600 μm. An extended fill factor analysis shows that fill factor limitations

for the full-area a-Si:H/c-Si contacts result from non-ideal diode behavior, ascribed to the injection dependence of the heterojunction interface recombination velocity. Analysis of the external quantum efficiency under back side illumination with different bias light intensities delivers the effective surface recombination $S_{\mathrm{eff}}(\Phi)$ in dependance of the illumination intensity Φ.

The front contact (emitter) uses a sequence of intrinsic and phosphorous doped amorphous silicon layers together with a ZnO:Al or a SnO_2:In layer and an Al front contact grid. The emitter is prepared at a maximum temperature of 220 °C. Measurements of the minority carrier lifetime on symmetric i/n-a-Si:H coated wafers judge the emitter passivation quality. The best solar cells that use a thermal oxide back side passivation with Al-point contacts and flat a-Si:H emitters have open circuit voltages up to 683 mV and efficiencies up to 17.4 %. The efficiency of such devices is limited by a low short circuit current due to the flat front side. Using the same back contact structure with random pyramid textured wafer front sides and a-Si:H emitters yields open circuit voltages up to 660 mV and efficiencies up to 18.5 %, so far limited by a relatively low fill factor $FF \leq 74.3$ %. Analysis of the external quantum efficiency underlines the excellent surface passivation properties of the amorphous emitter.

Combining both, amorphous front- and back contacts yields p-type heterojunction solar cells completely fabricated at temperatures below 220 °C. The best devices reach an open circuit voltage $V_{\mathrm{oc}} = 678$ mV and an efficiency $\eta = 18.1$ % with random textured wafers, limited by low fill factors $FF \approx 75$ %.

Besides the cell fabrication and characterization, this thesis reveals that the inherent a-Si:H/c-Si band offset distribution with a low conduction band offset and a large valence band offset is disadvantageous for p-c-Si heterojuntion solar cells if compared to their n-c-Si counterparts. A calculation of the saturation current densities of the cell's emitter, bulk and back contact demonstrates that the n-a-Si:H/p-c-Si emitter suffers from a low built-in potential. Modelling of the back contact based on the charge carrier transport equations shows that the insertion of an i-a-Si:H layer with a thickness $d \geq 3$ nm (that is mandatory for a high surface passivation quality) leads to a series resistance that is critical for usage in a solar cell. The model mainly ascribes the high back contact resistance to the large valence band offset at the heterojunction.

Zusammenfassung

Die vorliegende Arbeit untersucht Niedertemperatur Front- und Rückkontakte aus amorphem Silizium für Hocheffizienzsolarzellen auf p-Typ kristallinem Silizium Basismaterial. Als Rückkontakt findet eine Sequenz aus intrinsischen und Bor dotierten amorphen und mikrokristallinen Siliziumschichten hergestellt mittels Plasma Enhanced Chemical Vapor Deposition (PECVD) Anwendung. Die Fertigstellung des Kontakts erfolgt über die Kathodenzerstäubung einer hoch leitfähigen ZnO:Al Schicht und Aufdampfen von Aluminium. Der Kontakt ist insgesamt bei Temperaturen unter 220 °C hergestellt. Eine Analyse des elektrischen Transports freier Ladungsträger am Rückkontakt offenbart, dass die zwei Anforderungen für hohe Solarzelleneffizienz *geringer Serienwiderstand* und *gute Oberflächenpassivierung* in starkem Widerspruch zueinander stehen und daher nur schwierig gleichzeitig zu erreichen sind. Die Präparation von Widerstands- und Lebensdauerproben ermöglicht es, beide Anforderungen getrennt zu untersuchen. Der elektrischen Widerstand wird an kompletten Al/ZnO:Al/a-Si:H/c-Si Rückkontaktstrukturen untersucht. Die Passivierqualität des Rückkontakts wird bestimmt durch die Rekombination von Minoritätsladungsträgern an der a-Si:H/c-Si Grenzfläche und untersucht an Hand von Messungen der effektiven Lebensdauer an a-Si:H beschichteten Wafern. Beide Hocheffizienz-Anforderungen gemeinsam werden an kompletten Solarzellen analysiert, wobei der elektrische Widerstand des Rückkontakts vor allen Dingen den Füllfaktor bestimmt, während die Qualität der c-Si Oberfläche vor allem die Leerlaufspannung beeinflusst. Die beste Zelle ausgestattet mit einem diffundierten Hocheffizienzemitter, einer Pyramidentextur und einem ganzflächigen a-Si:H/c-Si Rückkontakt erreicht einen bestätigten Wirkungsgrad $\eta = 21$ % mit einer offenen Klemmspannung $V_{\mathrm{oc}} = 681$ mV und einem Füllfaktor $FF = 78{,}7$ % auf einer Fläche von 1 cm^2. Ein alternatives Rückkontaktkonzept mit einer vereinfachten a-Si:H Schichtsequenz in Kombination mit Aluminium Punktkontakten erreicht einen bestätigten

Wirkungsgrad η = 19,3 % mit einer offenen Klemmspannung V_{oc} = 655 mV und einem Füllfaktor FF = 79,5 % auf einer Fläche von 2 cm^2. Die Analyse der internen Quanteneffizienz zeigt, dass beide Rückkontaktstrukturen zu einer effektiven Diffusionslänge von mehr als 600 μm führen. Eine tiefgreifende Untersuchung der Solarzellenkennlinie deckt auf, dass die Limitierung des Füllfaktors bei ganzflächigen a-Si:H/c-Si Rückkontakten durch eine Nichtidealität der Diode, verursacht durch die Injektionsabhängigkeit der Grenzflächen-Rekombinationsgeschwindigkeit, entsteht. Messungen der externen Quantenausbeute unter rückseitiger Beleuchtung mit variierenden Beleuchtungsstärken bestätigen diese Injektionsabhängigkeit.

Die Frontseite (Emitter) verwendet eine Sequenz von intrinsischem und Phosphor dotiertem amorphen Silizium zusammen mit einer ZnO:Al oder einer SnO_2:In Schicht und einem Aluminium Kontaktgitter, ebenfalls komplett bei Temperaturen unter 220 °C hergestellt. Die Oberflächen-Passivierqualität des Emitters wird an Hand von symmetrischen i/n-a-Si:H beschichteten Wafern untersucht. Die besten Solarzellen, ausgerüstet mit einer thermischen Oxidpassivierung und Al Punktkontakten auf der Rückseite sowie untexturierten a-Si:H Emittern, erreichen eine Leerlaufspannung V_{oc} = 683 mV und einen Wirkungsgrad FF = 17,4 %. Der Wirkungsgrad dieser Zellen ist begrenzt durch eine geringe Stromdichte bedingt durch die flache Frontseite. Derselbe Rückkontakt und ein a-Si:H Emitter mit Pyramidentextur erreicht eine offene Klemmspannung V_{oc} = 660 mV und einen Wirkungsgrad η = 18,5 %, begrenzt durch einen niedrigen Füllfaktor FF = 75 %. Die Analyse der externen Quanteneffizienz (EQE) bestätigt die exzellente Oberflächenpassivierung des a-Si:H Emitters.

Die Kombination der a-Si:H Front- und Rückkontakte ermöglicht die Herstellung kompletter Heterostruktur-Niedertemperatursolarzellen auf p-Typ c-Si Basismaterial. Die besten Bauelemente erreichen eine offene Klemmspannung von $V_{\mathrm{oc}} = 678mV$ und einen Wirkungsgrad η = 18,1 % auf Wafern mit Pyramidentextur, begrenzt durch einen niedrigen Füllfaktor von $FF \approx 75$ %.

Neben der Zellpräparation zeigt diese Dissertation inhärente Nachteile von Heterostruktur-Solarzellen auf kristallinem p-Typ- im Vergleich zu n-Typ Basismaterial auf. Die Berechnung der Sättigungsströme die in Emitter, Basis und Rückkontakt auftreten verdeutlicht, dass a-Si:H Emitter auf p-Typ c-Si unter einer geringeren eingebauten Spannung als ihre n-Typ c-Si Pendants leiden. Die Modellierung des Rückkontakts, basierend auf den Gleichungen des Ladungsträgertransportes,

verdeutlicht, dass die für eine sehr gute Rückseitenpassivierung zwingend erforderliche i-a-Si:H Schicht mit einer Dicke von mehr als 3 nm zu einem Serienwiderstand führt, der bereits kritisch ist. Der Serienwiderstand ist dabei vor allem auf die Banddiskontinuität im Valenzband an der a-Si:H/p-c-Si Grenzfläche zurückzuführen.

Chapter 1

Introduction

1.1 Motivation

Solar cells based on boron doped, *p-type* crystalline silicon (c-Si) represent the vast majority on today's photovoltaic (PV) device market. However, the efficiencies of industrially fabricated p-c-Si devices are rather low if compared to laboratory cells using a more sophisticated device structure. For mono-crystalline Si, as an example, the common industrial efficiency is around 17-18 % whereas efficiency in research surpasses 20 %. However, most necessary process technologies to reach such high efficiencies as for example photolithography are not profitably transferable to industrial scale mass production. Hence, an important area of today's research and also a goal of this PhD thesis is to design new *industrially applicable* and *cost-effective* solar cell processes that have the potential to increase the efficiency of industrial devices.

In the 1990ies, the company Sanyo developed a promising new member of the PV device family: The Heterojunction solar cell with Intrinsic Thin layer (HIT) [1]. The device bases on a phosphorous doped *n-type* mono-crystalline Si wafer equipped with amorphous Si front and back contacts. Such devices reach efficiencies of more than 20 % with open circuit voltages in excess of 710 mV even in the industrial mass production [2]. Figure 1.1 compares Sanyo's n-type HIT concept with a state of the art p-type industrial c-Si solar cell. Originally, Sanyo deposited the doped amorphous Si layers directly on the wafer. It turned out that the doped layers cause a high defect density at the surface and a high surface recombination

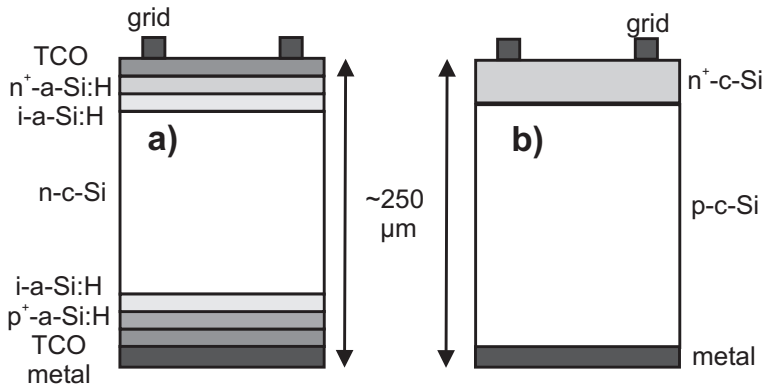

Fig. 1.1: (a) Sanyo's n-type solar cell concept with a-Si:H heterojunctions that form emitter (top) and back contact (bottom) of the device. (b) Sketch of a p-type c-Si solar cell according to the status quo in the photovoltaic industry. The device has a diffused n-type front electrode (emitter) and a p-type base. The back contact is formed by a full area metallization with Al.

velocity too [1]. To reach very high efficiencies, Sanyo integrated a thin intrinsic interlayer to passivate the c-Si surface. Since 1997 Sanyo has been fabricating HIT solar cell modules in mass production with *module* efficiencies up to 17 % that range among the highest in the world [3]. Several research groups have tried to adapt Sanyo's concept of a-Si:H/c-Si heterojunctions from phosphorous to boron doped wafers. It turned out that, for p-c-Si, the fabrication of an efficient a-Si:H *back contact* is much more challenging than that of an a-Si:H *emitter*. Jensen et al. achieved an efficiency η of about $\eta = 14$ % with a n-a-Si:H emitter on a non-textured wafer with an Al back contact [4]. Von Maydell et al. reached $\eta = 17.1$ % with a textured front side and a p-a-Si:H/Al back contact [5]. Even Sanyo offers in a promotion leaflet a p-type HIT solar cell without specified efficiency that indeed uses an a-Si:H emitter but a full area Al back contact just like a standard industrial pn-homojunction solar cell [6]. Only Wang et. al recently showed a p-type c-Si device with a-Si:H emitter *and* a-Si:H back contact fabricated by Hot-Wire Chemical Vapor Deposition HWCVD. They achieved an efficiency $\eta = 18.2$ % on a cell area of 1 cm^2 [7]. However, large scale a-Si:H fabrication with hot-wire CVD is not yet established and the industrial relevance of this technique is open. Sanyo achieves much higher efficiencies (on n-type base material) in particular due to a higher open

circuit voltage and a higher fill factor. This thesis ascribes both to the favorable a-Si:H/c-Si band offset distribution on n-type material.

1.2 Objectives

An important target of this thesis is to develop a high quality a-Si:H back contact for p-c-Si solar cells fabricated by Plasma Enhanced Chemical Vapor Deposition (PECVD) below deposition temperatures of 220 °C. The PECVD a-Si:H deposition process is a state of the art technique in the thin film solar cell- as well as flat panel display industry [8, 9]. Therefore, such a *back contact* is suitable for a rapid implementation into a c-Si production line with the clear opportunity to improve the final cell efficiency. In addition, this thesis aims to give a comprehensive understanding of the electronic properties of this back contact. Besides, another target is the development of a high-efficiency a-Si:H *emitter* (solar cell front side) for p-c-Si solar cells and to combine this emitter with the previously optimized a-Si:H back contact. The result is a p-type heterojunction c-Si device that is completely fabricated at low temperatures with a deposition technique that allows for a total inline processing.

1.3 Structure of this thesis

Chapter 2 presents the fundamentals of semiconducting photovoltaic devices and introduces the basics of amorphous and crystalline silicon heterostructures. The chapter also shows the influence of losses in heterojunction solar cells on their photovoltaic output parameters.

Chapter 3 introduces the measurement methods and the deposition techniques.

Chapter 4 focuses on the properties of amorphous silicon and its fabrication. It resumes the a-Si:H depositions on glass substrates with the goal to achieve a good layer homogeneity and, for the p-type layers, a high active doping.

Chapter 5 investigates the surface passivation of crystalline silicon with amorphous silicon. At first, it addresses the topic of wafer passivation with intrinsic a-Si:H. The chapter then develops an i/p-a-Si:H surface passivation scheme that is afterwards used in the solar cell back contact.

Chapter 6 develops (with the knowledge about a-Si:H/c-Si surface passivation

of Chapter 5) a back contact that has a low surface recombination velocity and, additionally, a low resistance.

Chapter 7 applies intrinsic and n-type a-Si:H depositions on p-type wafers to develop a high efficiency a-Si:H emitter (front side).

Chapter 8 combines both a-Si:H/c-Si emitter and a-Si:H/c-Si back contact to a complete p-type heterojunction solar cell.

Chapter 2

Solar cell fundamentals

This chapter summarizes the fundamentals of photovoltaic devices based on semiconductors. At first, it repeats the operating principles from the literature. The chapter then explains the special case of solar cells that use amorphous and crystalline silicon interfaces. Such devices form the basis of this thesis.

2.1 Operating principles

The physics of solar cells are described thoroughly in Refs. [10, 11]. The following summarizes those operating principles that are of importance in the present context. Photovoltaic solar cells convert the energy contained in the sunlight into electrical energy. The first device requirement is therefore:

(i) Absorption of the sunlight by the generation of mobile charge carriers.

This conversion takes place in the bulk of a semiconductor. Figure 2.1a shows the principle of this effect. Light with an energy equal or larger than the bandgap energy E_g of the semiconductor transfers its energy to an electron (full circle). By the absorption of the photon, the electron is moved from the valence band into the conduction band where it is a mobile charge carrier. The missing electron in the valence band is described as a positive charge carrier, a hole (open circle).

Without an additional component to separate the generated charge carriers, no net current can be extracted from the semiconductor and the electrons simply recombine into the energy E_V of the valence band after a certain time τ.

A second requirement for a working photovoltaic device is:

(ii) Collection of the generated charge carriers under short circuit conditions.

There are two concepts to achieve the separation of generated charge carriers: Selectivity of the contacts [12], or a pn-junction with built-in electric field. Solar cells in this thesis use selective interfaces as well as pn-junctions. Hence, the next part of this chapter presents a closer look at both.

Figure 2.1b shows a photovoltaic device that separates the generated charge carriers under short circuit conditions with the help of the selectivity of the contacts. It is Würfel's flat band solar cell [12,13]. Note that the cell is shown in Ref. [12] with open terminals, a case that will be discussed later in this section. The absorber

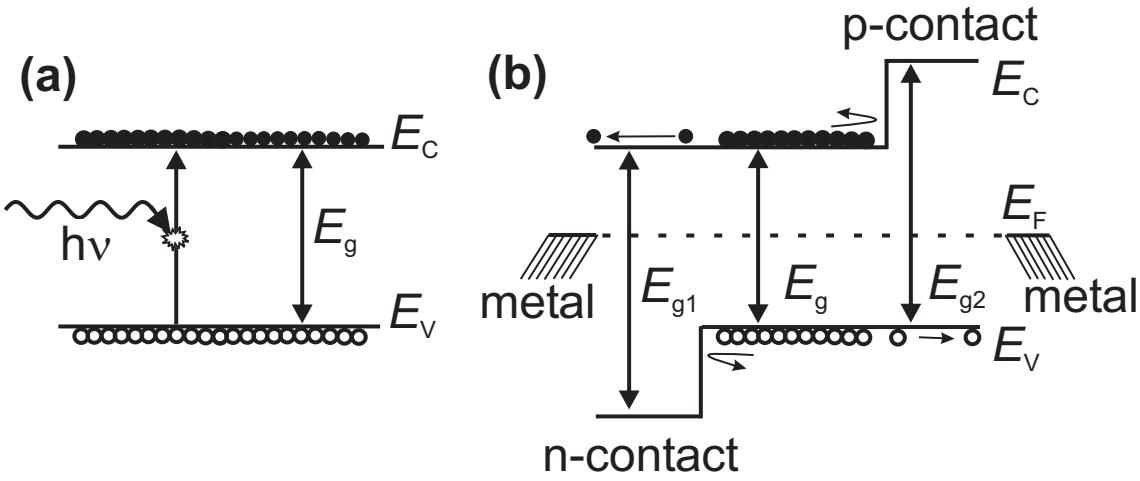

Fig. 2.1: (a) Sketch of the photon absorption in a semiconductor with bandgap E_g. The absorption causes the generation of mobile electrons (full circles) into the conduction band E_C and mobile holes (open circles) in the valence band E_V. (b) Sketch of a photovoltaic device equipped with two selective contacts (Würfel's flat band solar cell, redrawn according to Refs. [12, 13]). The absorber (bandgap E_g) is connected with semiconductors that form a selective contact for electrons (bandgap E_{g1}) and a selective contact for holes (bandgap E_{g2}).

with a bandgap E_g is equipped with two hetero-interfaces. On the left hand side (lhs), generated mobile electrons are collected in the n-contact whereas the holes are reflected. On the right hand side (rhs) of the device, the mobile holes are collected in the p-contact whereas the electrons are reflected. Thus, the built-in electric field of a pn-junction is *not* mandatory for the charge carrier collection under short circuit

conditions.

The third requirement for a solar cell is:

(iii) Formation of an open circuit voltage.

Figure 2.2a shows the flat band solar cell under illumination with open terminals. Note that the band diagram is modified from its original [12] according to Ref. [14]. Figure 2.2b depicts an illuminated pn-junction solar cell with open terminals. The

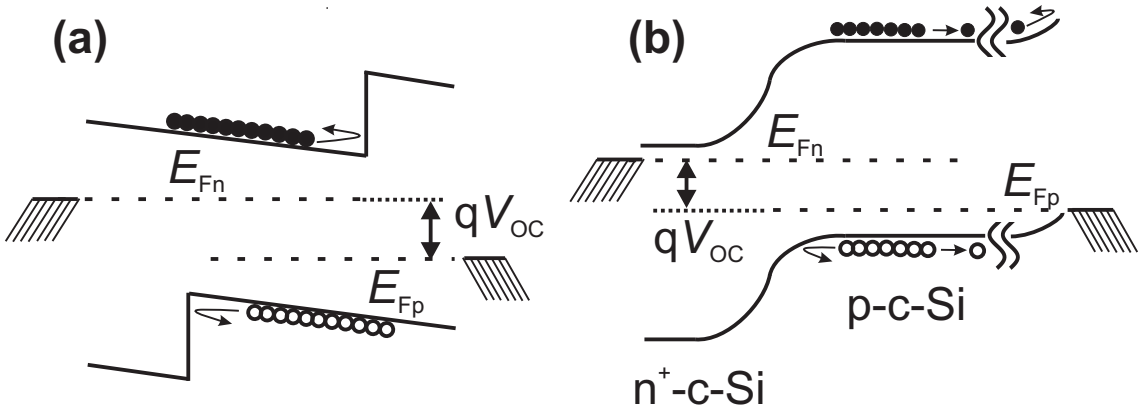

Fig. 2.2: (a) Sketch of the device with selective contacts under illumination and with open terminals. The Fermi level within the absorber splits into the quasi-Fermi levels for electrons E_{Fn} and holes E_{Fp}. The energetic difference between the quasi-Fermi levels is a measure for the cell's open circuit voltage. (b) Sketch of a standard industrial c-Si photovoltaic device with a pn-homojunction. The cell has a diffused n-type front electrode (emitter) and a p-type base. The back contact forms by a full area metallization with Al. Again the device is under illumination without connected load. The advantage of this structure is that the built-in electric field of the pn-junction enhances the carrier collection.

illumination induces a splitting of the Fermi level into the quasi-Fermi levels for holes E_{Fp} and for electrons E_{Fn}. The open circuit voltage created in the device is given by the difference of the Fermi-energy of electrons and holes.

Figure 2.2a indicates an inherent disadvantage of the flat band solar cell that emerges if it is connected to a load *and* charge carriers are extracted under a non-zero voltage: To contribute to the external current, the charge carriers have to diffuse *against* the arising electric field that hinders the electron transport towards the front contact. Thus, a fourth requirement for an efficient solar cell is:

(iv) Maintenance of charge carrier collection at the maximum power point.

This requirement is not easily fulfilled by the flat band cell. In the case of the pn-junction solar cell, Fig. 2.2b, the built-in electric field at the junction *enhances* the electron transport towards the front contact. Hence, *selectivity* of the contacts instead of a *pn-junction* is sufficient for the charge carrier separation, but the emerging electric field under operating conditions hampers the carrier collection. The efficiency of the flat band cell is therefore lower than that of the pn-junction solar cell - as long as the charge carrier lifetime and mobility are both lower than infinity.

Figure 2.2b shows a c-Si solar cell according to the status quo in the photovoltaic industry. Such a device consists of a moderately doped p-type absorber or base (thickness $d_\mathrm{b} = 100 - 300$ μm, doping concentration $N_\mathrm{A} \simeq 10^{16}$ cm^{-3}) and a heavily doped n-type emitter (thickness $d_\mathrm{e} \approx 0.5$ μm, doping concentration $N_\mathrm{D} \simeq 10^{19}$ cm^{-3}). The pn-junction is created by in-diffusion of phosphorous. The width of the space charge region inside the base is several hundred nm, i.e. 99 % of the device thickness is still electrically neutral. To obtain very high efficiencies, one has to pay much attention to passivate the cell's front- and back surface to reduce the surface recombination velocity S.

The emitter surface of industrial cells is passivated by amorphous silicon nitride a-$Si_{1-x}N_x$:H. In general, it forms the light-facing front side of the solar cell and is contacted with a metal grid front contact. The grid is optimized to cause as low shading as possible whilst allowing for a low device series resistance. On the back side of the device, the base is equipped with a full area Al-contact. The in-diffusion of Al into the base by a high temperature firing step creates a p^+-type doping of the c-Si back surface, the so-called Back Surface Field (BSF). The BSF repels minorities and thereby lowers the back surface recombination velocity. However, a metal back contact does not passivate the c-Si surface itself and is also not selective. Electrons that overcome the BSF and diffuse to the interface recombine at the back junction. Therefore, the back contact of an industrial c-Si solar cell is a recombination site that limits the cell efficiency. Hence, an industrial c-Si device has a *better charge carrier collection* than Würfel's flat band solar cell but a *worse charge carrier separation.*

Fig. 2.3a shows a solar cell that uses a pn-junction *and* a selective flat band Würfel-type Ohmic back contact. This device yields a better charge carrier separation than a pn-junction device with non-selective Ohmic Al back contact (Fig.

2.2b) and a better charge carrier collection than Würfel's flat band solar cell (2.2a). Thus, the combination of both, the contact *selectivity* and the *pn-junction* delivers

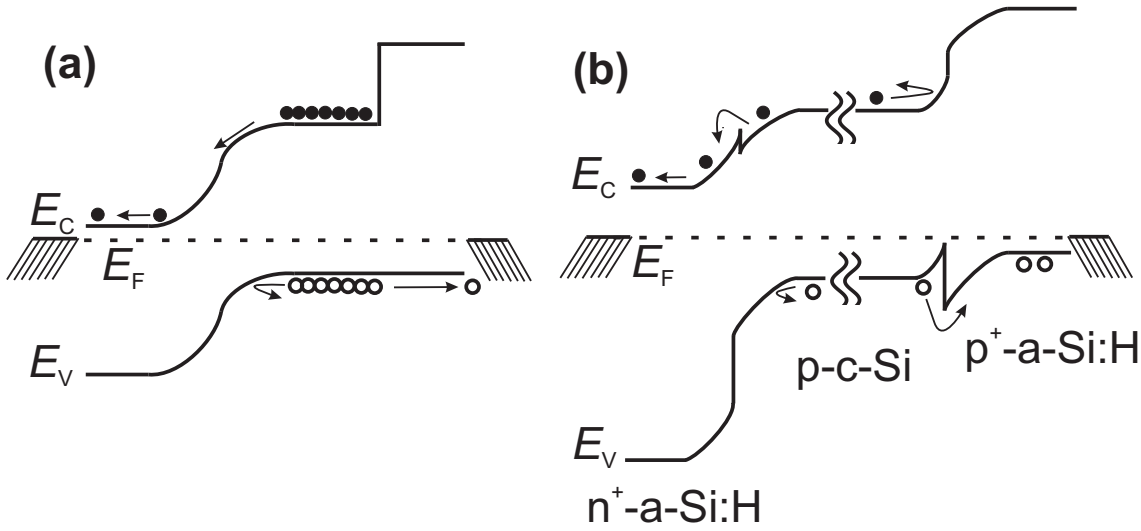

Fig. 2.3**:** (a) Photovoltaic device with pn-homojunction and selective back contact. Such a device is superior to a flat band solar cell due to an improved charge carrier collection and superior to a standard industrial pn-junction c-Si solar cell due to better charge carrier separation. (b) Heterojunction solar cell with a-Si:H front and back contacts that form selective interfaces for electrons (left hand side) and holes (right hand side).

an ideal photovoltaic device.

Figure 2.3b shows the concept of an a-Si:H/c-Si solar cell where heterojunctions are used as both, the rectifying front contact and the Ohmic back contact. The band discontinuities ΔE_C for the conduction band and ΔE_V for the valence band at both interfaces are caused by the different bandgap of c-Si ($E_{g,Si} = 1.12$ eV) and a-Si:H ($E_{g,a-Si:H} \approx 1.7$ eV) (comp. Fig.2.7). The front n-a-Si:H/p-c-Si contact (lhs) is similar to a pn-homojunction. Besides, it forms a selective n-contact because the band offset in the valence band hinders holes from entering into the a-Si:H emitter. The p^+-a-Si:H back contact forms a BSF, the electric field forces the electrons away from the interface and collects the holes. In addition, the band offset in the conduction band hinders the electrons from diffusing into the a-Si:H layer. The *inherent* disadvantages of this a-Si:H/c-Si solar cell if compared to the ideal solar cell from Fig. 2.3a are the band offset in the *conduction band* on the lhs (emitter) and the

band offset in the *valence band* on the rhs (back contact). These band offsets hinder the charge carrier transport of electrons across the front interface and holes across the rear interface. In particular, the large band offset in the valence band at the back contact makes the p-c-Si/p^+-a-Si:H interface apparently more suitable as a selective interface for *electrons* than for *holes*. Section 2.3 describes how I achieve the selectivity for holes at the back junction despite of this complication. Details about the a-Si:H/c-Si hetero-emitter are found in section 2.4. The next section summarizes in a general way the losses in the bulk and at the surface that occur in photovoltaic devices.

2.2 Losses in solar cells

There are losses in solar cells limiting the efficiency of, e.g., Si devices with a single bandgap to $\eta \approx 28$ % [15, 16]. It is thereby assumed that the impinging light on the solar cell corresponds to the AM1.5G spectrum of the sun. The most important losses of solar cells are:

- *Losses due to a single band gap.* Solar cells with a bandgap E_g are transparent to light with a smaller energy than E_g.
- *Losses due to thermalization.* Photons with an energy quantum E_PH larger than the bandgap transfer the whole energy to just one charge carrier. The excess energy $\Delta E_\mathrm{TH} = E_\mathrm{PH} - E_\mathrm{g}$ of the charge carrier is then lost by thermalization and heats up the device.
- *Losses due to thermodynamics and due to materials constants.* Recombination of photo-generated charge carriers occur in semiconductor materials. Two recombination mechanisms cannot be prevented: Radiative recombination (thermodynamics) and Auger recombination (material constants). The mechanisms of recombination in solar cells are depicted in Fig. 2.4 and described in detail in the following.

2.2.1 Intrinsic recombination losses

Recombination is the reverse process of generation, i.e. photo-generated electrons relax back to the valence band. *Intrinsic* recombination cannot be avoided, even

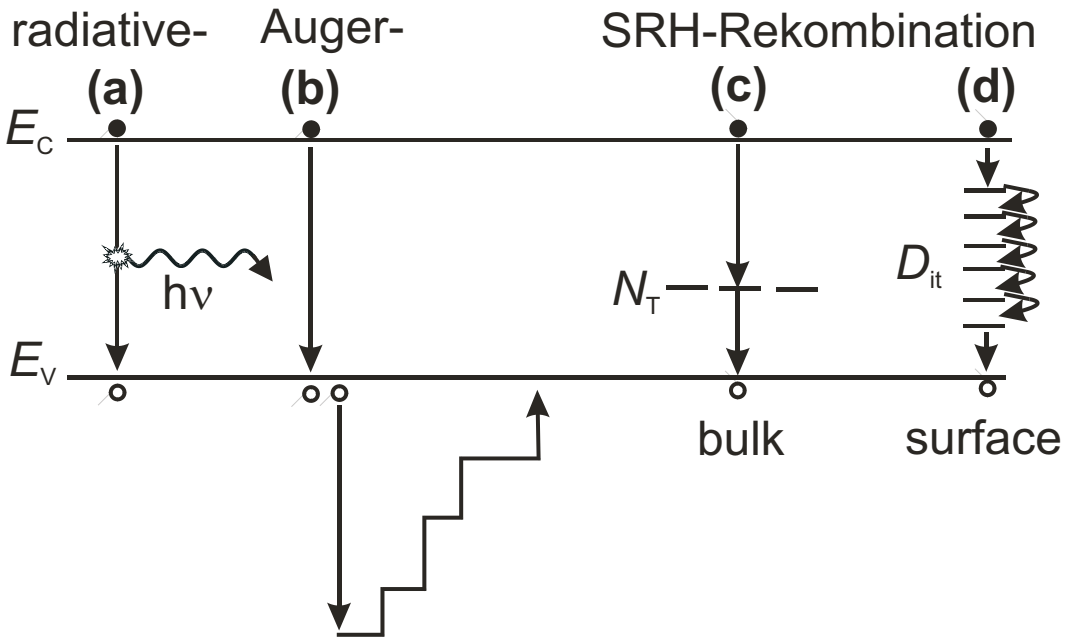

Fig. 2.4**:** Sketch of the predominant recombination mechanisms in semiconductor solar cells. (a) Radiative recombination is the reverse of the photo-generation. The energy of the charge carrier is lost by the generation of a photon. (b) Auger recombination (in this case by holes), a charge carrier transfers its excess energy to kinetic energy of another charge carrier. The energy is subsequently lost by thermalization. (c) Shockley-Read-Hall recombination in the bulk is caused by energy states in the band gap. It depends on the trap density N_T. (d) Surface recombination takes place at the front and back side of the device. It depends on the interface trap density D_{it}, and is caused e.g. by dangling bonds that create energy states in the bandgap.

appears in a perfect crystal and describes the basic thermodynamics as well as the fundamental material properties.

Radiative recombination Radiative recombination, Fig. 2.4a, is the reverse process of photo-generation. Due to the principle of detailed balance, the phot-generation of electron/hole pairs is counter-balanced by radiative recombination. In fact, the semiconductor follows the thermodynamic rules. In the thermodynamic equilibrium, the generation G has to be equal to the recombination R, $G = R$, otherwise the semiconductor would heat up or cool down. Thus, there is a dynamic

equilibrium between generation and recombination within the semiconductor and the mean product of electron and hole concentrations $np = {n_\mathrm{i}}^2$ are constant. An electron recombines with a hole by generating a photon and the radiative recombination rate

$$R_\mathrm{RAD} = Bnp \tag{2.1}$$

is therefore proportional to the electron density n and the hole density p. For crystalline silicon, the material constant B is $B = 2 \times 10^{15}$ cm^3/s [17]. Radiative recombination is usually not the predominant recombination process in Si solar cells and is therefore often neglected.

Auger recombination In the case of Auger recombination, as sketched in Fig. 2.4b, the excess energy of a charge carrier is transferred to kinetic energy of another charge carrier. Usually, the kinetic energy is subsequently lost by thermalization. Auger recombination needs three carriers: an electron/hole pair for the recombination process and an additional carrier that absorbs the excess energy. Auger recombination can therefore be the predominant loss in highly doped areas of the cell. In p-type material, the density n of free electrons is much smaller than the density of free holes p. The excess energy is then usually absorbed by a hole and the Auger recombination rate

$$R_\mathrm{AUG} = Cnp^2 \tag{2.2}$$

depends on the square of the hole concentration p. The Auger coefficient C for silicon is $C = 4 \times 10^{31}$ cm^6/s [18].

2.2.2 Extrinsic recombination processes

Extrinsic recombination describes the material and surface quality and is caused by defects in the crystal lattice as well as by impurities such as metals. It is minimized by a careful manufacturing of the semiconductor to avoid contamination of the bulk and by surface passivation.

Shockley-Read-Hall recombination Shockley-Read-Hall (SRH) recombination, Fig. 2.4c, describes the carrier recombination via relaxation into energy states within the bandgap. The energy states in the bandgap are caused by lattice defects and

by interstitial or substituting impurities. According to Shockley, Read [19] and Hall [20] the recombination rate R_{SRH} holds for all defects inside the semiconductor that cause an energy state in the bandgap in the bulk of the semiconductor

$$R_{\mathrm{SRH}} = \frac{np - {n_{\mathrm{i}}}^2}{(n+n_1)\tau_{\mathrm{p}} + (p+p_1)\tau_{\mathrm{n}}}, \tag{2.3}$$

with $n_1 = N_{\mathrm{C}}\exp((E_{\mathrm{C}} - E_{\mathrm{T}})/kT)$, $p_1 = N_{\mathrm{V}}\exp((E_{\mathrm{T}} - E_{\mathrm{V}})/kT)$ and E_{T} as the energy level of the trap. In Eq. (2.3), the lifetimes

$$\tau_{\mathrm{n,p}} = v_{\mathrm{th}} N_{\mathrm{T}} \sigma_{\mathrm{n,p}} \tag{2.4}$$

depend on the defect density N_{T} and capture cross sections $\sigma_{\mathrm{n,p}}$ of the recombination center.

Surface recombination Surface recombination, Fig. 2.4d, is a special case of SRH-recombination. The energy states within the bandgap at the surface stem from dangling bonds that occur at the edge of the crystal lattice. On the surface, the SRH-recombination rate $R_{\mathrm{SRH,S}}$ per unit of the surface area reads as

$$R_{\mathrm{SRH,S}} = S_{\mathrm{n}} S_{\mathrm{p}} \frac{np - {n_{\mathrm{i}}}^2}{(n+n_1)S_{\mathrm{n}} + (p+p_1)S_{\mathrm{p}}}, \tag{2.5}$$

and the surface recombination velocity is calculated by $S_{\mathrm{n}} = R_{\mathrm{SRH,S}}/(np - {n_{\mathrm{i}}}^2)$. In analogy to $\tau_{\mathrm{n,p}}$ in the volume of the semiconductor with N_{T} as the volume trap density, for the two dimensional surface $S_{\mathrm{n,p}}$ from Eq. (2.5) equals

$$S_{\mathrm{n,p}} = v_{\mathrm{th}} D_{\mathrm{it}} \sigma_{\mathrm{n,p}} \tag{2.6}$$

with the interface trap density D_{it}.

2.3 Heterojunction back contact

An important ingredient for a high-efficiency p-c-Si solar cell back contact is

- *Selectivity for holes.* The back contact forms a low-Ohmic contact for majorities (holes) and repels minorities (electrons).

The present work develops an a-Si:H back contact that satisfies this requirement. The back contact's selectivity serves two distinct tasks: Low resistance (low-Ohmic contact for majorities) to reach high fill factors, and passivation of the surface (low minority carrier recombination) to achieve high open circuit voltages. However, as Fig. 2.3b shows and section 2.1 describes, a c-Si/a-Si:H interface forms rather a selective interface for *electrons* (minorities) than, as desired in the back contact, for *holes* (majorities).

Figures 2.5a-c illustrate how to achieve the selectivity for holes. Figure

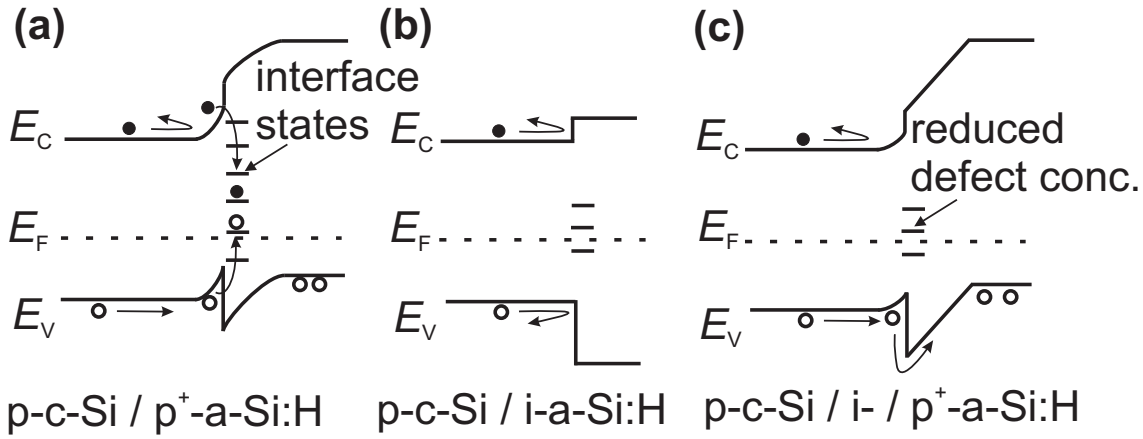

Fig. 2.5**:** Concept to establish a selective a-Si:H hole contact for p-c-Si solar cells. (a) p$^+$-a-Si:H layer contact. Such an interface forms an Ohmic hole contact but the electrons recombine at the defect rich surface. (b) i-a-Si:H layer contact. The minority carrier recombination velocity is now reduced but the contact is not low-Ohmic for holes. (c) i/p-layer stack contact. The combination of the two layers allows for both, a low minority carrier recombination velocity and a low-Ohmic contact for majority carriers.

2.5a shows p-c-Si/p$^+$-a-Si:H contact. The p$^+$-a-Si:H layer creates a BSF that repels electrons. Chapter 6 shows that, despite the valence band offset $\Delta E_V \approx 0.5$ eV [21], such an interface forms a low-Ohmic contact for holes. However, the c-Si surface is not well passivated and defect rich because the p$^+$-a-Si:H layer causes a high density of states distribution within the bandgap at the a-Si:H/c-Si interface. Hence, Fig. 2.5a fulfills the requirement *low-Ohmic contact for majorities* but not for *low minority carrier recombination*. Figure 2.5b shows an i-a-Si:H layer that contacts the p-c-Si. In this case, a low minority carrier recombination velocity is achieved

but such a contact is not low-Ohmic for holes. The following argument explains the low surface minority carrier recombination delivered by the i-a-Si:H: At the c-Si surface, there are dangling (unsaturated) bonds that form recombination centers. Intrinsic a-Si:H saturates such dangling bonds with Si-Si or Si-H bonds and thereby decreases the surface recombination velocity S. Doped a-Si:H does not decrease S as significantly as i-a-Si:H because the density of states within the band gap that form recombination centers is much larger in doped layers. Figure 2.5c shows that the two selectivity tasks together are accomplished by the combination of an i-a-Si:H layer that passivates the surface and a p^+-a-Si:H layer that creates the low Ohmic contact for holes.

Figures 2.6a-c show three sketches of different a-Si:H back contact types that are used for solar cells in the present thesis. The back contacts consist of

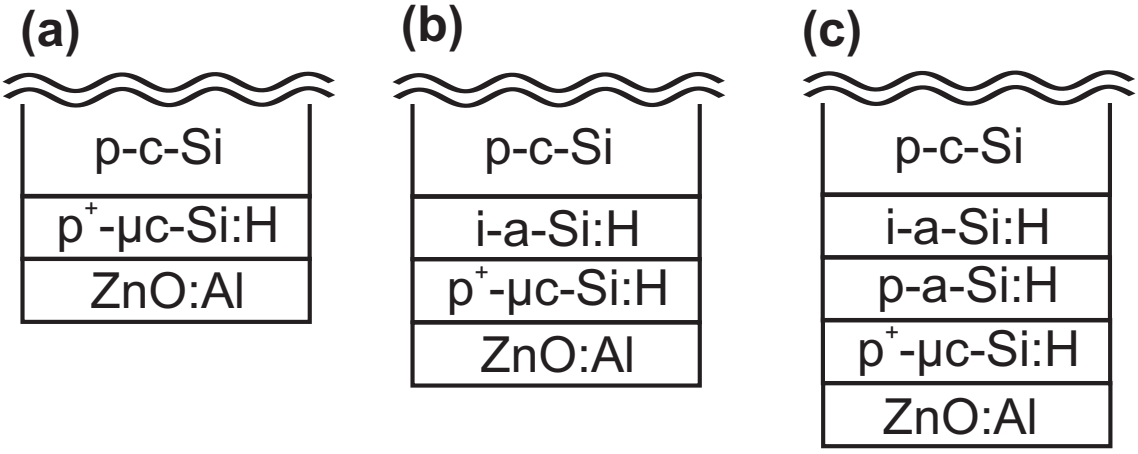

Fig. 2.6**:** Sketch of the three full area a-Si:H back contacts that are evaluated in this thesis. (a) Single layer p-μc-Si:H back contact, (b) double layer i-a-Si:H/p-μc-Si:H back contact and (c) triple layer i-a-Si:H/p-a-Si:H/p-μc-Si:H back contact.

amorphous and micro-crystalline Si, ZnO:Al and aluminum. Instead of only p-a-Si:H as depicted in Fig. 2.5, the back contacts use as well p-μc-Si:H layers. The p-μc-Si:H is higher doped than the p-a-Si:H, see chapter 4, and therewith creates a lower solar cell series resistance as chapter 6 shows. The ZnO:Al layer forms a dielectric mirror and avoids the contamination of the p-μc-Si:H with Al.

Unfortunately, the two requirements *good surface passivation* by the insertion of the intrinsic passivation layer and *low series resistance* are in strong contra-

diction to each other. Two different measuring techniques allow to investigate both tasks separately. The surface passivation quality is analyzed in chapter 5 by the effective lifetime measurement on wafers equipped with i/p-a-Si:H contacts. The resistance is investigated in chapter 6 by current/voltage measurements on wafers that use this specific back contact. Both tasks together are analyzed in complete photovoltaic devices, as well described in chapter 6.

2.4 Heterojunction emitter

The heterojunction emitter (solar cell front side) works as a barrier for holes and a pathway for electrons. A n-a-Si:H/p-c-Si heterojunction makes a nearly ideal emitter due to the large valence band offset and the small conduction band offset. Figure 2.7 shows the band diagram. An electric field that extends into the p-type

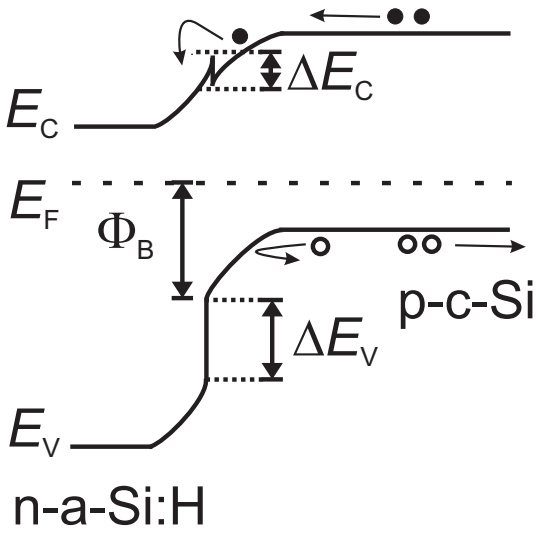

Fig. 2.7: Band diagram sketch of a n-a-Si:H/p-c-Si heterojunction interface. A band offset (ΔE_C in the conduction band and ΔE_V in the valence band) forms at the interface due to the different bandgap of c-Si and a-Si:H. The opposite doping of the a-Si:H layer leads to a pn-junction that causes a space charge region. Electrons are forced towards the junction and holes are repelled. The heterointerface therefore acts as a selective pathway for electrons. However, the barrier for electrons in the conduction band caused by the band offset hampers the carrier transport across the interface.

base forms at the junction due to the opposite a-Si:H doping type. The field forces positively charged holes away from the interface. In contrast, diffusing electrons that reach the space charge region are accelerated by the electric field towards the front contact. The band offsets at the junction form barriers for both electrons and holes. The conduction band offset ΔE_{C} unfortunately hinders the intended transport of electrons across the interface. Still, the height of the barrier is with an energetic value around $\Delta E_{\mathrm{C}} \approx 0.1$ eV small enough to allow a low-Ohmic n-a-Si:H/p-c-Si emitter contact [21].

2.5 Open circuit voltage V_{oc} in heterojunction devices

The minority carrier lifetime limits the cell's open circuit voltage V_{oc} and influences its short circuit current density J_{sc}. Besides, an injection dependence of τ in certain cases imposes a limit on the cell's fill factor FF, as described in section 6.5.1. However, τ has the strongest impact on the open circuit voltage V_{oc}. In the following, I estimate the influences of bulk recombination as well as front and back surface recombination on the open circuit voltage of an a-Si:H/c-Si heterojunction solar cell. The open circuit voltage V_{oc} of a solar cell follows

$$V_{\mathrm{oc}} = \frac{n_{\mathrm{id}} kT}{q} \ln\left(\frac{J_{\mathrm{sc}}}{J_0} + 1\right). \tag{2.7}$$

with n_{id} as the diode ideality, k as the Boltzmann constant, T as the temperature, J_{sc} as the short circuit current density and J_0 as the saturation current density. This equation can be simplified to

$$V_{\mathrm{oc}} = n_{\mathrm{id}} V_{\mathrm{T}} \ln\frac{J_{\mathrm{sc}}}{J_0} \tag{2.8}$$

because J_{sc} is normally much larger than J_0. A high minority carrier lifetime τ causes a low saturation current density J_0 and therefore a high open circuit voltage V_{oc}. Figure 2.8 shows the different saturation current densities that occur due to recombination in a real solar cell. There are four components in the saturation current density: $J_{0,\mathrm{front}}$ that stems from front side recombination, $J_{0,\mathrm{scr}}$ generated by recombination in the space charge region, $J_{0,\mathrm{bulk}}$ that is caused by bulk recombination,

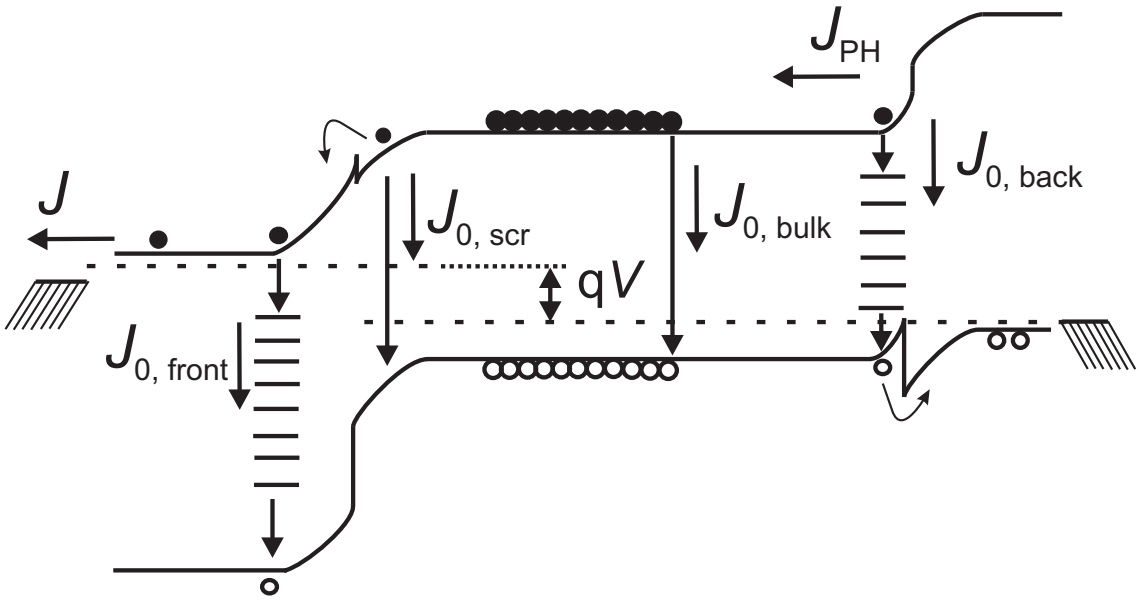

Fig. 2.8: Sketch of four saturation current densities that occur in a heterojunction solar cell. The total photo-generated current is J_{PH}. The saturation current densities are $J_{0,front}$ created by surface recombination at the front side interface, $J_{0,scr}$ that stems from recombination in the space charge region, $J_{0,bulk}$ that is caused by bulk recombination, and $J_{0,back}$ generated by surface recombination at back side interface. The current density J is extracted from the device.

and $J_{0,\mathrm{back}}$ that occurs due to back side recombination. If the device is connected to a load, the current density J is extracted. The recombination in the Space Charge Region SCR is usually neglected due to the presence of the electric field. The electric field minimizes the length of stay of charge carriers in the SCR. Casually speaking, the excess charge carriers that reach the SCR are gone before they have enough time τ to recombine. To determine the influences of the bulk recombination as well as the front and back surface recombination on J_0 and V_{oc}, I calculate three different saturation current densities $J_{0,\mathrm{front}}$, $J_{0,\mathrm{bulk}}$, and $J_{0,\mathrm{back}}$. With electrons as minority carriers (p-type base material), I use the dark carrier distribution Δn_{d} calculated from the one-dimensional diffusion equation for the calculation [22]

$$\frac{\Delta n_{\mathrm{d}}(x)}{\Delta n(0)} = \cosh\left(\frac{x}{L_{\mathrm{n}}}\right) - \frac{L_{\mathrm{n}}}{L_{\mathrm{eff}}}\sinh\left(\frac{x}{L_{\mathrm{n}}}\right) \tag{2.9}$$

assuming the simplification that the illuminated case can be calculated by superposition. The saturation current density in the bulk $J_{0,\mathrm{bulk}}$ writes as

$$\begin{aligned} J_{0,\mathrm{bulk}} &= q \int_{x=0}^{x=d} \frac{\Delta n(x,V)}{\tau_{\mathrm{bulk}}}\,\mathrm{d}x \\ &= q\frac{\Delta n(0)}{\tau_{\mathrm{b}}}\left[L_{\mathrm{n}}\sinh\left(\frac{d}{L_{\mathrm{n}}}\right) - \frac{L_{\mathrm{n}}^2}{L_{\mathrm{eff}}}\left(\cosh\left(\frac{d}{L_{\mathrm{n}}}\right)-1\right)\right] \end{aligned} \tag{2.10}$$

with τ_{b} as the bulk lifetime and L_{eff} as the effective diffusion length. The carrier distribution $\Delta n(0)$ at $x = 0$, the edge of the space charge region, follows

$$\Delta n(0) = \frac{{n_{\mathrm{i}}}^2}{N_{\mathrm{A}}}\left[\exp\left(\frac{qV}{kT}\right)-1\right] \tag{2.11}$$

and depends on the doping concentration N_{A}. The effective diffusion length L_{eff} is a function of the bulk diffusion length $L_{\mathrm{n}} = \sqrt{D_{\mathrm{n}}\tau_{\mathrm{b}}}$ with D_{n} as the diffusion constant of electrons, and the surface recombination velocity S:

$$L_{\mathrm{eff}} = L_{\mathrm{n}}\frac{SL_{\mathrm{n}}\sinh(d/L_{\mathrm{n}}) + D_{\mathrm{n}}\cosh(d/L_{\mathrm{n}})}{SL_{\mathrm{n}}\cosh(d/L_{\mathrm{n}}) + D_{\mathrm{n}}\sinh(d/L_{\mathrm{n}})}. \tag{2.12}$$

The back side saturation current density

$$\begin{aligned} J_{0,\mathrm{back}} &= qS_{\mathrm{back}}\Delta n(d,V) \\ &= qS_{\mathrm{back}}\Delta n(0)\left[\cosh\left(\frac{d}{L_{\mathrm{n}}}\right) - \frac{L_{\mathrm{n}}}{L_{\mathrm{eff}}}\sinh\left(\frac{d}{L_{\mathrm{n}}}\right)\right] \end{aligned} \tag{2.13}$$

depends on the back side recombination velocity S_{back}.

At the front interface of a heterojunction solar cell, the front side saturation current density $J_{0,\mathrm{front}}$ follows from

$$J_{0,\mathrm{front}} = qS_{\mathrm{front}}N_{\mathrm{A}}\exp\left(\frac{\Phi_{\mathrm{B}}}{kT}\right)\left[\exp\left(\frac{qV}{kT}\right)-1\right]. \tag{2.14}$$

and depends on the barrier height Φ_{B}, cf. Fig. 2.7 in section 2.4. For sufficiently high charge carrier mobilities, the total saturation current density is the linear superposition of all saturation current densities

$$J_{0,\mathrm{total}} = J_{0,\mathrm{bulk}} + J_{0,\mathrm{back}} + J_{0,\mathrm{front}}. \tag{2.15}$$

Figures 2.9a-d show V_{oc} as well as the ratio of the different saturation current densities $J_{0,bulk}/J_{0,total}$, $J_{0,front}/J_{0,total}$, and $J_{0,back}/J_{0,total}$ plotted versus L_n/d, that is the bulk diffusion length L_n normalized by the cell thickness d. The figures visualize the contribution of the different recombination currents (bulk, front and back) to the devices's total recombination current and their impact on V_{oc}, assuming a surface recombination velocity of $S_{front} = S_{back} = S = 100$ cm/s and a cell thickness of $d = 250$ μm. The third parameter, the built in potential Φ_B, can be extracted for example from high frequency capacitance/voltage measurements and depends on the doping of the base and the emitter [23, 24]. According to the cited references, assuming a common doping of the base 10^{16} cm$^{-3} \leq N_A \leq 10^{17}$ cm^{-3} and an emitter doping of $10^{18} \leq N_D \leq 10^{19}$ cm^{-3} the barrier height ranges around 0.75 eV $\leq \Phi_B \leq 0.85$ eV.

Figures 2.9a,c are calculated for a built in front side barrier $\Phi_B = 0.75$ eV and Figs. 2.9b,d for $\Phi_B = 0.8$ eV. The comparison of Figs. 2.9a,c with Figs. 2.9b,d shows how crucial a high Φ_B is to achieve a low front side recombination and therewith a high open circuit voltage V_{oc}. For low bulk diffusion lengths, the bulk saturation current density $J_{0,bulk}$ predominates and surface recombination plays a minor role for both $\Phi_B = 0.75$ eV and $\Phi_B = 0.8$ eV. If the bulk diffusion length L_n exceeds the cell thickness d by a factor of more than 5 (high quality c-Si material), Fig. 2.9b shows that for $\Phi_B = 0.75$ eV front and back side recombination currents $J_{0,front}$ and $J_{0,back}$ contribute almost with equal shares to the total saturation current density $J_{0,total}$. For $\Phi_B = 0.8$ eV however, Fig. 2.9c visualizes that the front side saturation current $J_{0,front}$ plays a *much less* pronounced role. It is remarkable that an increase of Φ_B by just 5 meV causes such a major change. Figure 2.9a shows that for $\Phi_B = 0.75$ eV the open circuit voltage saturates at $V_{oc} = 675$ mV whereas Fig. 2.9b depicts that for $\Phi_B = 0.8$ eV a decidedly higher $V_{oc} = 690$ mV is achieved. Hence, the V_{oc} potential of a heterrojunction solar cell is proportional to Φ_B and S. The impact of S on the open circuit voltage lowers with increasing Φ_B. For a high quality heterojunction emitter, a large built in potential Φ_B is therefore an important ingredient. Figures 2.10a,b compare the emitter of a p-type (Fig. 2.10a) and an n-type (Fig. 2.10b) a-Si:H/c-Si heterojunction solar cell. The figure exhibits an inherent disadvantage of the n-a-Si:H/p-c-Si heterocontact. The built in potential Φ_B of this interface is lower than that of its p-a-Si:H/n-c-Si counterpart. The front surface recombination in devices with n-a-Si:H/p-c-Si heterocontacts is therefore

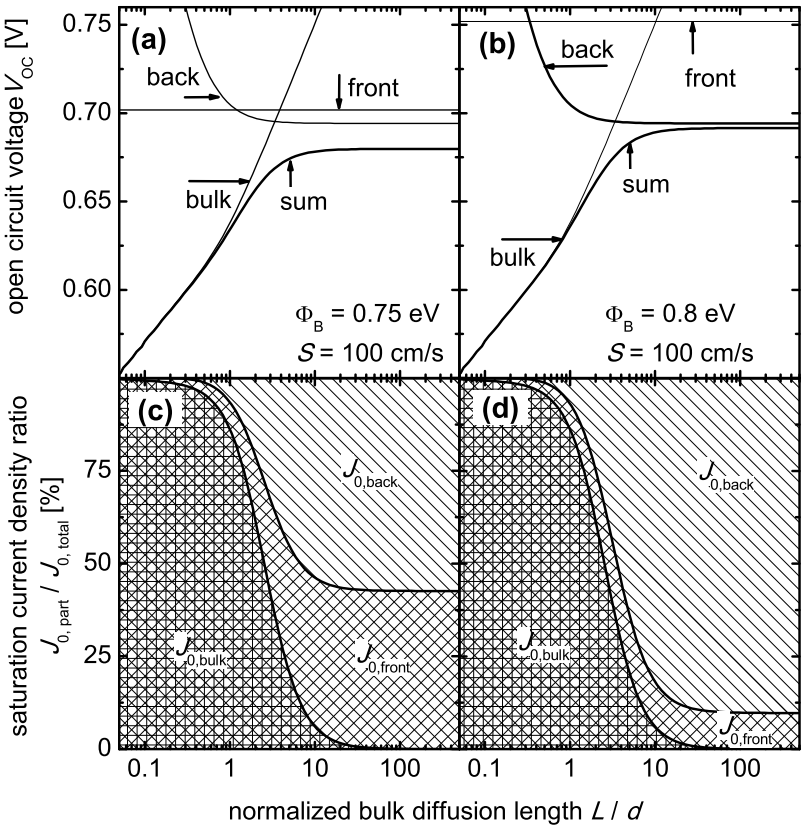

Fig. 2.9**:** Open circuit voltage calculated from Eq. (2.8) and saturation current density ratios calculated from Eqs. (2.10), (2.13), (2.14) and (2.15) for a surface recombination velocity of $S_{\text{front}} = S_{\text{back}} = S = 100$ cm/s and a cell thickness of $d = 250$ μm. (a) and (c) belong together and use a built in barrier of $\Phi_B = 0.75$ eV. (b) and (d) use $\Phi_B = 0.8$ eV. For high quality c-Si material, i. e. when the bulk diffusion length L_n exceeds the cell thickness d by a factor of more than 5, a comparison of (a) and (b) shows that the larger Φ_B yields a decidedly larger open circuit voltage V_{OC}. Comparing (c) and (d) clarifies that the larger $\Phi_B = 0.8$ eV causes a much lower contribution of the front side saturation current density $J_{0,\text{front}}$ to the total saturation current density $J_{0,\text{total}}$ of the device. Hence, $J_{0,\text{total}}$ is lower for a larger Φ_B and, for high quality heterojunction emitters aimed to deliver high open circuit voltages, a large built in potential Φ_B is an essential solar cell ingredient.

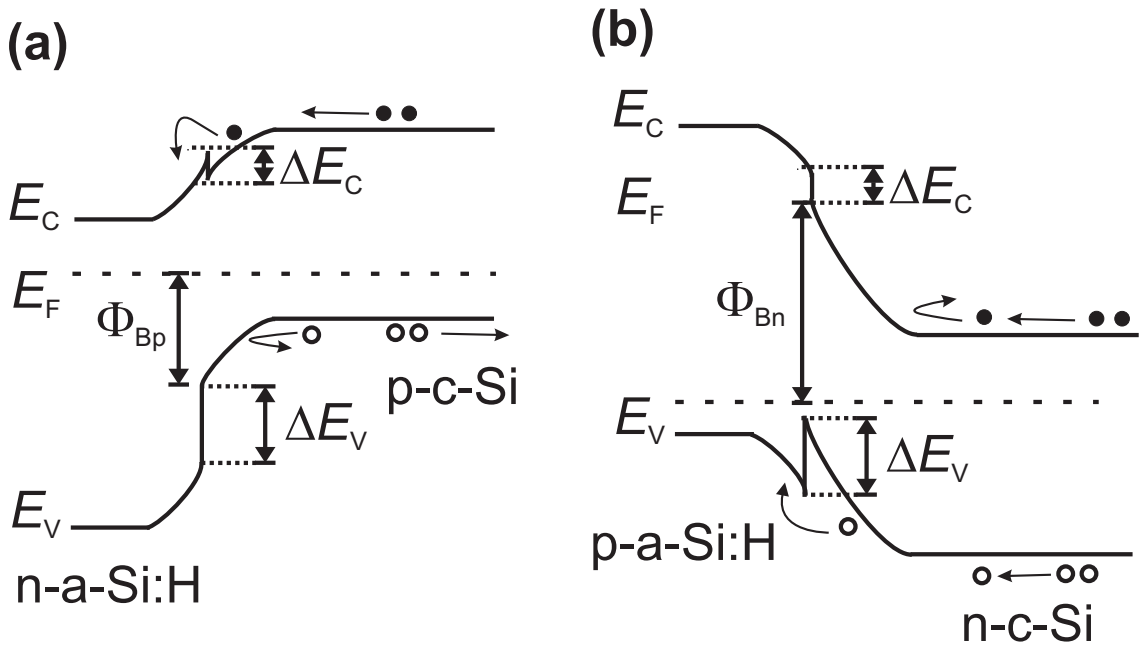

Fig. 2.10: Comparison of a-Si:H emitters on different doped c-Si substrates. (a) n-a-Si:H/p-c-Si heterocontact. (b) p-a-Si:H/n-c-Si heterocontact. Contact (b) has the higher built in potential Φ_{Bn} if compared with contact (a). Hence, the front surface recombination in n-type c-Si solar cells with a-Si:H emitters plays a minor role and the devices have the potential to reach higher open circuit voltages than their n-a-Si:H/p-c-Si counterparts.

more pronounced. Thus, p-a-Si:H/n-c-Si solar cells have the inherent capability to reach higher open circuit voltages than n-a-Si:H/p-c-Si solar cells.

Chapter 3

Measuring techniques and deposition methods

3.1 Measuring techniques

This section explains the measuring techniques to characterize solar cells as well as individual process steps necessary for their fabrication. The solar cells are characterized by current/voltage and quantum efficiency measurements. The quasi steady state Photoconductance, a tool for minority carrier lifetime characterization, measures the a-Si:H/c-Si surface passivation quality. The transmission measurement and the temperature dependent conductance measurement allow one to investigate the performance of individual a-Si:H layers.

3.1.1 Current/Voltage characteristics

According to Eq. (2.7), the current/voltage (I/V) characteristics of a solar cell follow an exponential diode behavior. From the I/V-measurement under illumination, the four device parameters

- Open circuit voltage V_{oc}
- Short circuit current density J_{sc}
- Fill factor FF and
- Efficiency η

are derived. The open circuit voltage is the voltage that the solar cell delivers without connected load. It gives information about the material quality and the surface passivation quality. The doping of the substrate and the emitter also play an important role for V_{oc} [25]. The short circuit current density J_{sc} is the current that is extracted from the device. The fill factor

$$FF = \frac{P_{\mathrm{MAX}}}{J_{\mathrm{sc}} V_{\mathrm{oc}}} \tag{3.1}$$

is the ratio between the cell's maximum power P_{MAX} and the power given by the $J_{\mathrm{sc}} \times V_{\mathrm{oc}}$ product. The conversion efficiency η of a solar cell is given by the ratio of the optical input power P_{OPTIC} to the electrical output power P_{MAX}

$$\eta = \frac{P_{\mathrm{MAX}}}{P_{\mathrm{OPTIC}}} = FF \frac{J_{\mathrm{sc}} V_{\mathrm{oc}}}{P_{\mathrm{OPTIC}}}. \tag{3.2}$$

Apart from the cost of the device per conversion power (EUR per watt), the conversion efficiency η is the most important solar cell parameter.

3.1.2 Quantum efficiency QE

The external quantum efficiency EQE follows

$$\mathrm{EQE}(\lambda) = \int_0^d f_{\mathrm{abs}}(\lambda, x) \eta_{\mathrm{c}}(\lambda) \mathrm{d}x = \frac{J_{\mathrm{sc}}(\lambda)}{q\phi(\lambda)} \tag{3.3}$$

with f_{abs} as the probability that a photon is absorbed and η_{c} as the collection probability of the generated charge carrier. The EQE is a measure for the amount of extracted electron/hole pairs generated by photons with a certain wavelength λ that contribute to the current.

An EQE measurement (spectrally resolved J_{sc} measurement) contains information on the optical as well as electrical properties (bulk and surface quality) of the device. The short circuit current density J_{sc} of the cell is measured under monochromatic light illumination with a known intensity.

The EQE includes the optical properties of the device. Taking into account the reflection R at the front side, the internal quantum efficiency

$$\mathrm{IQE}(\lambda) = \frac{\mathrm{EQE}(\lambda)}{1 - R(\lambda)} \tag{3.4}$$

characterizes the electrical device properties. The IQE is, according to Brendel at al., a sum of the carrier fractions generated in the emitter, the space charge region and the base [26].

An appropriate way to characterize for example the bulk and back surface quality of a c-Si device is via the effective diffusion length L_{eff} of minority carriers from Eq. (2.12). According to Ref. [27], L_{eff} is derived from a standard analysis of the IQE of silicon solar cells and depends on the bulk diffusion length L_{n}, the base thickness d, the minority carrier diffusion constant D, and the back surface recombination velocity S. A plot of the inverse internal quantum efficiency

$$\text{IQE}^{-1} = 1 + \frac{L_\alpha}{L_{\text{eff}}}, \tag{3.5}$$

versus the absorption length L_α for $10\,\mu\text{m} < L_\alpha < d/4$ usually follows a linear behavior making it convenient to derive L_{eff} [28]. If the mono-crystalline c-Si solar cell is textured with random pyriamids on the front side, one has to consider the longer effective path length of the light refracted at the surface by a factor $\cos(\theta)$ with $\theta = 41.8°$ [27]

$$\text{IQE}^{-1} = 1 + \frac{L_\alpha \cos(\theta)}{L_{\text{eff}}}. \tag{3.6}$$

The internal quantum efficiency also yields information on the front side in the wavelength regime $\lambda \leq 400$ nm. Neglecting the ionization of carriers due to collisions as described in Ref. [29], the quantum efficiency can be assumed as constant in this wavelength range. The IQE is then independent of the emitter diffusion length and holds according to [30]

$$\text{IQE}^{-1}(L_\alpha) = 1 + \frac{D_{\text{e}} + S_{\text{f}} L_\alpha}{D_{\text{e}} + S_{\text{f}} d_{\text{e}}}, \tag{3.7}$$

with the front side recombination velocity S_{f}, the depth of the emitter d_{e} and the emitter diffusion constant D_{e}.

3.1.3 Minority carrier lifetime τ

The excess carrier lifetime τ describes how long a generated charge carrier remains in the excited state before it relaxes. A comprehensive review about the excess carrier lifetimes in silicon is found in Ref. [31]. In an illuminated solar cell under

operating conditions $V < V_{\mathrm{oc}}$, the thermodynamic equilibrium is not preserved. The device absorbs much more photons of the impinging light than it reemits. Hence, it holds $np > {n_{\mathrm{i}}}^2 = n_0 p_0$ for the electron and hole concentration. Excess carriers $\Delta n = n - n_0$ and $\Delta p = p - p_0$ are generated and $\Delta n = \Delta p$ holds if carrier trapping is neglected because every photon generates an electron/hole pair.

If the illumination is switched off at a time $t = 0$, the excess carrier density Δn decays exponentially as

$$\Delta n(t) = \Delta n(t = 0) \exp\left(-\frac{t}{\tau_{\mathrm{n}}}\right), \tag{3.8}$$

with the carrier lifetime

$$\tau_{\mathrm{n}} = \frac{\Delta n}{U}. \tag{3.9}$$

The net recombination rate $U = R - R_{\mathrm{rad}}$ follows from

$$U = -\frac{\partial \Delta n}{\partial t}. \tag{3.10}$$

As described in section 2.2, there are various recombination mechanisms with different recombination rates U_{i} that imply different limits on the excess carrier lifetime τ_{i}. The reciprocal value of the combined excess carrier lifetime

$$\frac{1}{\tau_{\mathrm{eff}}} = \sum \frac{1}{\tau_{\mathrm{i}}} \tag{3.11}$$

is the sum of the reciprocal values of the different lifetimes τ_{i}. The index i stands for the different recombination mechanisms such as radiative-, Auger-, or SRH-recombination.

Measuring technique

Most effective lifetime samples in this work are measured with the the Quasi Steady State Photoconductance (QSSPC) setup. It is is a convenient, quick and powerful measuring technique to characterize crystalline silicon. The QSSPC was developed by Sinton and Quevas [32]. Figure 3.1 shows a sketch of the measuring setup. The method uses the dependence of the semiconductor conductivity σ on the excess minority carrier density Δn. A flash light pulse generates excess carriers in the wafer. The diffusion equation of the photo-generated charge carriers

$$\frac{\partial \Delta n(x,t)}{\partial t} = G - U + D_{\mathrm{n}} \frac{\partial^2 \Delta n(x,t)}{\partial x^2}, \tag{3.12}$$

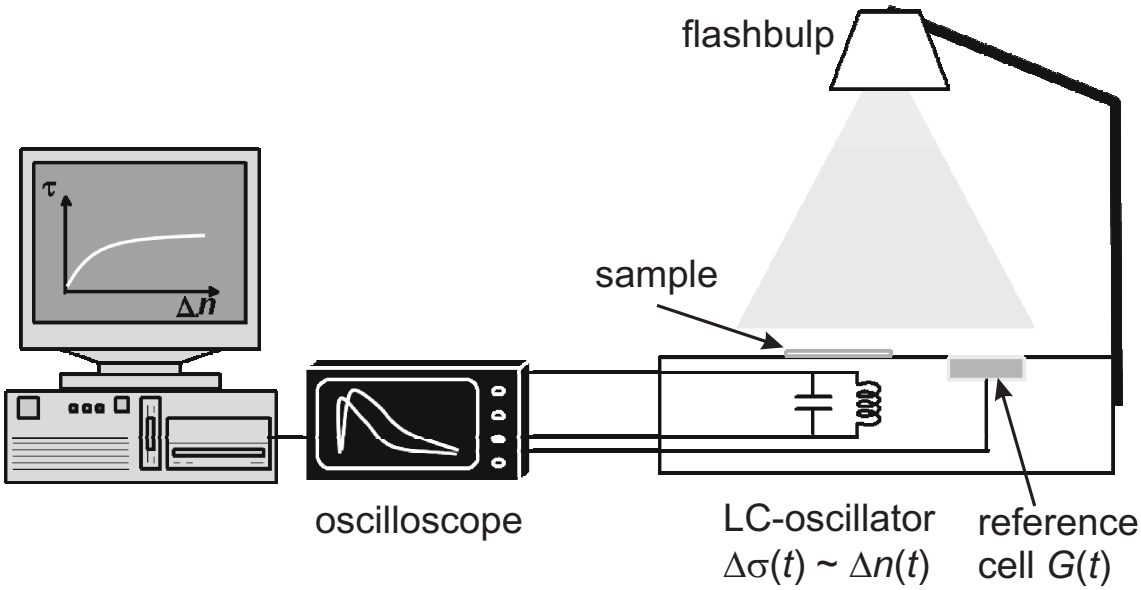

Fig. 3.1: Sketch of the Quasi Steady State Photoconductance measuring setup. The LC-oscillator detects the conductance variation in the sample caused by the photogenerated charge carriers. The reference cell measures the generation rate of the flashbulb simultaneously. Both signals are recorded by an oscilloscope and processed by a computer.

with G as the generation rate, U as the net recombination rate and D_{n} as the diffusion coefficient, forms the base to derive the carrier lifetime. For sufficiently large charge carrier mobilities, all spatial spatial gradients area levelled out and the diffusion equation 3.12 reduces to

$$\frac{\partial \Delta n(x,t)}{\partial t} = G - U. \tag{3.13}$$

Therefore, after switching off the generation, the excess carrier density Δn decays exponentially and the recombination rate U follows from $U = \Delta n/\tau$. The QSSPC setup measures the generation rate G with a reference cell. With a given generation G, it is then necessary to know the excess carrier density Δn in the sample to derive τ. With the correlation

$$\Delta\sigma = q(\mu_{\mathrm{n}} + \mu_{\mathrm{p}})\Delta n, \tag{3.14}$$

where μ_n is the electron mobility and μ_p the hole mobility in the sample, Δn is extracted from the excess photoconductance $\Delta\sigma = \sigma - \sigma_0$, where σ is the photoconductance and σ_0 is the equilibrium conductance in the dark.

The core of the QSSPC setup is the LC-oscillator configuration that has a linear dependence between the measured voltage ΔV and the conductance σ of the sample:

$$\Delta V = k_{\mathrm{cal}} \Delta\sigma. \tag{3.15}$$

The oscillator has to be calibrated first with a sample of known resistance to determine the proportionality coefficient k_{cal}. Reference [33] describes details about the advanced analysis of lifetime measurements from the QSSPC-technique as well as other lifetime measurement techniques.

3.1.4 Optical transmission

The transmission measurement characterizes single a-Si:H layers on glass substrates. The measurements are performed with a Varian Cary 5e spectrometer. First, a baseline calibration measurement of the optical path without the sample is carried out. Then, the sample is placed within the course of the light and the optical transmission is measured. From optical transmission measurements of a-Si:H layers on glass, I derive the layer thickness via a an optical model that assumes a stack of plane-parallel flat layers with abrupt interfaces through which a plane wave propagates coherently [34, 35]. The model also takes into account the optical properties of the glass substrate. Transmission measurements also yield information on the bandgap and the absorptance of the material.

3.1.5 Conductance measurements at a-Si:H layers

Conductance measurements to characterize a-Si:H layers are carried out in dependance of the applied temperature or with and without illumination. For the 4-point probe measurement, two coplanar aluminum contacts with a contact length of 0.5 cm and a distance of 0.5 or 1 mm are evaporated onto the a-Si:H layer that is fabricated on a corning glass substrate. The layer is then mounted in a vacuum setup and heated to 100 °C to remove adsorbates.

The activation energy E_a is derived via

$$\sigma_d = \sigma_0 \exp \frac{-qE_a}{kT}, \tag{3.16}$$

from temperature dependent dark conductance σ_d; here q denotes the elementary charge, k the Boltzmann constant, T the temperature, and σ_0 the conductance for $T \to \infty$. The measurement gives information on the location of the Fermi level E_F within the bandgap. For intrinsic and n-type layers, E_a describes the energetic distance of the Fermi level E_F from the conduction band edge E_C. For p-type layers, E_a stands for the energetic distance of the Fermi level E_F from the valence band edge E_V. Thus, E_a is an important measure for the doping level of the a-Si:H layers.

For intrinsic layers, σ_d and E_a serve as criteria for the material quality. The lower the dark conductivity σ_d and the closer E_a is located at the middle of the bandgap, i. e. for $E_a = E_g/2$ the less contaminated is the layer with impurities and dopants. For doped layers, a prerequisite for high conductivities is to minimize E_a. To do an exact analysis of the activation energy, it is necessary to take into account the temperature dependence of E_a itself [36, 37].

3.2 Deposition methods

This section resumes the technologies to fabricate heterojunction devices. The first part introduces the deposition setup that is installed at the Institut für Physikalische Elektronik, ipe. The second part of this section describes the Plasma Enhanced Chemical Vapor Deposition PECVD to deposit amorphous and microcrystalline silicon. The third part introduces the magnetron sputtering technique to fabricate transparent conductive oxides TCO.

3.2.1 The deposition setup

Figure 3.3 shows a picture of the deposition setup (MV-Systems) installed at the *ipe*. The machine has four deposition chambers. One chamber for ZnO:Al sputtering, and one chamber each for the PECVD deposition of i-a-Si:H, n-a-Si:H and p-a-Si:H. The separation of the chambers for doped and undoped a-SiH is essential to fabricate intrinsic films of high quality. It is also of advantage if the p- and n-type layers are deposited in separate chambers to avoid cross-doping.

Fig. 3.2: Picture of the a-Si:H and ZnO:Al cluster deposition machine. The system has four chambers. One for i-a-aSi:H, n-a-Si:H and p-a-Si:H plasma enhanced chemical vapor deposition and one for ZnO:Al sputtering, respectively.

3.2.2 Plasma Enhanced Chemical Vapor Deposition

Figure 3.3 shows a sketch of the inside of a PECVD chamber. The abbreviation PECVD stands for Plasma Enhanced Chemical Vapor Deposition that is a special case of the Chemical Vapor Deposition CVD [38]. For CVD, a chemical reaction in the gas phase takes place inside the deposition chamber. The reaction is caused by high substrate temperatures [39,40]. In PECVD, the chemical reaction is caused or enhanced by a plasma. The advantage of PECVD if compared with CVD is a higher growth rate and a lower substrate temperature, e.g. enabling the use of plastic as a substrate [41]. The first remarkable breakthrough for the a-Si:H deposition actually

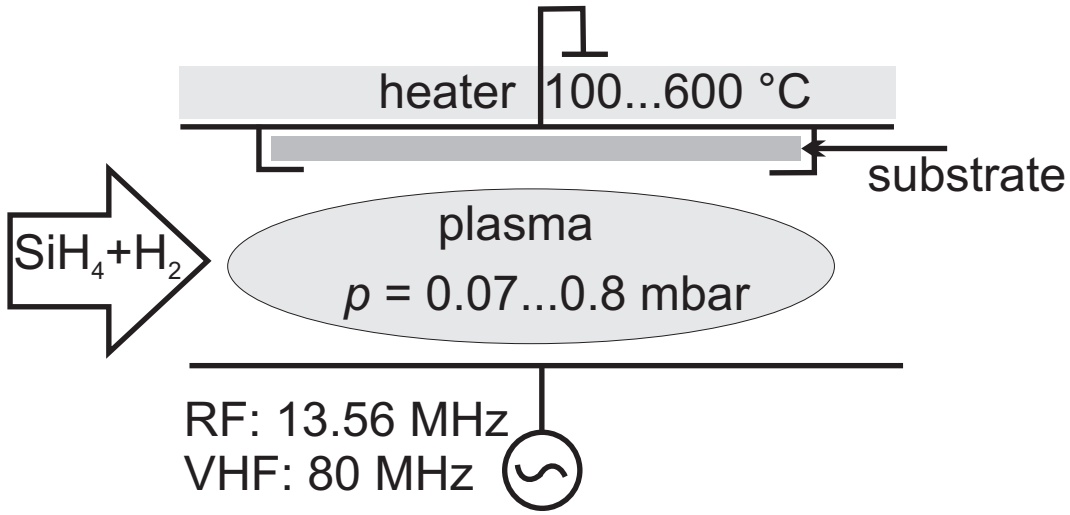

Fig. 3.3: Sketch of the deposition chamber. The gases silane (SiH_4) and (if additionally desired) hydrogen (H_2) flow into the chamber. The alternating electrical field, in this work applied either with a radio frequency of 13.56 MHZ or a very high frequency of 80 MHZ, decomposes the source gas into SiH_x radicals and atomic hydrogen. Hydrogenated amorphous silicon (a-Si:H) grows on the surface of the substrate.

came with the use of PECVD by Chittick et al. [42]. The plasma is generated by an alternating electric field applied in between two electrodes. The source gas silane (SiH_4) is decomposed in the plasma into SiH_x radicals and atomic hydrogen. Then, hydrogenated amorphous silicon (a-Si:H) starts to grow on the surface of the substrate. Note that sputtering as a physical vapor deposition process is an alternative a-Si and a-Si:H fabrication technique [43]. However, the electron drift mobility is lower in sputtered a-Si:H layers than in their by PECVD fabricated counterparts [44].

Hydrogen is an additional gas that plays an important role for the a-Si:H deposition. An addition of hydrogen during a-Si:H growth mainly leads to a change from amorphous to microcrystalline deposition after surpassing a certain dilution ratio. Usually, the transition regime between amorphous and microcrystalline Si growth takes place in a hydrogen dilution range $R = [H_2] / [SiH_4] \approx$ 10-30 [45]. Microcrystalline Si, in the following denoted as μc-Si:H, stands in fact for a wide range of Si material. Its composition contains varying amounts of crystalline grains and

voids embedded in an amorphous phase. The structural and electronic properties of this material have been widely studied over the last 20 years [46–48]. Not only a high hydrogen dilution during deposition but also a high glow discharge power leads to microcrystalline instead of amorphous growth [45]. Depositing with a hydrogen dilution in the transition regime between the amorphous and microcrystalline deposition leads to the growth of proto-crystalline Si [49].

There are three more parameters that affect the growth of a-Si:H besides gas composition and glow discharge power: The deposition pressure p, the substrate temperature T_s and the plasma excitation frequency ν_p. The deposition pressure mainly affects growth rate and homogeneity [50]. The substrate temperature changes the nucleation properties and has an impact on the defect density in the film [50]. The plasma excitation frequency has also an important impact on the film properties concerning film quality and doping ratio, details are found in [45, 51, 52].

The plasma excitation frequency classifies the PECVD process into RF-PECVD with a standard frequency of $\nu_\mathrm{p} = 13.56$ MHz and VHF-PECVD with higher frequencies up to $\nu_\mathrm{p} \approx 150$ MHz. Usually, a-Si:H is deposited with RF-PECVD. The higher frequency of the VHF-PECVD leads to a much higher film quality and to a more effective doping in doped layers when depositing μc-Si:H.

The depositions in this work use RF-PECVD with the standard frequency of $\nu_\mathrm{p} = 13.56$ MHz to grow the amorphous films. For the growth of the microcrystalline layers, the VHF-PECVD with a plasma excitation frequency of $\nu_\mathrm{p} = 80$ MHz is used. However, the μc-Si:H films that are deposited for the heterojunction back contacts and emitters have thicknesses of only a few nanometers and one can hardly talk about a *real* microcrystalline layer in this case. It has been observed that during the deposition of a μc-Si:H layer on top of a substrate there grows a 30 - 50 nm thick interlayer denoted as "incubation zone" that contains a varying amount of microcrystals [53]. The crystalline fraction in this zone as well as its thickness strongly depend on the deposition conditions and the substrate material. I nevertheless denote the thin layers that are grown in the microcrystalline deposition regime as μc-Si:H in the following.

3.2.3 Transparent conductive oxide magnetron sputtering

Figure 3.4 shows a sketch of a magnetron sputtering chamber. Sputtering is a physical vapor deposition (PVD) process. Atoms in a solid state target are released out into the gaseous phase by highly energetic ion bombardment. The target

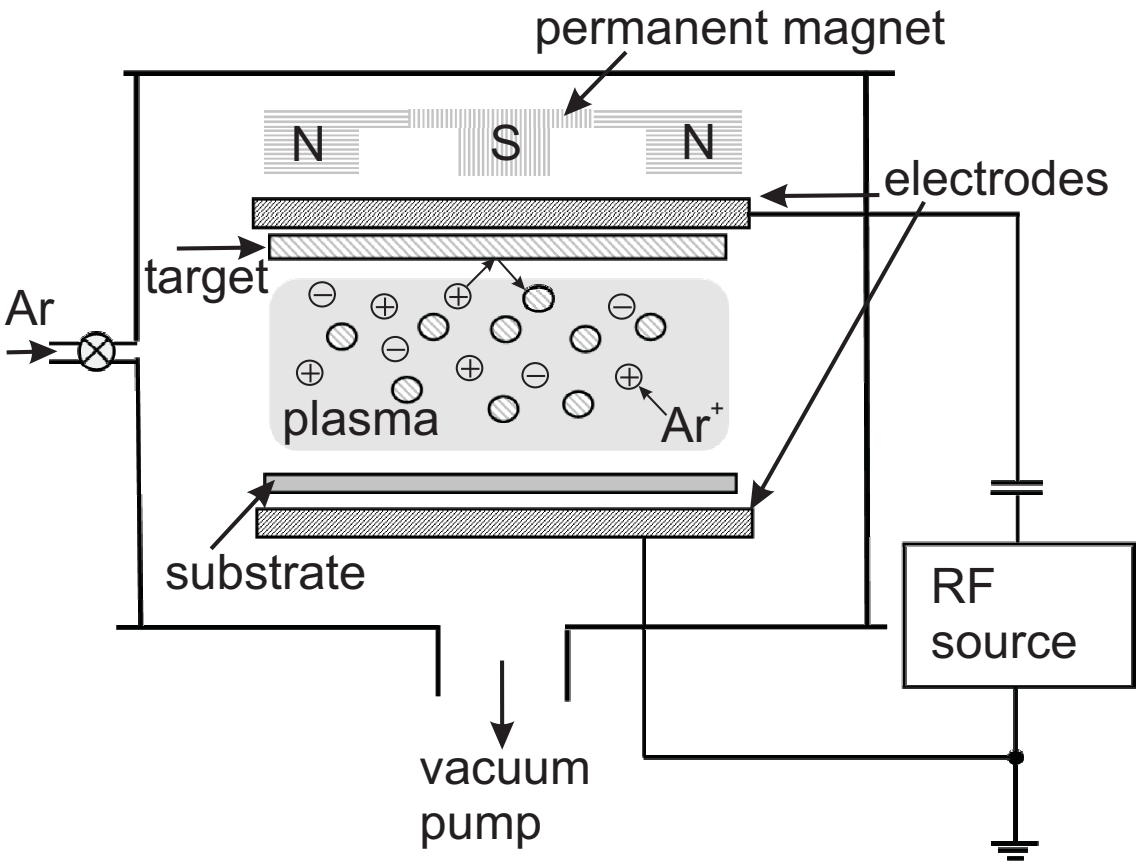

Fig. 3.4: Sketch of a magnetron sputtering chamber. Argon as the working gas is ionized in a RF-plasma. The ions bombard the target and release atoms into the gaseous phase. The target atoms then deposit on the substrate and on the walls of the chamber. The permanent magnet causes a higher ionization rate by forcing the electrons that ionize the argon on circular paths near the target. The time that the electrons remain inside the deposition chamber is thereby enhanced.

atoms are then deposited on the surface of the substrate and all over the walls of the deposition chamber. Usually, an inert gas such as Argon is used as the working

gas that supplies the ions for the target bombardment. A plasma excited by a RF or DC generator delivers the energy needed for the ionization.

Magnetron sputtering is a modified sputtering technique yielding a higher ionization rate. A permanent magnet that is mounted behind the target forces electrons on circular paths near the target. The electrons then remain longer within the deposition chamber and the ionization probability of the inert gas by the electrons is increased. More generated ions cause an increased deposition rate. Besides, the total pressure in the chamber can be decreased and the plasma still remains stable. Having a lower deposition pressure decreases the probability that a free target atom hits another atom on its way towards the substrate. The target atoms therefore hit the substrate surface with a higher energy yielding a denser film. The magnetic field also hinders electrons from hitting the substrate and the thermal load of the substrate is decreased [54].

Chapter 4

Single a-Si:H layers

This chapter starts with an introduction into the properties of amorphous silicon. It then presents the depositions of intrinsic a-Si:H layers on glass substrates focused on the goal to achieve a good layer homogeneity. The last part of this chapter focuses on p-type doped a-Si:H with the target to achieve good layer homogeneities and a very high doping level. As Figs. 2.6a-c show, both intrinsic and p-type layers are part of the heterojunction back contact.

4.1 Properties of amorphous silicon

Figure 4.1 shows the calculated defect density of amorphous silicon plotted versus the energy. The figure is provided by courtesy of Al Tarabsheh [55]. The calculation is based on a standard model for amorphous silicon [56]. In difference to c-Si, amorphous silicon has no long range order. Figure 4.1 illustrates the impact of the lack of crystallinity on the density of states. The amorphous structure causes different bond lengths between the Si atoms leading to a broadly distributed density of states throughout the energy range and no sharp band edges. The present energy states in the middle of the band gap stem from unsaturated bonds. Hence, amorphous silicon has no well defined band gap like its crystalline counterpart and exhibits a continuous density of states in the bandgap. The density of these so-called dangling bonds is for a-Si in the range of $10^{19} - 10^{20}$ cm^{-3} [57]. For hydrogenated amorphous silicon a-Si:H the density reduces to $10^{15} - 10^{16}$ cm^{-3} [58]. In a-Si:H, the highest quality silicon-hydrogen bonds are single, so-called mono-hydride (Si:H) bonds [59].

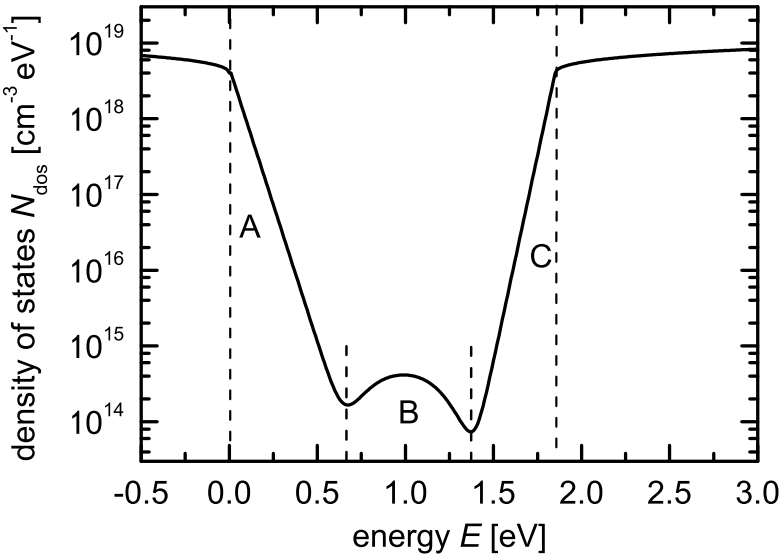

Fig. 4.1: Density of states of a-Si:H calculated by a standard model [56]. The spatial disorder in a-Si:H causes a spatially disordered potential energy leading to a broadening of the valence and the conduction band into the band gap (tails, regions A and C). Structural defects (dangling bonds) are responsible for energy states within the middle of the band gap (region B). The figure is provided by courtesy of Al Tarabsheh [55].

4.2 Intrinsic amorphous silicon i-a-Si:H

The back contact sketches in Figs. 2.6b,c show that an i-a-Si:H layer is necessary for the fabrication of the double and triple layer back contact. This section summarizes the experiments to achieve homogeneous i-a-Si:H layers. The i-a-Si:H depositions of this work use a silane flow of $[SiH_4] = 10$ sccm, an additional hydrogen flow of $[H_2] = 10...100$ sccm, a chamber pressure $p = 0.26...0.53$ mbar and a glow discharge power $P_I = 8$ mW cm^{-2}. The i-a-Si:H growth rate is about 5 to 7.5 nm/min depending on the hydrogen flow. Adding hydrogen lowers the growth rate.

The role of the i-a-Si:H layer in a heterojunction device is to supply a well passivated p-c-Si surface, i.e., to cause a low recombination velocity for electrons.

Thus, it plays the key role to reach high open circuit voltages in heterojunction solar cells. Unfortunately, the i-layer also decreases the fill factor of the cell by increasing its series resistance. The photovoltaic output parameters of solar cells presented in chapter 6 show that the i-a-Si:H thickness range that enables to reach high open circuit voltages *and* low series resistances is extremely small. Only an i-a-Si:H layer thickness around 2 to 3 nm yields a satisfactory c-Si surface passivation while marginally increasing the cell's series resistance. A good homogeneity of the i-a-Si:H layer is therefore an essential prerequisite for the fabrication of high-efficiency heterojunction solar cells. The optimization of the i-a-Si:H deposition conditions towards a perfect homogeneity is an important issue of this thesis. The following deposition parameters have an impact on the homogeneity of an a-Si:H layer:

- The *deposition pressure* has the strongest influence on the homogeneity and is varied between $p = 0.07...0.8$ mbar.
- The *gas flow* determines the time period that the gases remain within the chamber and influences the deposition rate as well as the homogeneity. The gas flows in this thesis range around 1...200 sccm.
- Depending on the *distance between the electrodes* and the *applied plasma frequency*, standing waves form within the deposition chamber and influence the homogeneity.
- The *glow discharge power* mainly changes the deposition rate but also influences the homogeneity. Depending on the applied power, local charges within the substrate or the substrate holder appear causing electric fields that locally change the deposition conditions.
- The *substrate holder and the substrate* if conductive or isolating or whether one or both are coated with a conductive or isolating layer has an impact on the deposition rate and the homogeneity.

When depositing amorphous silicon onto crystalline silicon, especially for a few nanometer thin layers, it is very hard to detect the exact thickness not to mention spatial inhomogeneities by conventional measurements that base on optical interferences. Scanning Electron Microcopy (SEM) is no alternative, because one can not detect the difference between crystalline and amorphous material. Measuring the

a-Si:H thickness on c-Si is possible by Transmission Electron Microcopy (TEM), but this technique is very complex and time consuming. Additionally, only an area of a few micrometers can be measured, making it impossible to detect spacial inhomogeneities.

The present thesis deposits 100 nm - 1 μm thick a-Si:H layers on glass substrates to investigate the homogeneity and to determine the deposition rate from measurements based on opt. interferences. However, glass has different electrical and surface properties than crystalline silicon and an a-Si:H layer that grows homogenously on glass not necessarily grows homogeneously on c-Si. For the investigation of the a-Si:H homogeneity on c-Si the spatially resolved effective lifetime measurement is used. Such samples use the fact that i-a-Si:H coated areas of a wafer exhibit an increase in effective lifetime that depends on the i-a-Si:H layer thickness. The investigations show, that the increase in effective lifetime saturates after surpassing an i-a-Si:H layer thickness of about 6 nm. Hence, depositing i-a-Si:H layers with a thickness *below* 6 nm allows to detect spatial inhomogeneities on the wafer by spatial resolved effective lifetime measurements.[1]

As an example showing the different homogeneities at different pressures, Figs. 4.2a,b depict the spatially resolved effective carrier lifetime of two i-a-Si:H coated c-Si wafers. Dark colors stand for high effective lifetimes and vice versa. The i-a-Si:H layer thickness d_i for both wafers is only $d_\mathrm{i} \approx 3$ nm allowing to detect already a slight thickness inhomogeneity by a change in the measured effective lifetime. The wafers are processed with two distinct pressures. Wafer 4.2a has lower lifetimes in the center and thus the i-a-Si:H thickness in the center is lower. For wafer 4.2b the opposite holds and the lifetime, respectively the i-a-Si:H thickness, is higher in the center.

4.2.1 Influence of the substrate holder potential

The PECVD is a deposition technique that uses an electromagnetic field. The electrical potential distribution within the deposition chamber therefore plays an important role for the layer deposition rate and homogeneity. Experiments with electrically isolated and grounded wafer holders are performed to find out the influ-

[1] I would like to express my gratitude to Markus Hlusiak who performed all the spatially resolved effective lifetime measurements.

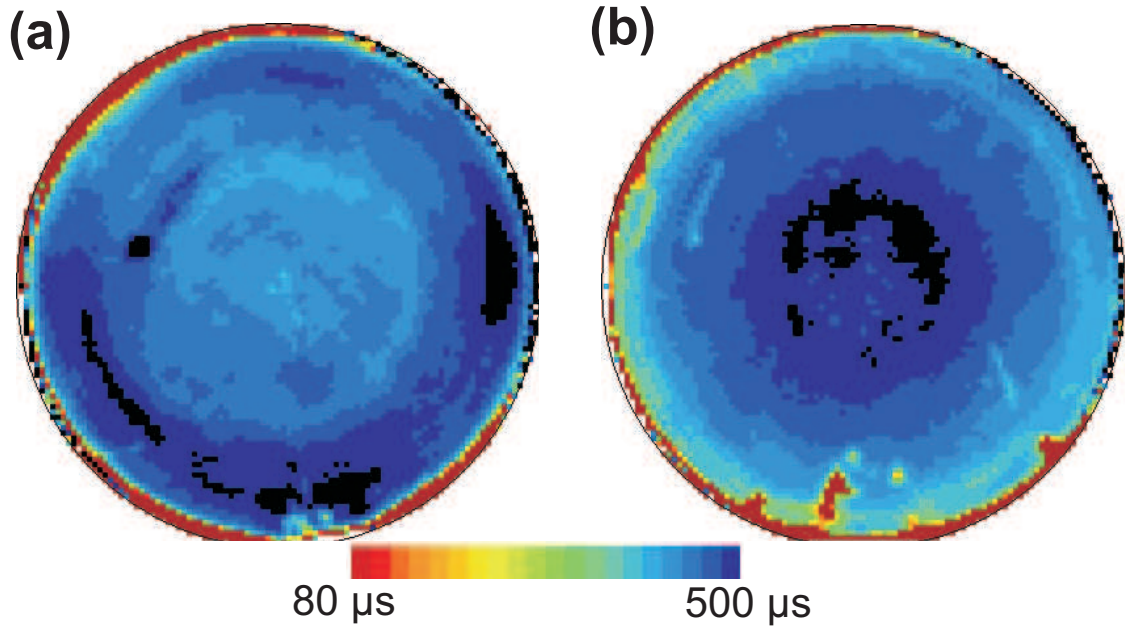

Fig. 4.2: Spatially resolved effective lifetime of two i-a-Si:H coated wafers showing the dependence of the a-Si:H deposition homogeneity on the deposition pressure. Dark colors stand for high effective carrier lifetimes and vice versa. The i-a-Si:H layer thickness is about 3 nm so that a spatial inhomogeneity can be detected in the spatial distribution of the effective lifetime. Both samples are processed with two distinct pressures, sample (a) has higher lifetimes i.e. a thicker i-a-Si:H layer at the edge whereas sample (b) has higher lifetimes i.e. thicker i-a-Si:H layer in the center.

ence of the electrical substrate potential on the deposition conditions.

Figure 4.3a shows a sketch of the deposition with an isolated substrate holder and Fig. 4.3b with a grounded substrate holder. In the case of an isolated substrate holder, an electrical potential on the holder occurs during the deposition. The potential arises in dependence of the deposition conditions, mainly the applied excitation power and frequency.

For the investigation of the electrical holder potential on the a-Si:H homogeneity, I fabricate i-a-Si:H coated lifetime samples. As for the samples in Figs. 4.2a,b, the i-a-Si:H layer thickness on the wafers is again about $d_i \approx 3$ nm allowing to detect already a slight thickness inhomogeneity via the spatial distribution of the effective lifetime. Figures 4.4a-d depict the spatially resolved effective carrier life-

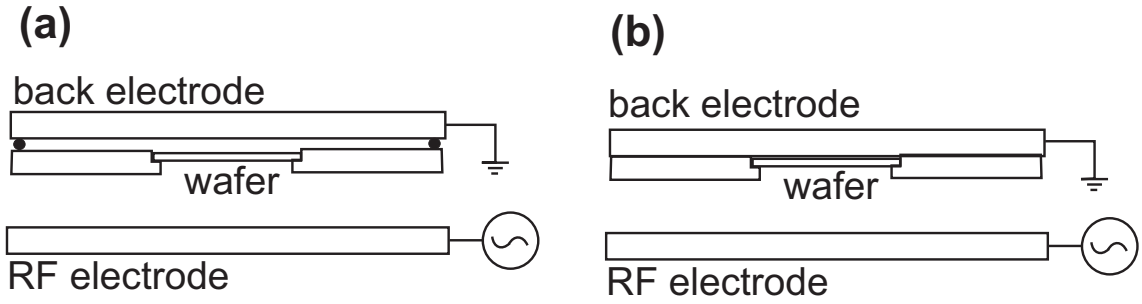

Fig. 4.3: Sketch of two different deposition conditions. (a) Isolated substrate holder. The electrical potential on the substrate and the holder arises depending on the plasma conditions. (b) Grounded substrate holder.

time of four i-a-Si:H coated c-Si wafers fabricated with the two different substrate potentials. Dark colors stand for high effective lifetimes and vice versa.

The wafers in Figs. 4.4a,b are fabricated with a grounded substrate holder, the wafers in Figs. 4.4c,d with an isolated substrate holder. The difference in between the two wafers fabricated with the same holder configuration is the deposition pressure. The wafer in Fig. 4.4a is fabricated with a pressure of 0.32 mbar, the wafer in Fig. 4.4b with a pressure of 0.52 mbar. The wafers in Figs. 4.4c,d are fabricated with a pressure of 0.65 mbar and 0.71 mbar respectively.

The grounded holder leads to a more even but somehow random distributed i-a-Si:H thickness throughout the wafer. All depositions for the solar cell back- and front contacts are therefore performed with a grounded substrate holder. The low effective lifetime on the left hand side of the wafer in Fig. 4.4a and on the bottom of the wafer in Fig. 4.4b stems from their handling with tweezers prior to the deposition. The c-Si wafer surface quality decreases heavily after a direct contact with other materials. The surface area that has been exposed to such a contact can often not be passivated any more. Drying of water-drops on the wafer surface also lead to a decreased c-Si surface quality.

With an isolated holder, the i-a-Si:H layer is always thicker in the center of the wafer independent from the deposition pressure. The concentric form of the layer thickness distribution indicates that the electrically conductive holder influences the a-Si:H deposition on the semiconducting wafer. The substrate holder is made of stainless steel and has therefore a much higher conductivity than the wafer.

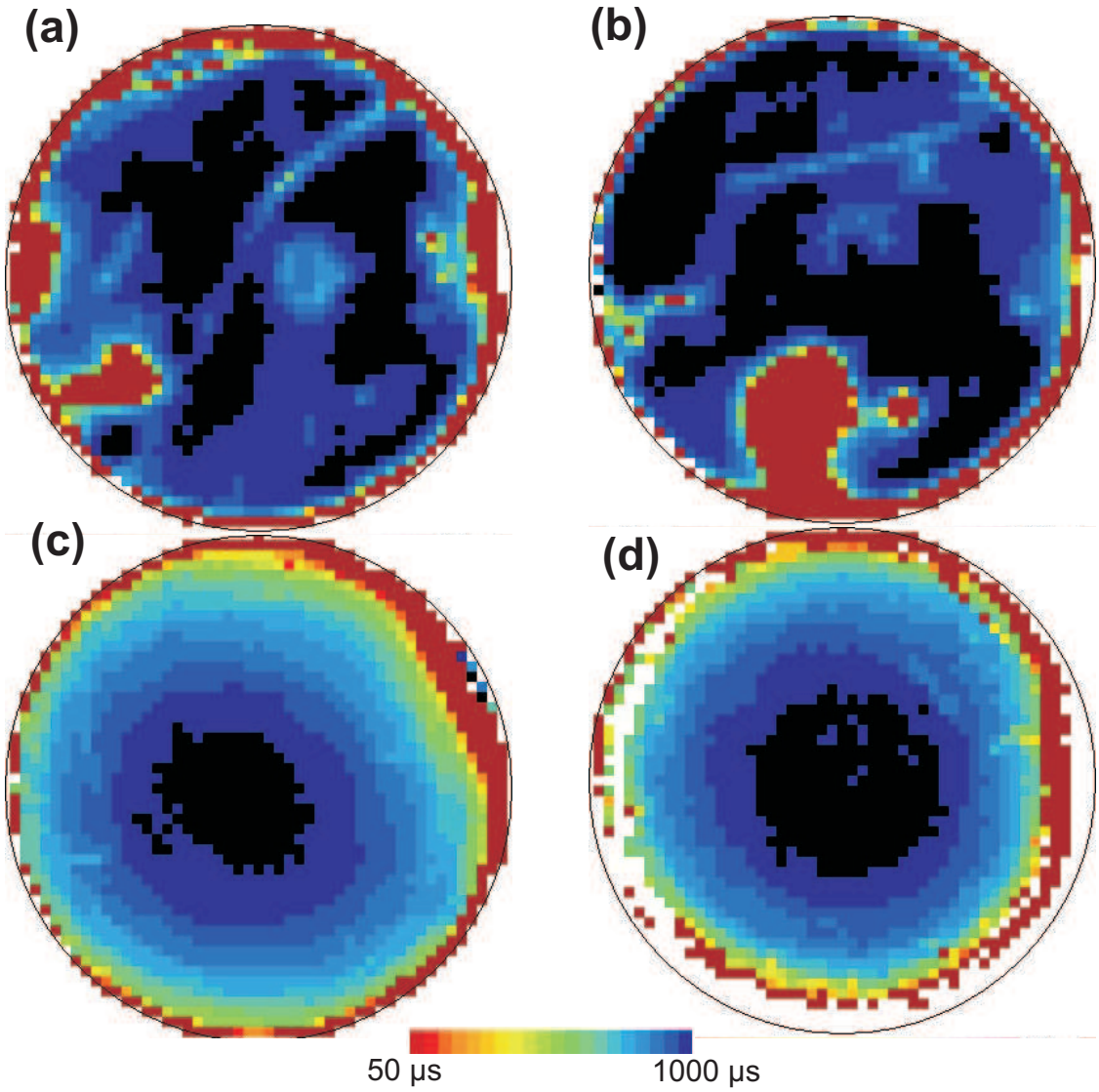

Fig. 4.4**:** Spatially resolved effective lifetime of four i-a-Si:H coated wafers showing the influence of the substrate potential on the a-Si:H distribution throughout the substrate. Dark colors stand for high effective carrier lifetimes and vice versa. The i-a-Si:H layer thickness is kept around 3 nm allowing to detect already a slight spatial inhomogeneity. Samples (a) and (b) are processed with grounded holders, samples (c) and (d) with isolated holders. The depositions with an isolated holder always lead to higher lifetimes, i.e. thicker a-Si:H layers, in the center of the wafer. The grounded holder creates a more even but slightly random distributed a-Si:H thickness throughout the wafer.

4.3 Growth of p-type amorphous and microcrystalline silicon

The sketches of the back contacts in Figs. 2.6a-c show, that all back contact types incorporate p-type microcrystalline Si. The triple layer back contact, Fig. 2.6c, additionally uses a p-type amorphous Si layer. This section summarizes the experiments to achieve homogeneous p-layers and a high active boron doping of the microcrystalline films. As section 6.3 shows, a high active doping of the microcrystalline Si is essential to achieve a low Ohmic contact resistance.

P-type and n-type doping of hydrogenated amorphous silicon by the addition of doping gases to the silane process gas was studied first by Spear et al. [60]. For p-type silicon, boron is mostly used as the dopant. Tsai et al. fabricate hydrogenated Si-B alloys by PECVD through the whole binary system [61]. They observe that the Fermi level is near mid-gap at the two ends of the binary system a-Si:H and a-B:H. For all alloy compositions, E_{F} moves close to the valence band indicating a self-doping with acceptors. The concentration of defects strongly increases with the doping level. Hence, the energy position as well as the density of the defects are both controlled by the position of the Fermi level E_{F} [62–64]. If the boron dopant density in the gas phase is too high, a clustering of boron atoms within the a-Si:H layer occurs [65].

For the fabrication of p-a-Si:H layers in this thesis, the doping gas B_2H_6 is added to the silane (SiH_4) gas during the deposition. The dilution of the doping gas is 2 % B_2H_6 in SiH_4. Adding hydrogen during growth influences the deposition rate, the homogeneity and the conductivity of the layer. For the VHF-PECVD (ν_{p} = 80 MHz) the addition of hydrogen causes a transition from amorphous to microcrystalline like growth after surpassing a hydrogen dilution range R_{H} = [H_2] / [B_2H_6 + SiH_4] ≈ 10-30 [45]. Figure 4.5 shows the homogeneity deviation and the deposition rate of p-type a-Si:H layers deposited with VHF-PECVD (ν_{p} = 80 MHz, Figs. 4.5a and 4.5b), and with RF-PECVD (ν_{p} = 13.56 MHz, Figs. 4.5c and 4.5d) plotted versus the hydrogen dilution. The graph only serves as a guideline to achieve homogeneous p-layers in the *ipe* reactor. Kindly note that the findings *cannot* be transferred to another deposition system with a different geometry. All layers are deposited on glass substrates. I use two diferent hydrogen fluxes [H_2] = 150 sccm and [H_2] = 200 sccm, a glow discharge power P_{I} = 80 mW cm^{-2} and vary

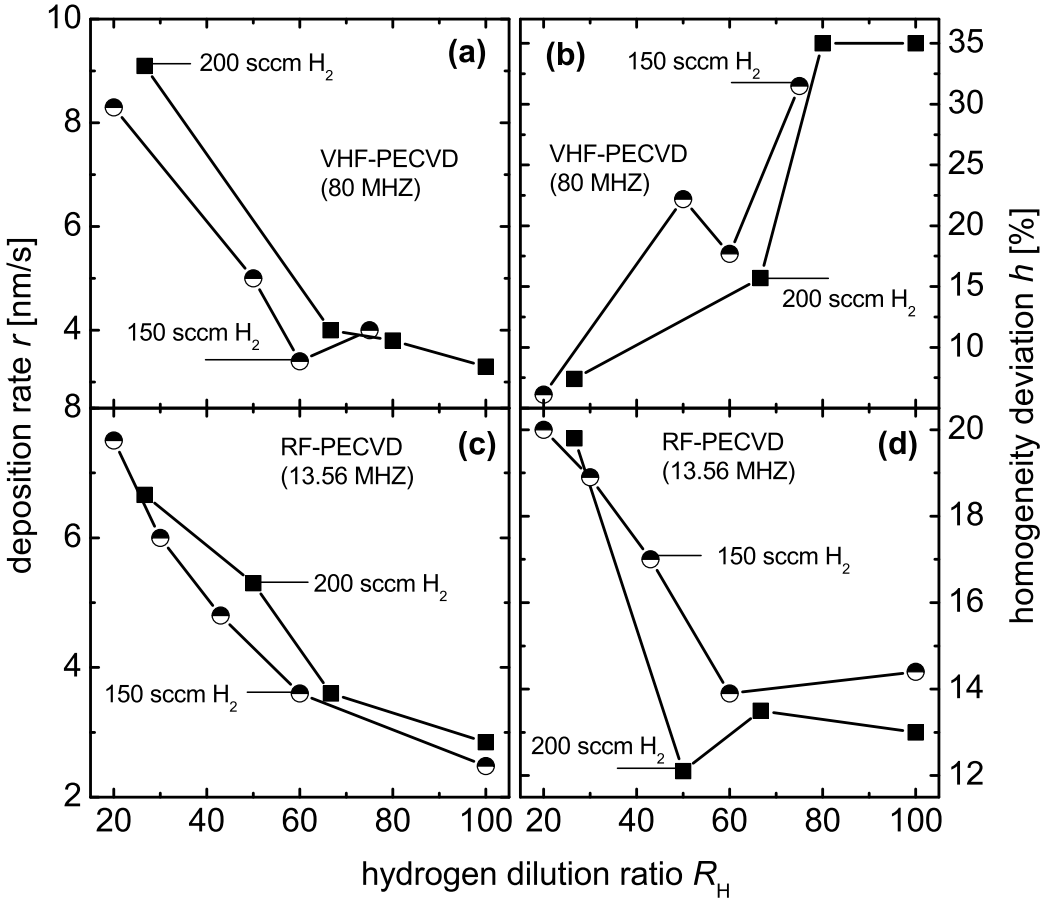

Fig. 4.5**:** Homogeneity deviation and deposition rate of p-a-Si:H layers deposited on glass substrates. (a),(b) show depositions with VHF-frequency $\nu_p = 80$ MHz; (c),(d) show depositions with RF-frequency $\nu_p = 13.56$ MHz. The hydrogen flux is hold at $[H_2] = 150$ sccm and $[H_2] = 200$ sccm, the silane diluted B_2H_6 doping gas flux is varied. To achieve as homogeneous layers a-Si:H layers as possible with $\nu_p = 13.56$ MHz, it is recommended to use $[H_2] = 200$ sccm and $R_H = 50$. For the VHF-frequency ($\nu_p = 80$ MHz), the best homogeneity is achieved with a low hydrogen dilution. However, the back contacts use a micro-crystalline layer that forms only after surpassing $R_H = 40$ as Fig. 4.6 shows. For a satisfying homogeneity, it is therefore recommended to use $[H_2] = 200$ sccm and $R_H = 66$ when depositing with the VHF-frequency. Kindly note that these findings are guidelines for the *ipe* reactor and cannot be transferred to another deposition system that uses a different geometry. The decrease in deposition rate shown in charts (a),(c) for increasing hydrogen dilutions is ascribed to etching during deposition caused by the large amount of hydrogen radicals [45]. Lines are guides to the eye.

the Silane diluted doping gas flux. The deposition rate is derived from transmission measurements at three distinct points on the glass substrate. The calculation uses the arithmetic mean of the layer thickness at these three points and divides it by the deposition time to derive an averaged deposition rate. The thickness homogeneity deviation is calculated by

$$h = \left(\frac{d_{\mathrm{MAX}}}{d_{\mathrm{MIN}}} - 1 \right) \times 100, \tag{4.1}$$

with d_{MAX} as the thickness of the thickest area and d_{MIN} as the thickness of the thinnest area. Thus, a lower homogeneity deviance stands for a better homogeneity. All VHF-PECVD depositions in Figs. 4.5a,b are carried out at a chamber pressure of $p = 0.53$ mbar. All RF-PECVD depositions in Figs. 4.5c,d are carried out at a chamber pressure of $p = 0.8$ mbar. The distinct chamber pressures for RF and VHF are a result of two particular local minima for the homogeneity deviation. That means, changing the chamber pressure from these particular values for RF and VHF leads to a stronger inhomogeneity. In summary, Figs. 4.5a-d show:

- The deposition rate decreases with increasing hydrogen dilution ratio R_{H} independently of the deposition frequency.
- At the same dilution ratios R_{H}, the growth rate is higher for a gas flow of $[H_2]$ = 200 sccm than for $[H_2]$ = 150 sccm.
- The homogeneity behaves oppositely for the two distinct frequencies. For the VHF-PECVD, the best homogeneity is reached with low R_{H} and for the RF-PECVD, the best homogeneity is reached with high R_{H}.

Concerning the microcrystalline p-layers, a second important parameter for the use in a heterojunction back contact apart from the deposition homogeneity is the conductivity, respectively the active boron doping. Figure 4.6 shows the conductivity and the conductivity activation energy of p-layers deposited with the VHF-frequency ($\nu_{\mathrm{p}} = 80$ MHz) on Corning glass. The conductivity activation energy E_{a} of an undoped a-Si:H film ranges around mid-gap $E_{\mathrm{a}} = 0.6 - 0.9$ eV [66]. The lower the activation energy E_{a} and the higher the conductivity σ, the higher is the active doping. Performance of secondary ion mass spectroscopy (SIMS) derives a boron density c_{B} of about $c_{\mathrm{B}} = 7$ x 10^{19} cm^{-3} for all layers depicted in Fig. 4.6. The

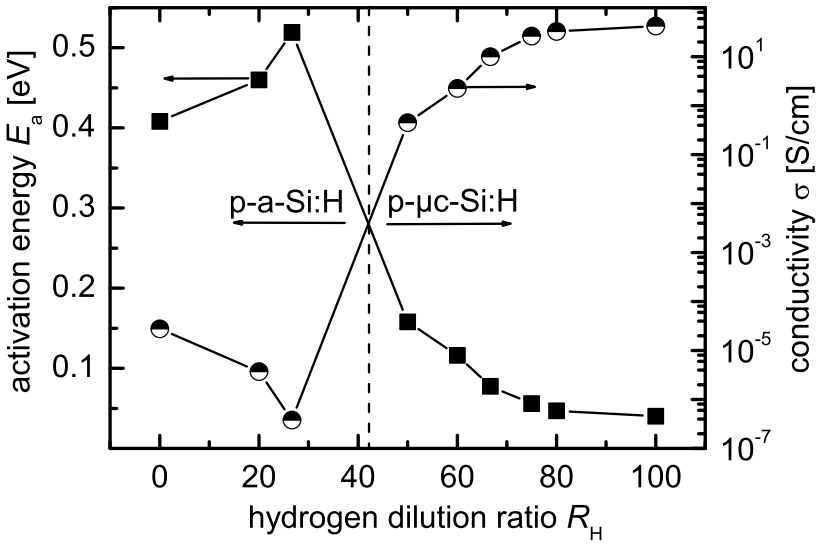

Fig. 4.6: Conductivity and activation energy of p-layers fabricated with the VHF-frequency (ν_p = 80 MHz) using a glow discharge power of P_l = 80 mWcm^2. The conductivity is low for low hydrogen dilutions. After surpassing a certain hydrogen dilution ratio, the conductivity rises strongly. Secondary mass spectra measurements using layers deposited with high and low hydrogen dilutions yield the same *boron concentration*. The steep conductivity rise towards high hydrogen dilutions is caused by a phase transition from amorphous like growth to microcrystalline like growth. The micro-crystals have a higher *active* doping than the pure amorphous matrix, leading to a higher conductivity of the micro-crystalline films. Lines are guides to the eye.

finding that all layers have the same boron concentration but exhibit different conductivities indicates, that the amount of boron that is *active* as a donor increases with increasing hydrogen dilution. The graph shows that the conductivity strongly depends on the hydrogen dilution ratio R_H. After surpassing a hydrogen dilution ratio of $R_H \geq 40$, the conductivity rises steeply. Depositions with hydrogen dilutions above $R_H \geq 20$ with $\nu_p = 80$ MHz cause a phase transition from amorphous to microcrystalline like growth. i.e. the amount of micro-crystals within the amorphous matrix steadily increases. This is ascribed to the increasing crystallinity of

the layer. The micro-crystals have a much higher active doping than the pure amorphous matrix, leading to a higher conductivity of the μc-Si:H if compared to the pure a-Si:H. The layer with the highest doping is fabricated with $R_{\mathrm{H}} = 100$ and has a conductivity $\sigma = 42$ S/cm. When using this conductivity as the conductivity of a fictive c-Si wafer and calculating the fictive boron dopant density N_{A} in this wafer I derive $N_{\mathrm{A}} = 4$ x 10^{19} cm^{-3}. This result shows that nearly all boron atoms in the p-μc-Si:H layer fabricated at $R_{\mathrm{H}} = 100$ are active as donors. Note that for our experimental setup, we do not observe a change in conductivity *independent* of the hydrogen dilution ratio for depositions using the RF-frequency ($\nu_{\mathrm{p}} = 13{,}56$ MHz). There is no phase transition, and the layers are always amorphous.

Chapter 5

Wafer passivation with a-Si:H

This chapter shows the experimental optimization of a-Si:H depositions on wafers to achieve homogeneous and well passivated a-Si:H/c-Si interfaces. A good and homogeneous c-Si surface passivation is an essential ingredient for the fabrication of high efficiency solar cells. A well passivated surface yields a low surface recombination velocity leading to a high solar cell open circuit voltage. The chapter starts with a literature survey on c-Si surface passivation. Subsequently, the chapter presents experimental results using i-a-Si:H and p-a-Si:H for surface passivation of p-c-Si wafers. The last part of this chapter estimates the open circuit voltage of virtual solar cells derived from symmetrically passivated c-Si samples.

5.1 Literature survey: c-Si surface passivation

References [67, 68] give a general review of c-Si surface passivation. Amorphous silicon, pure or with added nitrogen, oxygen or carbon, is up to now the only efficient way for the *low-temperature* passivation of a c-Si surface ($T \leq 400°C$). For some solar cell processes, as for example the *ipe* transfer process [69, 70], only low temperature processing of the back contact is possible. Several research groups are studying the a-Si:H/c-Si surface passivation properties extensively and use different types of amorphous silicon. Schmidt et al. used hydrogenated amorphous silicon-nitride a-$Si_{1-x}N_x$:H deposited at process temperatures $300°C \leq T \leq 400°C$ and reach recombination velocities $S \leq 10$ cm/s [71]. Martín et al. used hydrogenated amorphous silicon carbide a-SiC_x:H as a c-Si surface passivation layer

reaching $S \leq 30$ cm/s [72]. With pure amorphous silicon a-Si:H, in particular intrinsic films lead to a high quality c-Si surface [1]. Dauwe et al., for example, achieved very low recombination velocities $S \leq 10$ cm/s already at i-a-Si:H deposition temperatures of $200°C \leq T \leq 250°C$ [73]. Froitzheim et al. explored the influence of wet-chemical wafer surface pre-treatments carried out prior to the a-Si:H deposition on the a-Si:H/c-Si interface recombination properties [74]. In contrast, Martín et al. avoided all wet-chemical wafer pre-treatments [75]. They removed the native oxide on the wafer surface prior to the a-Si:H deposition inside the deposition chamber by a short treatment with a pure hydrogen plasma. The hydrogen thereby etches the SiO_2 from the wafer surface. Extended analysis on the injection dependence of the effective surface recombination velocity S_{eff} of a-Si:H coated wafers was carried out by Garin et al. [76]. They analyzed the physical parameters of the interface recombination and proposed a model to calculate $S_{\text{eff}}(\Delta n)$. Olibet et al. proposed a physical model of amphoteric defects to explain the high surface recombination in a-Si:H/c-Si interfaces at low injection densities [77].

The present work optimizes the i-a-Si:H deposition conditions to reach a good homogeneity throughout the wafer, an essential prerequisite for the fabrication of a-Si:H/c-Si solar cells, cf. chapter 4. Then, the thesis focuses on the influence of the i-a-Si:H and p-a-Si:H deposition conditions on the c-Si surface passivation quality. A good c-Si back side passivation is an essential ingredient for high efficiency a-Si:H/c-Si solar cells. For example, the influence of the deposition temperature and the hydrogen dilution during growth on the effective lifetime of a-Si:H coated samples is explored. With the a-Si:H layers optimized with respect to homogeneity and back side passivation quality, lifetime samples that use i/p-a-Si:H layer stacks are fabricated. The samples have the same structure as the back contacts of the solar cells that are shown in Figs. 2.6a-c. Such samples allow to determine the i/p-layer scheme that supplies the highest effective lifetime. Note that for high performance a-Si:H/c-Si solar cells, the intrinsic layer has to be as thin as possible to ensure a low series resistance but it *has* to be inserted to achieve a high quality c-Si surface. Hence, I fabricate samples with decreasing i-a-Si:H layer thickness with the best i/p-a-Si:H layer system. These i/p-a-Si:H samples enable to analyze the surface passivation quality in dependence of the i-a-Si:H layer thickness.

5.2 Samples

If not denoted otherwise, the effective lifetime samples use 250 μm thick boron doped float-zone Si wafers with a resistivity of $\rho = 1$ Ωcm. The resistivity corresponds to a doping level of about $N_{\mathrm{A}} = 1.5 \times 10^{16}$ cm^{-3}. Such medium boron doped float-zone wafers typically have bulk lifetimes τ_{b} well above $\tau_{\mathrm{b}} = 1$ ms. The wafers are taken as supplied from the box and the native oxide is removed by a dip in 5 % aqueous HF solution for 10 s. Subsequently, the samples are mounted into the PECVD vacuum cluster setup. After the sample fabrication, the effective minority carrier lifetime τ_{eff} measurement follows using the QSSPC technique. Section 3.1.3 describes this measuring setup. The effective lifetime in the following graphs is always extracted from the measurement spreadsheet at an injection level Δn that, according to the measurement system, corresponds to an illumination intensity of one sun under AM1.5G conditions.

5.3 Intrinsic a-Si:H surface passivation

As Figs. 2.6b,c show, the double and triple layer back contacts are equipped with an i-a-Si:H layer. Section 4.2 summarizes the experiments towards a good layer homogeneity, an essential prerequisite due to the fact that the layer thickness in the back contact ranges only around 3 nm. This section describes the optimization of the depositions towards a good c-Si surface passivation that is mandatory to reach high open circuit voltages in solar cells.

Figure 5.1 shows the passivation of the c-Si surface with i-a-Si:H. *Intrinsic* a-Si:H layers generally deliver the best c-Si surface passivation if compared to their phosphorus or boron doped counterparts and the i-a-Si:H layer therefore plays the key role to reach high efficiencies in heterojunction devices (comp. Fig. 5.7). The good c-Si surface passivation properties of i-a-Si:H is most likely caused by a low defect density distribution within the i-a-Si:H bandgap. A low defect state density in the i-a-Si:H bandgap leads to a low defect concentration at the i-a-Si:H/c-Si interface and therefore to a low c-Si surface recombination velocity [78].

Figure 5.2 shows the measured effective lifetime τ_{eff} (left ordinate) and the calculated maximum surface recombination velocity S_{MAX} (right ordinate) plotted versus the excess carrier density Δn of a wafer symmetrically equipped with a 30

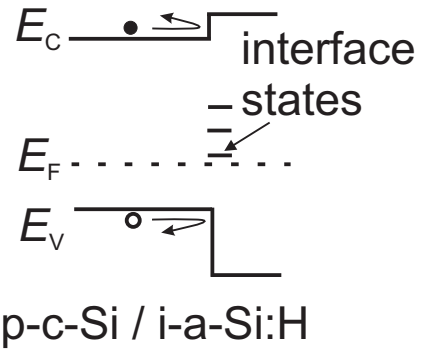

Fig. 5.1: Surface passivation of a wafer with i-a-Si:H. The low defect density of the i-a-Si:H creates a low concentration of interface states. Hydrogen additionally passivates the dangling bonds at the c-Si surface. The band offset in the valence and conduction band keeps mobile charge carriers from entering the a-Si:H layer and reaching the defect rich a-Si:H surface.

nm thick i-a-Si:H passivation layer. The i-a-Si:H layer on the wafer is the standard surface passivation layer of this thesis deposited with a silane flow of $[SiH_4] = 10$ sccm, a chamber pressure of 0.52 mbar, a plasma frequency of $\nu_p = 13.56$ MHz and a glow discharge power of 8.8 mW/cm^2. The sample shows a strong dependence of τ_{eff} on the injection density: For low Δn, the effective lifetime is also low. Then, τ_{eff} increases with increasing charge carrier density and saturates for this sample at $\Delta n = 1 \times 10^{15}$ cm^{-3} with $\tau_{eff} \approx 800\ \mu s$ before it decreases again. The curve characteristics of τ_{eff} in Fig. 5.2 is representative for all c-Si samples that are passivated with i-a-Si:H. The fact that the effective lifetime decreases for high injection levels $\Delta n > 1 \times 10^{16}$ cm^{-3} is known and stems from Auger recombination. The injection dependence for low $\Delta n < 1 \times 10^{15}$ cm^{-3} is caused by a injection dependence of the surface recombination velocity S. Taking into account the symmetric sample structure, i.e. both surfaces having the same recombination velocity $S_1 = S_2 = S$, neglecting bulk and Auger recombination I calculate S_{MAX} according to Ref. [79] as

$$S_{MAX} = \frac{d_{Si}}{2(\tau_{eff} - d_{Si}^2/(D_n \pi^2))}. \tag{5.1}$$

Here, d_{Si} is the wafer thickness. The right ordinate in Fig. 5.2 depicts the calculated S_{MAX}. To estimate the a-Si:H/c-Si surface recombination velocity for a typical solar cell application case, I calculate S_{MAX} for an injection level $\Delta n = 2 \times 10^{15}$ cm^{-3}

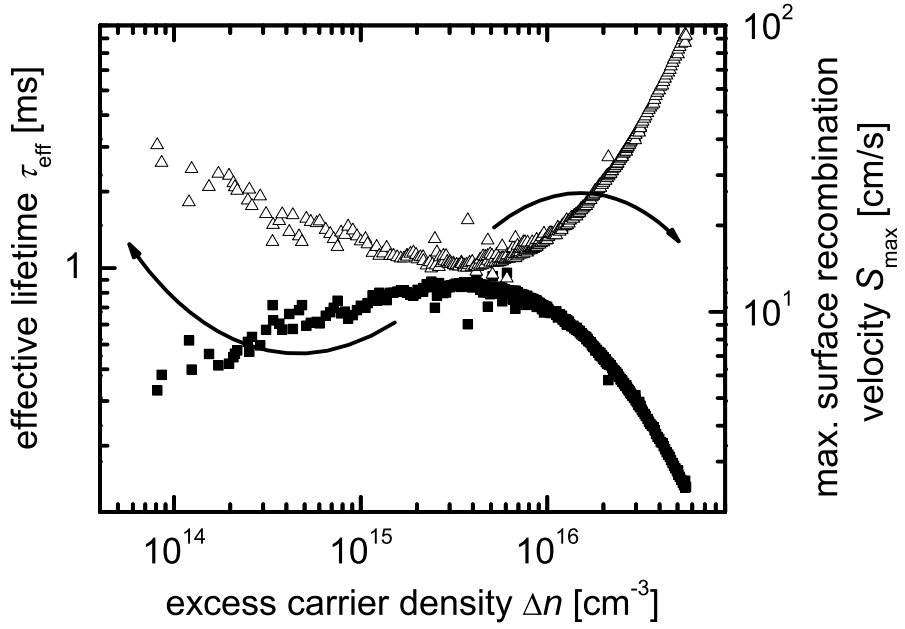

Fig. 5.2: Measured effective lifetime τ_{eff} and maximum surface recombination velocity S_{MAX} calculated from Eq. (5.1) of a wafer symmetrically equipped with a layer of intrinsic amorphous Si (thickness $d_i = 30$ nm). At low excess carrier density, τ_{eff} is low and therefore S_{MAX} high due to amphoteric defects [77]. With increasing injection level, these defects are saturated and τ_{eff} increases. At high injection densities $\Delta n > 10^{16}$, τ_{eff} decreases again due to intrinsic Auger recombination.

that corresponds to an impinging light intensity of one sun under AM1.5G conditions for a solar cell with open terminals. With the minority carrier diffusion constant $D_n = 27$ cm^2/s and $d_{Si} = 250$ μm I find $S_{MAX} \approx 20$ cm/s. The calculation of V_{oc} in Fig. 5.8 shows that such a low value of S_{MAX}, corresponding to a high effective lifetime $\tau_{eff} \approx 800$ μs, would allow to fabricate solar cells with open circuit voltages in excess of $V_{oc} = 700$ mV. The back side recombination velocity of industrial solar cells with screen printed Al back contact ranges around 500 cm/s $< S <$ 1000 cm/s [80]. Compared to that, the a-Si:H recombination velocity is more than one order of magnitude lower.

The i-a-Si:H layer for the sample of Fig. 5.2 is fabricated without adding H_2 during deposition. Due to the fact that hydrogen plays an important role for the c-Si surface passivation, one may conclude that an addition of hydrogen during the i-a-Si:H deposition leads to an even better c-Si surface passivation. However, it is important to note that the addition of hydrogen *above* a certain dilution ratio during the i-a-Si:H growth *lowers* its quality as a c-Si surface passivation layer. For c-Si samples equipped with i-a-Si:H layers deposited with hydrogen dilutions R = $[H_2]$ / $[SiH_4] > 20$ the measured effective lifetimes are lower than $\tau_{\text{eff}} \leq 100$ μs.

I explain the finding that addition of hydrogen during the i-Si:H deposition *above* a certain threshold value leads to a lower effective lifetime along the following line of arguments: Wang et al. showed by effective lifetime measurements and transmission electron microscopy that the best minority carrier lifetime in i-a-Si:H coated wafers is achieved if an immediate *amorphous* growth of the intrinsic passivation layer on the c-Si surface is ensured [81]. The growth of a-Si:H with hydrogen diluted silane increases the *crystalline* fraction in the amorphous matrix [45]. Hence, the reason for the reduced passivation quality that I observe when growing i-a-Si:H with a hydrogen dilution hydrogen dilutions R = $[H_2]$ / $[SiH_4] > 20$ lies in the higher crystalline fraction of these films. As Wang et al. showed, more crystalline-like growth also means a more epitaxial-like growth on the crystalline wafer surface [81]. My explanation for the lower lifetime of epitaxial like grown i-a-Si:H layers is the following. The more epitaxial-like the films grow, the higher the charge carrier mobility and the smaller the band offset at the μc-Si:H/c-Si interface leading to an increased diffusion of minority carriers to the defect rich μc-Si:H layer surface.

5.3.1 Influence of a surface pre-cleaning step

The effective lifetime of a-Si:H coated wafers with the same bulk properties also depends on the surface condition of the wafer prior to the a-Si:H deposition. Figure 5.3 shows τ_{eff} of c-Si samples with differently treated surfaces. Four samples are cleaned with a standard four-step process, commonly referred to as the RCA clean, consisting of a treatment with an alkaline solution containing ammonium hydroxide followed by a water rinse and an acid solution containing hydrochloric acid followed again by a water rinse [82]. The oxide grown during the cleaning steps is removed in between the cleaning steps either with HF or BHF. Two of the samples are taken

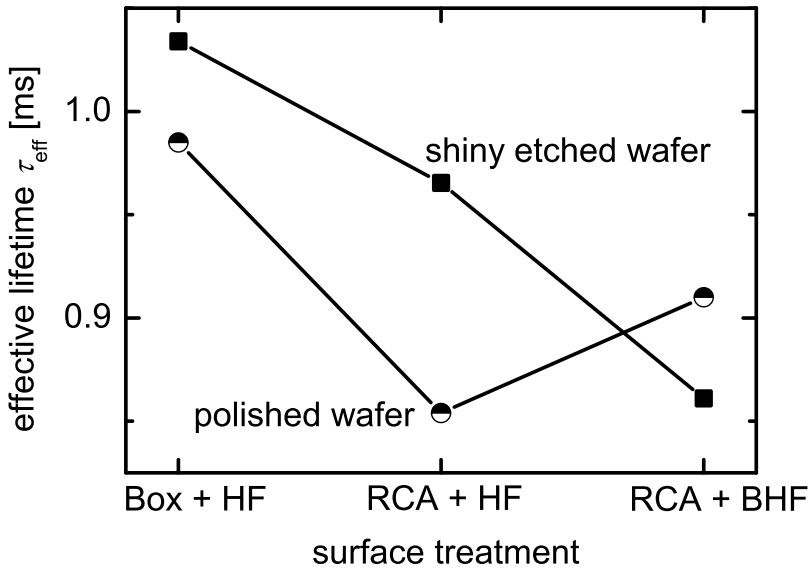

Fig. 5.3: Effective lifetime τ_{eff} of i-a-Si:H coated p-type wafers with surfaces that are differently treated prior to the a-Si:H deposition. The samples are symmetric with a layer of i-a-Si:H (thickness $d_{\mathrm{i}} = 30$ nm) on each side. The graph shows that a polished and a shiny etched wafer surface yields similar lifetimes. A RCA pre-cleaning step after taking the wafers as delivered from the box decreases the effective lifetime.

as delivered from the box, and the native oxide is removed with an HF dip. As the measurements show, a pre-cleaning step reduces the effective lifetime. Shiny etched wafers are slightly superior to polished wafers.

5.3.2 Influence of the deposition temperature

Annealing of an a-Si:H layer influences its optical properties and also changes the defect density in the layer as well as affects other material properties [83–85]. Heating above a temperature of 500 °C usually induces a transition into the thermodynamically stable crystalline phase. Figures 5.4a,b show that the surface passivation quality of an a-Si:H/c-Si interface is influenced by both, the a-Si:H deposition tem-

perature and by a post-deposition anneal. Figure 5.4a depicts a sample that is

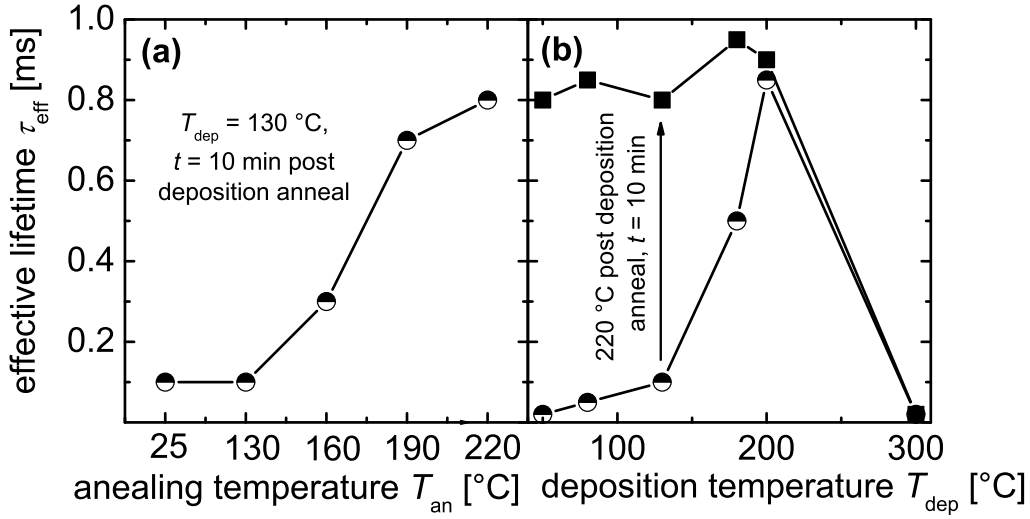

Fig. 5.4**:** Effective lifetime τ_{eff} of i-a-Si:H coated wafers. (a) shows the effect of a post deposition anneal on one sample. The sample is fabricated with a deposition temperature $T_{\text{dep}} = 130$ °C and subsequently annealed at different annealing temperatures T_{an} in ambient air. Annealing at a temperature of $T_{\text{dep}} = 220$ °C leads to the highest effective lifetime, a finding that was previously reported by Rau et. al [86]. Annealing at higher temperatures does not increase τ_{eff}. After surpassing $T_{\text{an}} = 240$ °C, the effective lifetime decreases again (not shown in chart (a)). (b) shows six samples fabricated at different deposition temperatures T_{dep} and subsequently annealed with an annealing temperature $T_{\text{an}} = 220$ °C for 10 min in ambient air. A high effective lifetime of $\tau_{\text{eff}} \approx 800\ \mu s$ is reached after the annealing step, even when depositing the a-Si:H layers at temperatures as low as room temperature ($T_{\text{dep}} = 25$ °C). After surpassing a deposition temperature of $T_{\text{dep}} = 300$ °C, the lifetime decreases heavily. Hence, to reach high effective lifetimes it is either possible to deposit the a-Si:H layers at substrate temperatures *below* $T_{\text{an}} = 200$ °C and perform a subsequent sample annealing *at* $T_{\text{an}} = 220$ °C or to deposit the a-Si:H layers *at* substrate temperatures 200 °C $< T_{\text{dep}} <$ 300 °C *without* further annealing.

fabricated at a deposition temperature of $T_{\mathrm{dep}} = 130$ °C. The effective lifetime of the sample is measured as deposited and after different annealing steps. The annealing is carried out for a time $t = 10$ min on a hotplate in ambient air. The figure shows that τ_{eff} increases with increasing annealing temperature. The effective lifetime saturates at $T_{\mathrm{an}} = 220$ °C. After surpassing $T_{\mathrm{an}} = 240$ °C, τ_{eff} starts to decrease again (not shown in Fig. 5.4a).

Figure 5.4b depicts six sample that are fabricated at different deposition temperatures T_{dep}. The effective lifetime of the samples is measured as deposited and after an annealing step at $T_{\mathrm{an}} = 220$ °C for $t = 10$ min on a hotplate in ambient air. Figure 5.4b shows that the effective lifetime increases after the annealing step if the deposition temperature is *below* the annealing temperature. After surpassing a deposition temperature $T_{\mathrm{dep}} = 280$ °C, the effective lifetime decreases rapidly. Possibly, this decrease is caused by a more epitaxial like growth of the first i-a-Si:H nanometers on the c-Si surface. High lifetimes are only achieved with an abrupt junction between the crystalline wafer and the amorphous passivation layer [81].

5.4 Wafer surface passivation by i/p-a-Si:H layer stacks

Figures 2.6a-c show that all a-Si:H back contacts use p-type micro-crystalline layers. The triple layer back contact, Figs. 2.6b,c, as well incorporates a p-type film. This section summarizes the experiments with p-a-Si:H, p-μc-Si:H and i/p-layer stacks towards a good surface passivation that is mandatory to reach a high open circuit voltage with the high-efficiency solar cells from chapter 6.

Figure 5.5a shows the field effect p-c-Si surface passivation by a p^+-a-Si:H and Fig. 5.5b depicts the combination of both, surface passivation with i-a-Si:H and field effect by p^+-a-Si:H. This section firstly investigates the surface passivation quality of an i/p-layer stack as shown in Fig. 5.5b. The surface passivation of Si wafers with i-a-Si:H results from the minimization of interface defects. Addition of a p-type a-Si:H or μc-Si:H layer introduces an additional field effect, the BSF. The potential drop Φ_{BSF} exponentially reduces the concentration of excess electrons at

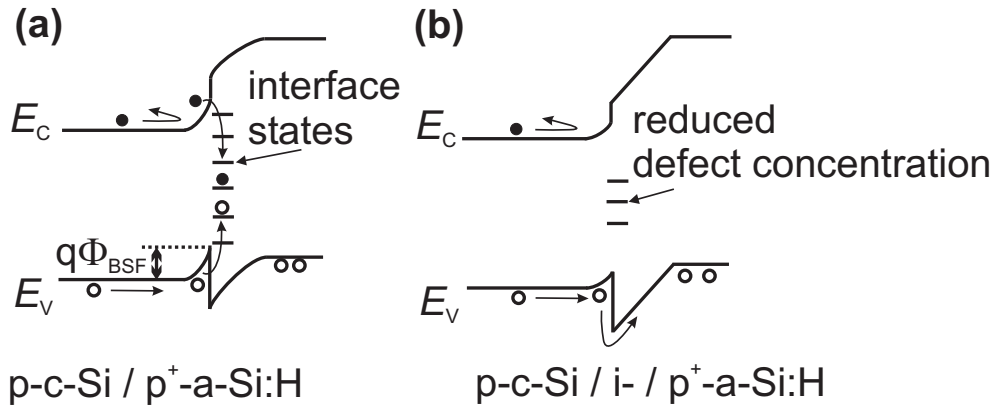

Fig. 5.5: (a) Wafer Surface passivation with an electric field created by a p^+-a-Si:H layer. (b) Surface passivation with an i-a-Si:H/p^+-a-Si:H layer stack that combines the field effect with a low defect concentration at the interface.

the c-Si/a-Si:H interface Δn_{int} by

$$\Delta n_{\mathrm{int}} = \Delta n_{\mathrm{bulk}} \exp\left(-\frac{q\Phi_{\mathrm{BSF}}}{kT}\right) \tag{5.2}$$

with respect to the bulk electron concentration Δn_{bulk}. Thus, the actual value of the recombination velocity at the interface S_{int} reduces to the effective value

$$S_{\mathrm{eff}} = S_{\mathrm{int}} \exp\left(-\frac{q\Phi_{\mathrm{BSF}}}{kT}\right). \tag{5.3}$$

Every 60 meV caused by a BSF reduces the interface recombination velocity approximately by a factor of ten. Figure 5.6 shows the effective lifetime of wafers coated with a 30 nm thick i-a-Si:H layer on one side and i/p-layer stacks on the other side plotted versus the p-a-Si:H hydrogen dilution. The i-layer is deposited with the standard conditions using a silane flow of $[SiH_4] = 10$ sccm, a chamber pressure of 0.52 mbar, a plasma frequency of $\nu_{\mathrm{p}} = 13.56$ MHz and a glow discharge power of 8.8 mW/cm^2. For the p-layers, I use the same two hydrogen fluxes $[H_2] = 150$ sccm and $[H_2] = 200$ sccm as for the test layers on glass substrates and vary the Silane diluted doping gas flux. The applied chamber pressure is $p = 0.53$ mbar and the glow discharge power is set to $P_{\mathrm{I}} = 80\ \mathrm{mW\,cm^{-2}}$ and the plasma frequency to $\nu_{\mathrm{p}} = 80$ MHz. As chapter 4 shows, such deposition conditions yield micro-crystalline silicon after surpassing a certain hydrogen dilution. For all samples, the thicknesses d_{i} of the

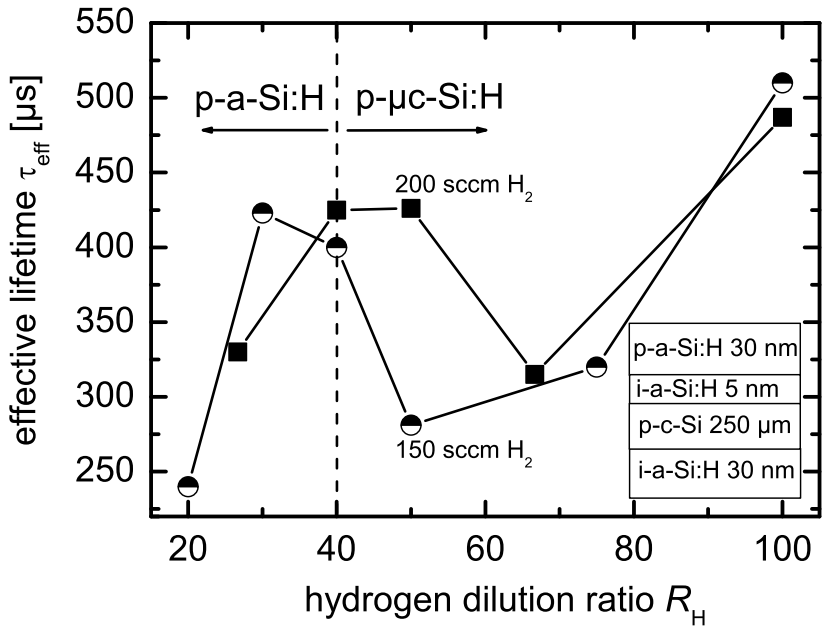

Fig. 5.6**:** Effective lifetime τ_{eff} of wafers that are coated with an i-a-Si:H layer on one side (thickness $d_{\text{i}} = 30$ nm) and with a double layer of i-a-Si:H (thickness $d_{\text{i}} \approx 5$ nm) and a p-layer (thickness $d_{\text{p}} = 30$ nm) on the other side. The graph shows that the deposition conditions of the p-layers influence the surface passivation quality. The highest effective lifetime is achieved if the p-layer is fabricated with a very high hydrogen dilution $R_{\text{H}} = 100$; a finding that is explained with the following arguments: Figure 4.6 shows that the p-layer deposited with a hydrogen dilution $R_{\text{H}} = 100$ has the highest doping level. A stronger p-layer doping causes a stronger back surface field potential drop Φ_{BSF} within the c-Si. Equation (5.3) explains that Φ_{BSF} decreases the surface recombination velocity exponentially, a larger Φ_{BSF} therefore allows for a higher effective lifetime τ_{eff}. Lines are guides to the eye.

i-layer and d_{p} of the p-layer in the i/p-double scheme are constant at $d_{\text{i}} \approx 5$ nm and $d_{\text{p}} \approx 30$ nm. Figure 5.6 shows that the effective lifetime rises with increasing hydrogen dilution. However, there is a lifetime drop for a hydrogen dilution $50 < R_{\text{H}} < 80$ that I interprete with the following argument: When deposing μc-Si:H with high hydrogen dilutions, an equilibrium between deposition and etching establishes in

the deposition chamber. Thereby, the very thin intrinsic layer is partly etched by the hydrogen, the surface passsivation decreases and the lifetime drops. However, this argument does not explain the rise in effective lifetime towards the very high hydrogen dilution $R_{\mathrm{H}} = 100$. The second lifetime rise is caused by the increased p-layer doping. At $R_{\mathrm{H}} = 100$, a very highly doped p-μc-Si:H layer grows. As a consequence, this layer causes the strongest band bending of all p-layers and creates the strongest potential drop Φ_{BSF} within the c-Si. According to Eq. (5.3), Φ_{BSF} decreases S_{eff} exponentially and a larger Φ_{BSF} therefore allows for a higher effective lifetime.

All i/p-passivation layer stacks in Fig. 5.6 use a 5 nm thick intrinsic layer. Chapter 6 shows that the use of such a intrinsic layer thickness in a solar cell back contact leads to a series resistance that is already too high to warrant a satisfying fill factor. As a next step, I therefore use the p$^+$-μc-Si:H layer deposited at $R_{\mathrm{H}} = 100$ that delivers the highest effective lifetime and study the influence of the i-a-Si:H thickness on the surface recombination velocity. The experiment is performed by the fabrication of i/p-passivated lifetime samples with decreasing i-a-Si:H layer thickness. Besides these lifetime tests with i-a-Si:H/p$^+$-μc-Si:H layer stacks, samples that use an i-a-Si:H/p-a-Si:H system to compare the passivation quality of the microcrystalline p-layer with the amorphous p-layer are fabricated. Two kinds of p-a-Si:H layers are investigated: One with a hydrogen dilution of $R_{\mathrm{H}} = 80$ and one without. In contrast to the p-layers of Fig. 5.6, these films are grown with a RF frequency $\nu_{\mathrm{p}} = 13.56$ MHz. Such deposition conditions yield amorphous material *independent* of the hydrogen dilution as pointed out in section 4.3.

Figure 5.7 shows the measured effective lifetime τ_{eff} of such samples plotted versus the intrinsic layer thickness. As for Fig. 5.7, the wafers are equipped on one side with a 30 nm thick i-a-Si:H layer and with an i/p-layer stack (varying i-layer thickness) on the other side. First of all, there seems to be no high quality surface passivation achievable with i/p-layer stacks for any i-a-Si:H layer thickness if the p-layer is grown without hydrogen dilution. De Wolf and Beaucarne [87] as well found that the passivation quality of 3 nm thin i-a-Si:H layers is destroyed by deposition of an additional p-a-Si:H layer grown without hydrogen dilution. In contrast, for the p$^+$-μc-Si:H layer, there seems to be a reasonable surface passivation quality for any thickness of the i-a-Si:H layer and even when omitting it. Thus, a passivation of the p-c-Si surface by a field effect, previously reported by Sakata et al. [88], caused

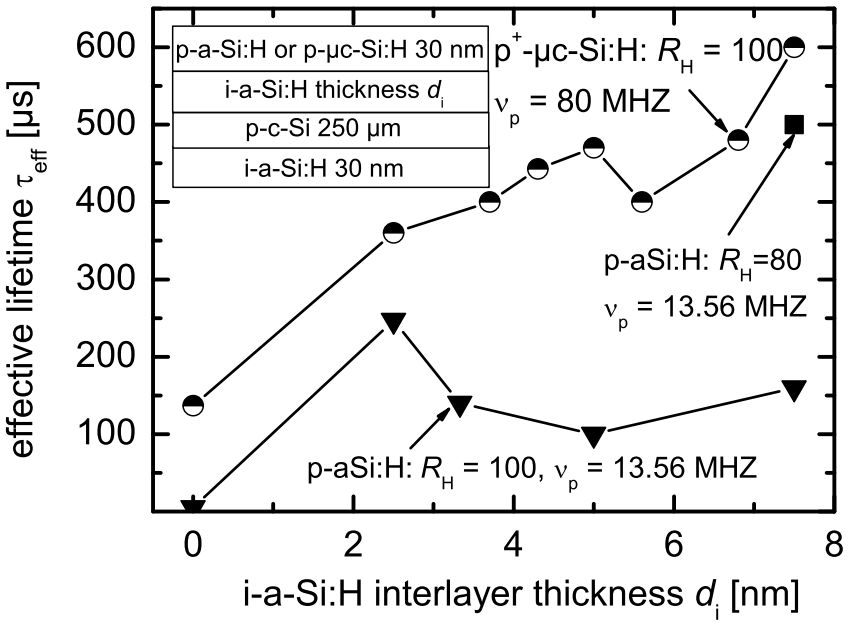

Fig. 5.7**:** Measured effective lifetime τ_{eff} plotted versus intrinsic layer thickness d_{i}. The samples use an i-a-Si:H layer (fixed thickness $d_{\text{i}} = 30$ nm) on one side and an i/p-layer stack with varying i-layer thickness on the other side. Two different p-layers are used: The p-μc-Si layer deposited with $R_{\text{H}} = 100$ that delivered the highest effective lifetime in Fig. 5.6 and, for comparison, a p-a-Si:H layer that is deposited without additional hydrogen dilution and with a plasma frequency of $\nu_{\text{p}} = 13.56$ MHz. The p-μc-Si layer yields always higher effective lifetimes than the p-a-Si:H layer, ascribed to its higher doping level. A higher doping level leads to a larger potential drop Φ_{BSF} that according to Eq. (5.3) reduces the surface recombination velocity exponentially. At an i-layer thickness of 7.7 nm, one additional wafer with a p-a-Si:H layer ($\nu_{\text{p}} = 13.56$ MHz) and an additional hydrogen dilution of $R_{\text{H}} = 80$ was fabricated. Note that, as explained in 4.3, such a p-a-Si:H layer has a much *lower* active doping than the p-μc-Si layer. Hence, the sample shows that not only the p-layer doping level affects the effective lifetime but also the hydrogen dilution level. Using a high hydrogen dilution, high effective lifetimes can be achieved with lowly doped p-layers as well. Hence, for all a-Si:H back contacts, cf. Figs. 2.6a-c, I use the p-μc-Si layer deposited with $R_{\text{H}} = 100$. For the triple layer back contact, I additionally use the p-a-Si:H layer deposited with a hydrogen dilution of $R_{\text{H}} = 80$.

by the highly doped p^+-μc-Si:H layer occurs. However, Fig. 5.7 also illustrates that a good surface passivation quality can be achieved as well with a p-a-Si:H layer *if* it is grown with a high hydrogen dilution. Unfortunately, there was only one wafer with the same specifications as the other wafers in Fig. 5.7 left when I performed this experiment. Thus, for the p-a-Si:H layer grown with $R_H = 80$ there is only one data point in at an i-a-Si:H layer thickness of approximately 7.7 nm.

The effective minority carrier lifetime for reference wafers covered with i-a-Si:H layers of 30 nm thickness on each side is $\tau_{eff} \approx 1.0$ ms. Assuming negligible bulk recombination, I derive a surface recombination velocity S = 13 cm/s using the model of Sproul [79]. For the asymmetric structures depicted in the inset of Fig. 5.6, I find that the effective lifetimes increases from 100 μs (for no i-a-Si:H interlayer) up to 600 μs (i-a-Si:H layer thickness $d_i \approx 7.5$ nm). Accepting S = 13 cm/s for the side passivated with 30 nm i-a-Si:H, I derive values between S = 180 cm/s and S = 30 cm/s for the side passivated with the i-a-Si:H/p-μc-Si:H double layer.

From Figs. 5.6 and 5.7 I conclude that the surface passivation quality of i/p-layer stacks mainly depends on the hydrogen dilution that is used during the p-layer growth. High hydrogen dilutions yield good surface passivation qualities no matter whether the p-layers layers are amorphous (plasma frequency 13,56 MHz during growth) or micro-crystalline (plasma frequency 80 MHz during growth). This finding is remarkable due to the fact that the micro-crystalline layers have a much higher doping level and therefore create a much stronger BSF than their amorphous counterparts. For the solar cell back contacts in chapter 6, I therefore compare both i-a-Si:H/p^+-μc-Si:H and i-a-Si:H/p-a-Si:H surface passivation stacks. Note that, to achieve a low-Ohmic contact to the following ZnO:Al layer of the back contact, I additionally deposit a p^+-μc-Si:H layer on top of the pure amorphous i/p-system. The whole back contacts therefore use either a double layer stack (i-a-Si:H/p^+-μc-Si:H) or a triple layer stack (i-a-Si:H/p-a-Si:H/p^+-μc-Si:H).

From the present results, we see that increasing the i-a-Si:H interlayer thickness decreases the surface recombination velocity. Whether or not the simultaneous increase of the contact resistance compensates the expected efficiency gain is investigated in chapter 6.

5.5 Estimated open circuit voltages from lifetime measurements

As Eq. (2.7) describes, the open circuit voltage V_{oc} of a solar cell depends on the base and emitter doping, the temperature and the effective minority carrier lifetime τ_{eff}. It is therefore possible to estimate a virtual solar cell open circuit voltage V_{oc} from the measured effective lifetime of bare wafers. However, the virtual device is then passivated on both sides as the lifetime sample - a fact that does not hold for the solar cells. Real solar cells either have diffused emitters (chapter 6), oxidized back sides (chapter 7) or n-a-Si:H on the front and p-a-Si:H on the back side (chapter 8). Such cells are either not symmetric or use an a-Si:H surface passivation on one side only. It is then hard to declare which side of the device limits V_{oc}. The effective lifetime of a-Si:H coated wafers is injection dependent. If a-Si:H is used on one surface of a device, the injection density on *this* surface has to be estimated to enable a comparison of the cell's measured V_{oc} with the estimated V_{oc} from lifetime measurements. Such comparisons lead to a rather uncertain results.

Solar cells with a-Si:H on both sides are asymmetrical and use p-a-Si:H on one side and n-a-Si:H on the other side. To estimate their V_{oc} from the measured effective lifetime of unsymmetrical p-a-Si:H/p-c-Si/n-a-Si:H samples that have a built in electric field is rather difficult due to depletion region modulation [89].

However, to estimate a *boundary* on the solar cell's open circuit voltage imposed by the a-Si:H contacts, I calculate the open circuit voltage of symmetrically passivated c-Si lifetime samples. Figure 5.8 draws V_{oc} vs. τ_{eff} for wafers with a resistivity of 1 Ωcm ($N_A = 1.5 \times 10^{16}$ cm^{-3}, $D_n = 27$ cm^2/s and $d_{Si} = 250$ μm). As an estimation for the wafer bulk lifetime τ_b, I use $\tau_b = 1$ ms and $\tau_b = 10$ ms. The graph shows that high open circuit voltages $V_{oc} > 680$ mV are already in reach if the effective carrier lifetime τ_{eff} exceeds $\tau_{eff} > 200$ μs.

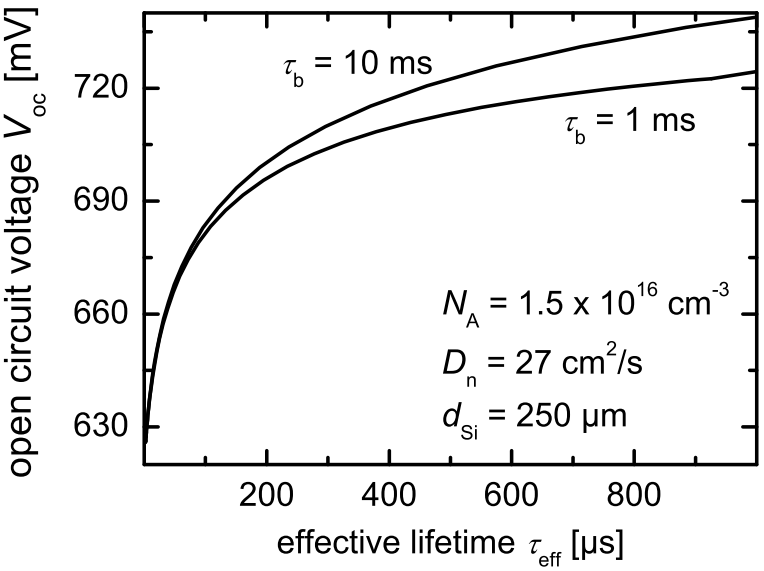

Fig. 5.8: Open circuit voltage versus effective carrier lifetime of a 1 Ωcm wafer for two distinct bulk lifetimes τ_b.

Chapter 6

Heterojunction back contacts

This chapter investigates heterojunction back contacts. After a literature review of p-type c-Si solar cell back contacts, the chapter summarizes how to meet the requirements for a high quality c-Si back contact with a-Si:H and describes the solar cell preparation sequence. The then following section presents results of devices with a-Si:H back contacts concerning their photovoltaic output parameters. The last parts of this chapter perform an extended fill factor analysis and an extended back side recombination velocity analysis of such solar cells.

6.1 Literature survey: Back contacts for p-type c-Si solar cells

At present, the back contact for p-type crystalline silicon solar cells is an important research issue. So far, the challenge to find an adequate alternative to the full area Al metallization that limits the efficiency of industrially fabricated devices due to its high back side recombination velocity is not solved. Besides, another disadvantage of the Al back contact metallization is that subsequent to the Al-paste application a high temperature contact firing step is necessary to form a low-Ohmic contact. This contact formation procedure is performed above the eutectic point of Al and Si (temperature $T = 577°\mathrm{C}$) and thus leads to a diffusion of Al into the c-Si to a depth of several microns. A bowing of the solar cell due to the different thermal expansion coefficients of the two materials is the consequence, leading to a high breakage rate during the subsequent module manufacturing. This problem gains

in importance nowadays because the wafer industry steadily decreases the wafer thickness down to thicknesses between 100 μm and 200 μm to save expensive c-Si material. Thus, alternative back contact concepts for silicon solar cells delivering a lower wafer bowing and a better electrical quality are highly desirable.

A feasible way to omit the wafer bowing caused by a *full area* Al contact and to enhance the cell's output power is via a back surface passivation layer combined with thermally activated or laser fired *local* Al contacts. Figures 6.1a,b show two distinct approaches. Fig. 6.1a depicts the approach of Schaper et al. and Plagwitz

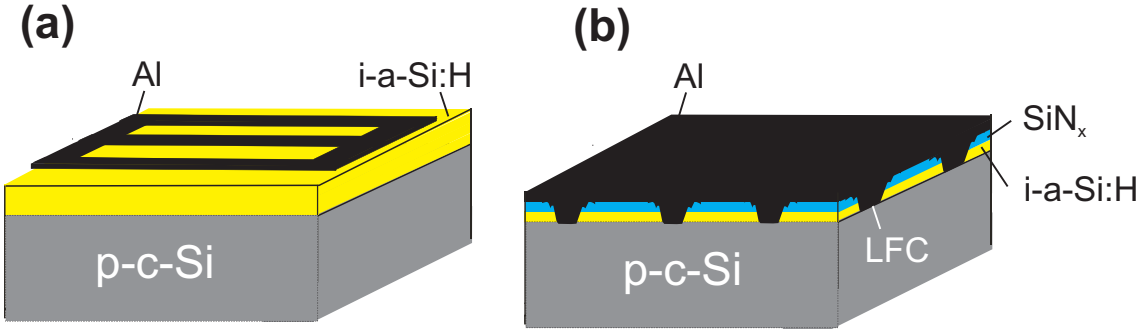

Fig. 6.1: Two approaches for an alternative c-Si solar cell back contact. (a) Aluminium grid evaporated on an i-a-Si:H coated wafer. The local contact to the c-Si base forms by an annealing step. The Al thereby sinters through the isolating passivation film. (b) Laser Fired Contact (LFC). An isolating passivation film such as SiO_2, SiN_x or a combination of a-Si:H together with SiO_2/SiN_x covers the wafer. A laser fires the Al locally into the c-Si base forming an Ohmic contact.

et al. [90, 91]. They used intrinsic amorphous silicon as a passivation layer and a local aluminum contact grid (denoted as Contact to Amorphous Silicon by Means of Annealing COSIMA). Subsequently to the Al-grid evaporation onto the i-a-Si:H, the Ohmic contact to the c-Si base forms by an annealing step at about 200 °C. The aluminum then penetrates through the i-a-Si:H to the c-Si base. Solar cells with COSIMA back contacts reach efficiencies up to $\eta = 20.1$ %. Note that this concept is similar to the Al point contact scheme presented in section 6.2. Maier used this Al point contact scheme together with a *sputtered* intrinsic a-Si:H film to passivate the wafer surface [92]. He fabricated solar cells with open circuit voltages up to $V_{oc} = 661$ mV and efficiencies up to $\eta = 18.6$ %.

Figure 6.1b shows another way to form local back contacts through an insulating passivation layer: A Laser Fired Contact (LFC). Aluminum is evaporated on top of a wafer with insulating passivation layer and then locally laser fired through into the c-Si base. Schneiderlöchner et al. used a thermally grown SiO_2 layer to passivate the wafer [93]. The disadvantage in this case is that the SiO_2 film has to be grown at temperatures above 900 °C making the process unsuitable for multi-crystalline material. Besides, the oxide that simultaneaously grows during the high temperature step on the cell's front surface has to be remove because an oxide layer on the front side does not form an antireflection coating after module encapsulation. However, Schneiderlöchner et al. achieved very high solar cell efficiencies $\eta = 21.2$ % with $V_{oc} = 679$ mV on a cell area of 4 cm^2 with a SiO_2 back surface passivation and a LFC. Schneiderlöchner et al. also used a more industrially relevant low temperature SiN_x back side passivation together with LFC. It is then possible to apply this back contact technique to solar cells with completed front electrodes. However, the device efficiency drops to $\eta = 19.5$ % with $V_{oc} = 665$ mV on a cell area of 4 cm^2 due to the fact that SiN_x has built-in fixed negative charges that make it less suitable than SiO_2 for solar cell side passivation.

Brendle et al. used another approach using laser fired contacts [69,70]. They used a low temperature intrinsic a-Si:H surface passivation in combination with a dielectric SiN_x layer and the local LFC. The i-a-Si:H passivates the c-Si surface and the SiN_x layer enhances the back side reflection. Brendle et al. achieve an efficiency of $\eta = 20.5$ % with $V_{oc} = 670$ mV on a cell area of 1 cm^2. The disadvantage of all described techniques is the local metal contact that still limits the open circuit voltage of the device by a high recombination velocity.

To my knowledge, research concerning a full area passivating heterojunction back contact has been carried out only on solar cells that use heterojunction emitters. Such devices are described in chapter 8. This work equips pn-*homojunction* emitter solar cells with full area *heterojunction* back contacts. The advantages of such solar cells are:

- The n-type emitter by phosphorous in-diffusion is standard in the solar cell industry; its particular advantage for multi-crystalline solar cells (today the most prominent solar cell type in the market) lies in gettering of impurities during the phosphorous diffusion.

- The back side of the cell is completely passivated and no local metal back contact increases the back side recombination velocity.
- The back contact needs no laser firing or thermal activation.
- There is no structuring of the rear metallization necessary. Hence, the back contact can be fabricated in a full in-line process.

To investigate their performance in solar cells concerning V_{oc} and η, the back contacts are applied to wafers equipped with a diffused homojunction emitter that has shown its capability to reach high efficiencies in the *ipe* standard process. In this process, the emitter together with a high efficiency PERC-type Aluminum point back contact [94], reliably yields $V_{oc} \geq 660$ mV and $\eta \geq 20.5$ %.

6.2 Back contact structure

Figures 2.6a-c show sketches of three different back contacts that are applied to solar cells in this thesis. The requirements for a high-efficiency c-Si back contact are:

- Low recombination velocity for minority carriers to achieve a high open circuit voltage.
- Back surface field (BSF) to repel minority carriers from the back surface and thereby further reduce the surface recombination velocity.
- High optical reflectance to reach a high short circuit current.
- Low resistance for majority carriers to achieve a high fill factor.

All these requirements are met by the a-Si:H/c-Si heterojunction back contacts:

- The intrinsic a-Si:H layer delivers a low surface recombination.
- A p-type doped a-Si:H or μc-Si:H layer creates a BSF.
- The ZnO:Al layer acts as a dielectric mirror and avoids a metallic contamination of the a-Si:H.
- Optimization of the i-a-Si:H layer thickness and of the p-a-Si:H as well as p-μc-Si:H deposition conditions lead to a low series resistance.

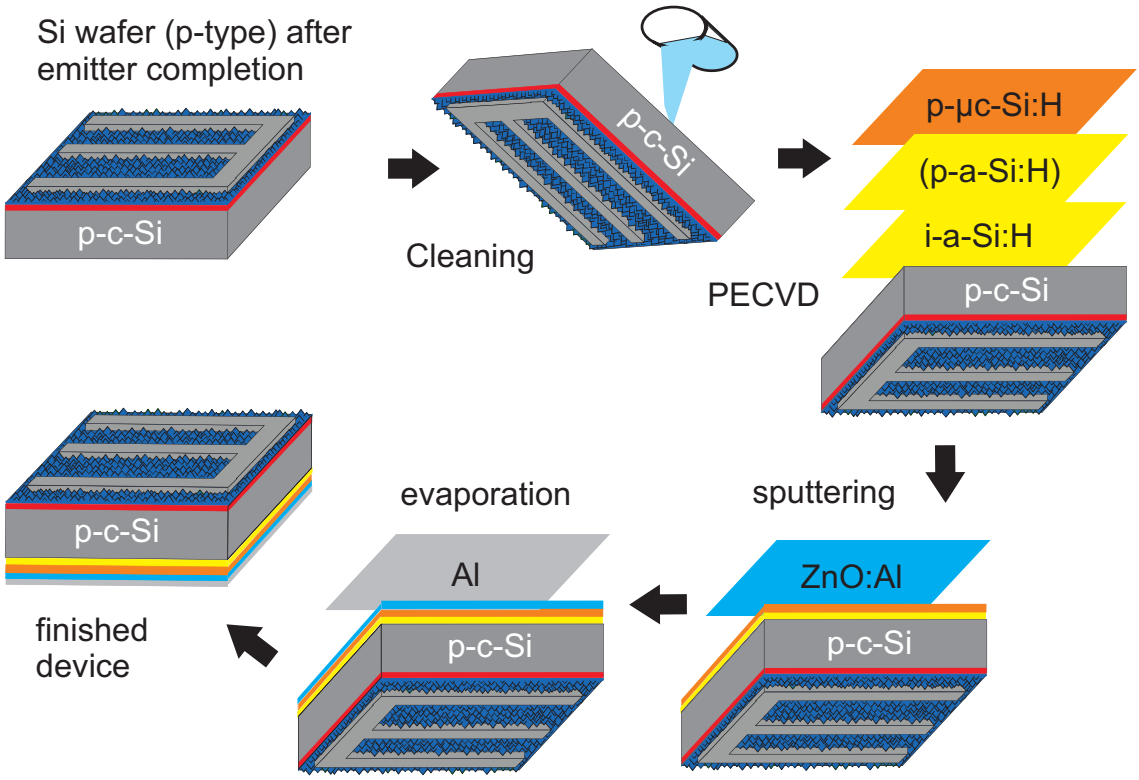

Fig. 6.2**:** Sketch of the the back contact preparation sequence for the solar cells equipped with diffused emitters. The back contact consists of intrinsic and boron doped μc-Si:H together with a transparent aluminum doped n-type ZnO:Al layer (double layer back contact). For the triple layer scheme, a boron doped a-Si:H buffer layer follows in between the i-a-Si:H and the p-μc-Si:H. The Al rear contact metal is evaporated onto the ZnO:Al to finish the device. For the alternative Al point contact scheme (confer Fig. 6.9) Al is evaporated additionally through a circularly perforated shadow mask *before* the ZnO:Al is sputtered.

Figure 6.2 shows a sketch of the back contact preparation sequence. The front side of the cells is completed first. The devices of this thesis use a shallow phosphorous doped, diffused emitter (sheet resistance $R_{\mathrm{sh}} = 100\ \Omega/\mathrm{sq}$) and a thermal oxide front passivation. The metal grid is structured photolithographically. The back side is masked with a thermal oxide during the whole front side processing to avoid contamination. The oxide is then removed by a single sided HF dip and the samples are subsequently mounted into a PECVD cluster system to fabricate the

back contact. The solar cell back contacts use either a single, double or a triple a-Si:H layer stack.

The single layer back contact, Fig. 2.6a and in the following denoted as 'single', is fabricated with the p^+-μc-Si:H layer that has shown the highest doping as well as the best surface passivation of all p-layers in the investigations described in the previous chapters of this thesis. It is deposited with a hydrogen dilution of R_H = 100 ($[H_2]$ = 200 sccm, $[SiH_4 + B_2H_5]$ = 2 sccm) at a chamber pressure of p = 0.52 mbar using a plasma frequency of ν_p = 80 MHz and a glow discharge power of P_I = 80 mW cm^{-2}, and has a thickness of approximately 30 nm. Besides its relevance to create a BSF, the $p^+\mu$c-Si:H also forms a low-Ohmic pn-tunneling contact to the transparent n-type ZnO:Al that follows in the back contact structure.

The double layer back contact, Fig. 2.6b and in the following denoted as 'double', is fabricated as follows: The standard i-a-Si:H surface passivation layer of this thesis is deposited onto the wafer with a silane flow of $[SiH_4]$ = 10 sccm, a chamber pressure of 0.52 mbar, a plasma frequency of ν_p = 13.56 MHz, and a glow discharge power of 8.8 mW/cm^2. Subsequently, the same p^+-μc-Si:H layer as used for the single layer back contact follows. The structure and the deposition conditions of the layers of the 'double' back contact are the same as for the lifetime samples in Fig. 5.7, chapter 5.

The triple layer back contact, Fig. 2.6c and in the following denoted as 'triple', uses the same i-a-Si:H and p^+-μc-Si:H layers as the double layer scheme but inserts a p-a-Si:H buffer layer in between (i-a-Si:H/p-a-Si:H/p^+-μc-Si:H structure). The 30 nm thick p-a-Si:H layer is deposited with a hydrogen dilution of R_H = 80 ($[H_2]$ = 160 sccm, $[SiH_4 + B_2H_5]$ = 2.5 sccm) at a chamber pressure of p = 0.52 mbar using a plasma frequency of ν_p = 13.56 MHz and a glow discharge power of P_I = 80 mW cm^{-2}. Due to the fact that not enough cells to create relevant statistics have been fabricated, it is so far uncertain whether there is a benefit caused by the p-a-Si:H buffer layer or not.

On top of the hydrogenated Si layer system a 100 nm thick magnetron sputtered ZnO:Al layer follows. The layer is deposited at a chamber pressure of p = 1.3 mbar using a plasma frequency of ν_p = 13.56 MHz and a glow discharge power of P_I = 1 W cm^{-2}. The ZnO:Al acts as a dielectric mirror, enhances the back side reflectance and keeps metallic impurities from the c-Si surface. The back contact is finished by evaporating Al onto the ZnO:Al layer. For the alternative point contact

scheme (confer Fig. 6.9), Al is evaporated additionally onto the a-Si:H through a circularly perforated shadow mask *before* the ZnO:Al sputtering.

Figure 6.3 shows the band diagram of a homojunction-emitter solar cell equipped with a heterojunction back contact. The figure illustrates that there is

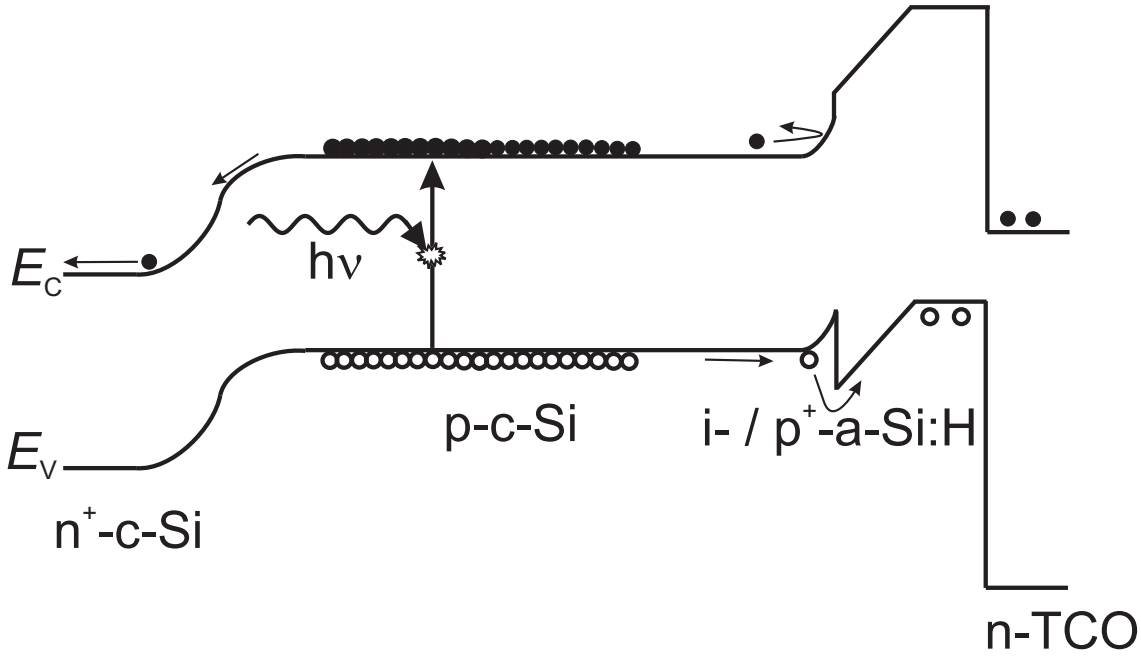

Fig. 6.3: Band diagram of a silicon solar cell with diffused pn-junction and heterojunction a-Si:H/c-Si/TCO back contact. The band offset in the conduction band and the back surface field at the c-Si/a-Si:H interface reduces the minority carrier recombination. The band offset in the valence band and the p$^+$-a-Si:H/n-ZnO:Al junction increase the series resistance.

a second pn-junction (p$^+$-μc-Si:H/n-ZnO:Al) at the rear interface. To achieve an Ohmic back contact, a steep band bending at this junction is necessary allowing for the tunneling of charge carriers.

6.3 Series resistance

In summary, solar cells with double/triple layer a-Si:H back contact include three obstacles that hamper the majority carrier transport across the contact and increase

the cell's series resistance R_s:

- The band offset in the valence band between c-Si and a-Si:H that limits the transport of holes across the c-Si/a-Si:H heterojunction.
- The p-a-Si:H/n-TCO interface that has to exhibit low-Ohmic tunneling instead of a rectifying pn-diode behavior.
- The i-a-Si:H surface passivation layer that has a high bulk resistance.

An increased series resistance R_s lowers the output power of the solar cell. The output power linearly decreases with decreasing fill factor as Eq. (3.1) in section 3.1.1 shows. Following the the phenomenological relation [95]

$$FF = \frac{v_{OC} - \ln(v_{OC} + 0.72)}{v_{OC} + 1} \left(1 - \frac{R_s J_{sc}}{V_{oc}}\right), \tag{6.1}$$

the fill factor FF itself decreases linearly with increasing series resistance R_s. Equation (6.1) uses $v_{OC} = qV_{oc}/n_{id}kT$. The following three sections estimate the influence of the three carrier transport barriers on the cell's series resistance R_s.

6.3.1 c-Si/a-Si:H heterojunction

Table 6.1 lists literature references of the band offset ΔE_V at a-Si:H/c-Si heterojunctions. The band offset in the valence band ranges around a value of $\Delta E_V \approx 0.5$ eV according to these literature references. The following estimates the influence of such a band offset on the series resistance of a solar cell. The transport of carriers across an energetic barrier follows

$$J = A^* T^2 \exp\left(\frac{-\Delta E_V}{kT}\right)\left(\exp\left(\frac{qV}{kT}\right) - 1\right), \tag{6.2}$$

with the Richardson-constant A^*. For a voltage $V = 0$, the conductance G_B across the barrier is

$$G_B(V = 0) = \frac{dJ}{dV} = \frac{A^* qT}{k} \exp\left(\frac{-\Delta E_V}{kT}\right). \tag{6.3}$$

With $\Delta E_V = 0.5$ eV, $T = 300$ K and $A^* = 100$ A/cm^{2}K^2 [102], I calculate a barrier conductance $G_B = 1.6$ S/cm^2 that corresponds to a barrier resistance $R_B = 0.6$

Tab. 6.1: References of the valence band offset in a-Si:H/c-Si heterojunctions.

Research group	Measurement technique	ΔE_V [eV]
Essick et al. [96]	Capacitance vs. temperature	0.58 ± 0.02
Sebastiani et al. [97]	Low-energy photoelectric yield spectroscopy	0.44 ± 0.02
Van de Walle et al. [98]	Theoretical investigation	0.2
Schäfer et al. [99]	Photoemission intensity	0.3
Song et al. [100]	Capacitance vs. voltage	0.18
Jensen et al. [23]	Electronic transport	0.51 ± 0.04
Einsele et al. [101]	Conductivity vs. temperature	0.6

Ωcm^2. This result shows that the resistance contribution R_B of the valence band offset is critical and has the same order of magnitude as a typical series resistance of a whole solar cell. The μc-Si:H bandgap is smaller than the one of amorphous material [100]. And the barrier resistance decreases exponentially with decreasing band offset. Hence, as described in section 5.3, a μc-Si:H/c-Si junction yields a considerably lower barrier resistance than an a-Si:H/c-Si junction but unfortunately an i-μc-Si:H layer does not passivate the c-Si surface.

6.3.2 p-a-Si:H/n-TCO heterojunction

Usually, pn-junctions such as the p-a-Si:H/n-ZnO:Al interface exhibit rectifying diode characteristics. To create the desired low Ohmic behavior, a junction that allows the tunneling of charge carriers is necessary. A tunneling pn-junction forms if the p-type and the n-type semiconductor are highly doped. The band bending is then very steep and transport takes place by tunneling of charge carrier from the conduction band of the n-layer (ZnO:Al) into the valence band of the p-layer (a-Si:H or μc-Si:H) leading to Ohmic I/V-characteristics. In such a case the a-Si:H/TCO interface forms a tunneling recombination junction according to the literature [103].

The n-type ZnO:Al sputtering target is supplied very highly Al doped by the manufacturer. Sheet resistance R_{sh} measurements of 1 μm thick layers yield very low values of $R_{sh} = 8\ \Omega_{sq}$. For the p-type layer, as section 4.3 shows, depositions in

the microcrystalline regime using high hydrogen dilutions and a plasma excitation frequency of $\nu_p = 80$ MHz deliver highly doped material. Figure 4.6 in this section shows a drastic increase in conductance i.e. a drastic increase in doping level for p-type layers that are grown with a hydrogen dilution of $R_H \geq 40$.

Figure 6.4 shows the functional dependence of the pn-diode zero-bias resistance R on the hydrogen dilution ratio R_H, the inset shows the test structure. Note that the structure is the same as for the 'single' back contact. A 40 nm thick layer of boron doped a-Si:H is directly deposited onto the surface of highly doped ($\rho = 10 - 20$ mΩcm) c-Si wafers. The hydrogen dilution ratio during depositio R_H = [H_2] / [B_2H_6 + SiH_4] is varied, whereas the chamber pressure of 0.52 mbar, the plasma frequency of $\nu_p = 80$ MHz, the Diboran/Silane gas mixture of 2 % B_2H_6 in SiH_4, and the glow discharge power of 8.8 mW/cm^2 are the same for all depositions. After the p-layer fabrication, the test devices are finished by magnetron sputtering of a 100 nm ZnO:Al layer and by evaporation of Al contacts on both sides of the wafer. The Al contact on the back side of the wafer is a full area contact, whereas the Al contact on top of the ZnO:Al is evaporated through a shadow mask onto areas of 0.1 cm^2. Subsequently, the ZnO:Al between the contact pads is removed by a short etch in 1 % HCl solution. I observe a significant resistance decrease by more than two orders of magnitude when the hydrogen dilution exceeds a threshold at approximately $R_H = 40$ and ascribe this dramatic change to a transition from amorphous to microcrystalline growth due to the increasing hydrogen dilution. For dilution ratios $R_H > 40$, the resistance decreases further and reaches values as low as $R < 10^{-3}$ Ωcm^2. This value is by far low enough to avoid significant resistive losses in a solar cell. In contrast, for dilution ratios $R_H < 40$, the contact resistance is pronouncedly too high for usage in a solar cell. Hence, in all back contacts of this thesis a p-μc-Si:H layer deposited at $R_H = 100$ is applied underneath the ZnO:Al layer.

The measured series resistance is a superposition of the Al/c-Si junction resistance, the c-Si bulk resistance, the c-Si/p-μc-Si:H junction resistance and the p-μc-Si:H/n-ZnO:Al junction resistance. With the p-μc-Si:H layers deposited at $R_H > 40$, the total structure resistance is much lower than the a-Si:H/c-Si barrier resistance calculated in the last section. The calculation uses the bandgap of amorphous material. It is very likely, that the discrepancy in estimated a-Si:H/c-Si and measured μc-Si:H/c-Si series resistance is caused by a *smaller* bandgap of the

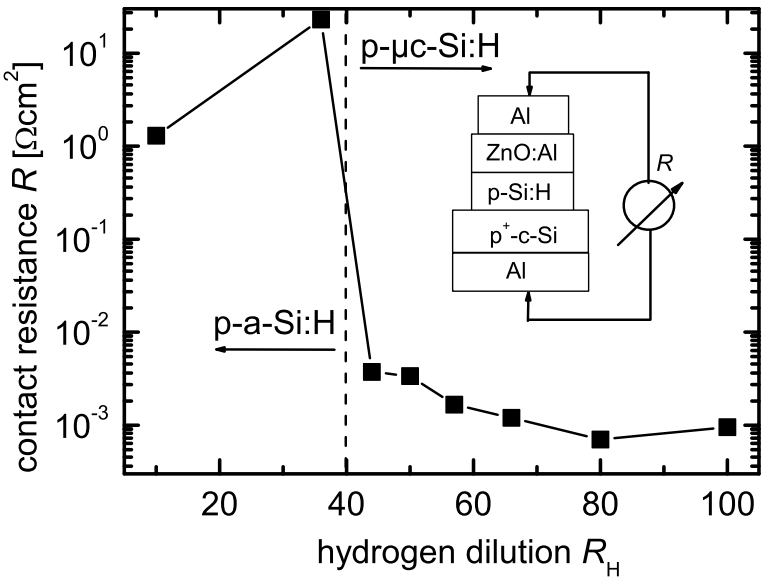

Fig. 6.4**:** Resistance of wafers equipped with a low-Ohmic full area Al contact on one side and a a-Si:H/ZnO:Al contact on the other side (confer inset). The samples estimate the p-a-Si:H/p-c-Si and the p-a-Si:H/n-ZnO:Al junction resistance. Samples that have p-a-Si:H layers deposited with low hydrogen dilutions have high resistances whereas the resistance is low for samples with p-layers deposited with high hydrogen dilutions. Lines are guides to the eyes.

p-μc-Si:H layer. Unfortunately, by the insertion of a *pure amorphous* intrinsic passivation layer on top of the c-Si surface and underneath the microcrystalline p-layer, the calculated *higher* a-Si:H/c-Si band offset arises again.

6.3.3 Intrinsic interlayer

The i-a-Si:H layer in a double/triple layer a-Si:H back contact increases the cell's series resistance by:

- Valence band offset. The valence band offset in a back contact with *amorphous* intrinsic interlayer is larger than in a back contact that uses solely a p-type *microcrystalline* layer.

- Bulk resistance of i-a-Si:H. Intrinsic a-Si:H has a very low charge carrier concentration as well as a low charge carrier mobility and therefore a high bulk resistance.

Figure 6.5 shows the series resistance of a double layer a-Si:H back contact versus the thickness of the intrinsic amorphous interlayer. The device structure is Al/p-c-Si/i-a-Si:H/p-μc-Si:H/n-ZnO:Al/Al. The p-μc-Si:H layer is deposited at $R_{\mathrm{H}} = 100$. The samples use i-a-Si:H either deposited with a hydrogen dilution of $R_H = 2.5$ or

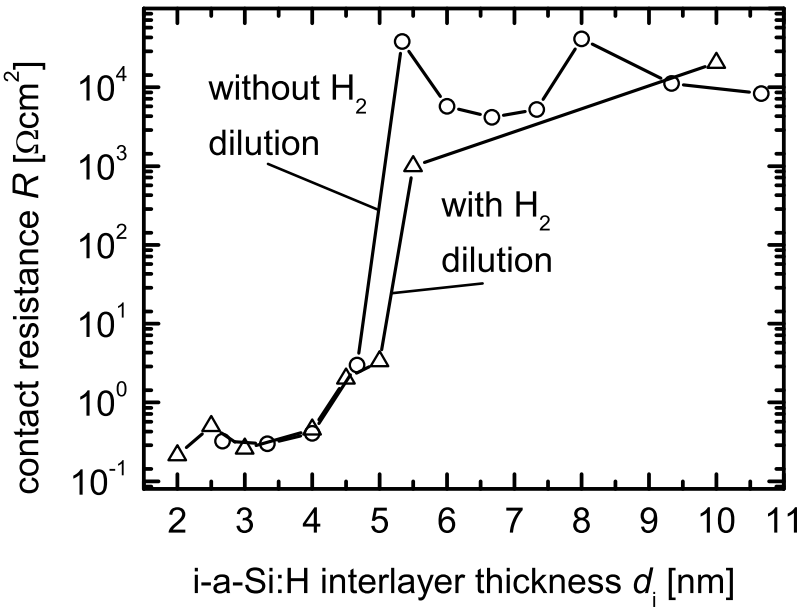

Fig. 6.5: Series resistance of heterojunction back contacts with intrinsic interlayer versus the i-a-Si:H thickness. The i-layers are fabricated with a hydrogen dilution $R_{\mathrm{H}} = 2.5$ and without. The hydrogen dilution leads to a lower deposition rate of about 6 nm/min compared to a deposition rate of about 7.8 nm/min without hydrogen. The series resistance of the back contact is already too high after surpassing a deposition time of 40 s for the layer with hydrogen dilution and 30 s for the layer without. These deposition times correspond to an intrinsic layer thickness of about 4 nm. Lines are guides to the eyes.

without additional hydrogen. The deposition rate for the hydrogen diluted i-a-Si:H

is about 6 nm/min. The undiluted i-layer has a higher deposition rate of about 7.8 nm/min. The graph shows that for the hydrogen diluted layer a deposition time of 40 s and for the undiluted layer a deposition time of already 30 s is enough to yield a critical series resistance. Such deposition times correspond to an i-a-Si:H layer thickness of about 4 nm. Besides its negative impact on the series resistance, the i-layer increases the diode ideality factor n_{id} of the solar cell, an observation that is further explained in subsection 6.5.1. As Eq. (6.1) shows, an increase of the diode ideality monotonically decreases the cell's fill factor. Hence, to achieve a low series resistance and an ideality factor n_{id} close to unity, omitting the i-a-Si:H film in a-Si:H back contacts is desired. However, as the lifetime samples in section 5.4 show, the surface passivation is then reduced. As a consequence, the open circuit voltage of solar cells without i-layer is lower. Hence, to achieve a maximum solar cell efficiency, the thickness of the i-a-Si:H layer has to be carefully optimized to achieve a high open circuit voltage V_{oc} while keeping the series resistance R_{s} low and the ideality factor n_{id} close to unity.

6.4 Series resistance and surface passivation model

To visualize the influence of the intrinsic layer on the surface passivation and the series resistance, the following develops a physical model that considers both effects. The model does not include spatial inhomogeneities, charge carrier hopping and tunneling. Therefore, the model represents a first, simple approach based on the charge carrier transport equations together with boundary conditions adapted for a-Si:H/c-Si heterojunctions. Despite these implications, the model visualizes the challenge in meeting both, a good surface passivation and a low series resistance together. Figure 6.6 shows the band diagram for the model. The model is divided into a calculation of the series resistance and the effective surface recombination velocity S_{eff} both depending on the built in potential Φ_0, the thickness of the i-a-Si:H layer d_{i}, the band offset and the charge carrier mobilities μ_{n}, μ_{p} in the a-Si:H layers.

Series resistance The series resistance R_{s} depends on the charge carrier transport of the majorities (holes). As Fig. 6.6 shows, the holes are accelerated by the BSF but have to overcome the barrier ΔE_{V} in the valence band to get into the i-a-Si:H

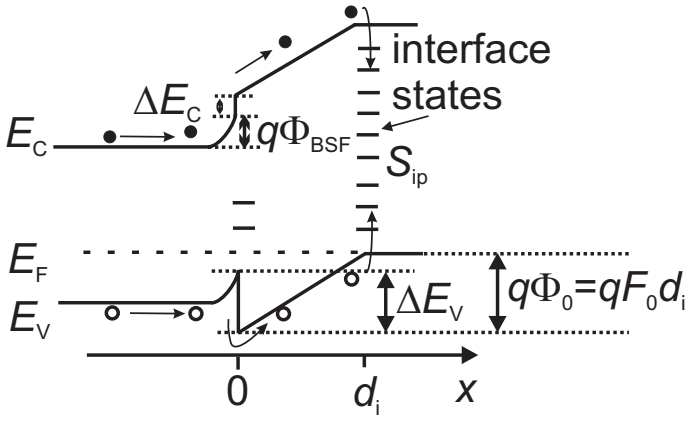

Fig. 6.6: Band diagram of a p-c-Si/i-a-Si:H/p$^+$a-Si:H heterostructure. The intrinsic layer thickness is d_i. The built in potential created by the p$^+$a-Si:H layer is Φ_0 inside the i-a-Si:H layer and Φ_{BSF} inside the base. At the i-a-Si:H/p$^+$a-Si:H interface, the surface recombination velocity is S_{ip} leading to an effective surface recombination velocity S_{eff} at the p-c-Si/i-a-Si:H interface.

layer where their mobility μ_p is lower than in the c-Si. In the i-a-Si:H layer, an electric field is present that enhances the hole transport towards the back contact. For a small thickness range, one can neglect generation as well as recombination resulting in $dj_p/dx = 0$ from the simplified continuity equation. Thus, the hole current densityj_p

$$j_p = -qD_p\frac{\mathrm{dp}}{\mathrm{d}x} + qF\mu_p p \tag{6.4}$$

with μ_p as the hole mobility in the a-Si:H, is constant. The electric field $F = F_0 + \Delta F$ consists of a built in electric field $F_0 = \Phi_0/d_i$, and an external electric field $\Delta F = V/d_i$ with V as the voltage drop across the contact. With the Ansatz $p(x) = A\exp(Bx)$, where A and B are constants, we find the general solution of Eq. (6.4) as

$$p(x) = \frac{j_p}{qF\mu_p} + \left(p(0) - \frac{j_p}{qF\mu_p}\right)\exp\left(\frac{Fx}{V_{th}}\right). \tag{6.5}$$

With the approximation

$$p(d_i) = p(0)\exp\left(\frac{\Phi_0}{V_{th}}\right), \tag{6.6}$$

where $V_{\mathrm{th}} = kT/q$ denotes the thermal voltage, the hole current j_{p} follows as

$$j_{\mathrm{p}} = q\frac{\Phi_0 + V}{d_{\mathrm{i}}}\mu_{\mathrm{p}}p(0)\left[1 - \exp\left(\frac{-V}{V_{\mathrm{th}}}\right)\right]. \tag{6.7}$$

The density of holes $p(0)$ at the c-Si/i-a-Si:H interface at the position $x = 0$ *inside* the i-a-Si:H layer follows from

$$p(0) = N_{\mathrm{A}}\exp\left(\frac{-(\Delta E_{\mathrm{V}} + q\Phi_{\mathrm{BSF}})}{kT}\right). \tag{6.8}$$

with N_{A} as the acceptor concentration in the c-Si, and Φ_{BSF} as the built in potential of the back surface field. Therewith, the contact resistance R calculates to

$$R = \left(\frac{\mathrm{d}j_{\mathrm{p}}}{\mathrm{d}V}\right)^{-1}|_{V=0} = \frac{V_{\mathrm{th}}d_{\mathrm{i}}}{q\mu_{\mathrm{p}}N_{\mathrm{A}}\Phi_0}\left[\exp\left(\frac{\Delta E_{\mathrm{V}} - q\Phi_{\mathrm{BSF}}}{kT}\right)\right]. \tag{6.9}$$

Effective surface recombination velocity S The surface recombination velocity depends on the excess density of minority carriers (electrons). For the model, I assume that the recombination velocity immediately at the c-Si/i-a-Si:H interface is negligible. Instead, I consider recombination at the i-a-Si:H/p-c-Si:H interface. As Fig. 6.6 shows, the electrons have to overcome the BSF, the barrier ΔE_{C} in the conduction band and the electric field in the i-a-Si:H to get to the i-a-Si:H/p$^+$a-Si:H interface where they recombine with the interface recombination velocity S_{ip}. With these assumptions, one can calculate the effective recombination velocity S_{eff} near the c-Si interface that limits the cell efficiency. For a small thickness range, one can neglect generation as well as recombination. Therefore the simplified continuity equation for electrons leads to a constant electron current density

$$\delta j_{\mathrm{n}} = -qD_{\mathrm{n}}\frac{\mathrm{d}}{\mathrm{d}x}\delta n - qF\mu_{\mathrm{n}}\delta n, \tag{6.10}$$

with μ_{n} as the electron mobility in the a-Si:H. In analogy to (6.5) the general solution of this equation is

$$\delta j_{\mathrm{n}} = qF\mu_{\mathrm{n}}\left[\frac{\delta n(x) + \delta n(0)\exp\left(\frac{-Fx}{V_{\mathrm{th}}}\right)}{\exp\left(\frac{-Fx}{V_{\mathrm{th}}}\right) - 1}\right], \tag{6.11}$$

with $\delta n(0)$ as the electron concentration *inside* the i-a-Si:H at the c-Si/i-a-Si:H junction corresponding to the position $x = 0$:

$$\delta n(0) = \delta n_{\mathrm{b}}\exp\left(\frac{-\Delta E_{\mathrm{C}} + q\Phi_{\mathrm{BSF}}}{kT}\right). \tag{6.12}$$

Here, δn_b is the excess electron concentration in the c-Si bulk. At the i-a-Si:H/p$^+$-a-Si:H junction (position $x = d_\mathrm{i}$), charge carriers recombine with an interface recombination velocity S_ip and the electron current holds

$$\delta j_\mathrm{n}(d_\mathrm{i}) = qS_\mathrm{ip}\delta n(d_\mathrm{i}). \tag{6.13}$$

Inserting Eq. (6.13) in (Eq. 6.11) at the position $x = d_\mathrm{i}$ yields

$$\delta j_\mathrm{n}(d_\mathrm{i}) = \delta n(0)\exp\left(\frac{-Fd_\mathrm{i}}{V_\mathrm{th}}\right)\left[\frac{qF\mu_\mathrm{n}}{F\mu_\mathrm{n} + S_\mathrm{ip}\left(1-\exp\left(\frac{-Fd_\mathrm{i}}{V_\mathrm{th}}\right)\right)}\right]. \tag{6.14}$$

At the position $x = 0$, the electron current holds

$$\delta j_\mathrm{n}(0) = qS_\mathrm{eff}\delta n_\mathrm{b} \tag{6.15}$$

with the effective recombination velocity S_eff near the c-Si/i-a-Si:H interface. Inserting Eq. (6.15) into (Eq. 6.14) allows to derive S_eff to

$$S_\mathrm{eff} = S_\mathrm{ip}\exp\left(\frac{-(q\Phi_0 + \Delta E_\mathrm{C} + q\Phi_\mathrm{BSF})}{kT}\right)\left[1 + \frac{S_\mathrm{ip}d_\mathrm{i}}{\Phi_0\mu_\mathrm{n}}\left(1-\exp\left(\frac{-q\Phi_0}{kT}\right)\right)\right]^{-1} \tag{6.16}$$

with $\Phi_0 = F_0 d_\mathrm{i}$ as the built in potential without externally applied voltage. Equation (6.16) shows, that the upper boundary $S_\mathrm{eff,MAX} = S_\mathrm{eff}(S_\mathrm{ip} \to \infty)$ of the effective recombination velocity is imposed by

$$S_\mathrm{eff,MAX} = \frac{\Phi_0\mu_\mathrm{n}}{d_\mathrm{i}}\exp\left(\frac{-(q\Phi_0 + \Delta E_\mathrm{C} + q\Phi_\mathrm{BSF})}{kT}\right)\left[1-\exp\left(\frac{-q\Phi_0}{kT}\right)\right]. \tag{6.17}$$

Thus, $S_\mathrm{eff,MAX}$ is mainly influenced by the *sum* of the built in potential and the valence band offset.

Figure 6.7 shows the effective surface recombination velocity S_eff and the contact resistance R versus the i-a-Si:H layer thickness. According to Refs. [104, 105], the electron and hole mobilities in a-Si:H are in the range of μ_n = 1 - 5 cm^2(Vs)$^{-1}$ and μ_p = 0.1 - 0.5 cm^2(Vs)$^{-1}$. For the calculation of Figs. 6.7 and 6.8, I use μ_n = 3 cm^2(Vs)$^{-1}$ and μ_p = 0.3 cm^2(Vs)$^{-1}$, a wafer doping of $N_\mathrm{A} = 1.5 \times 10^{16}$ cm^{-3}, an i-a-Si:H/p-a-Si:H interface recombination velocity of $S_\mathrm{ip} = 10^7$ cm/s and a temperature T = 300 K.

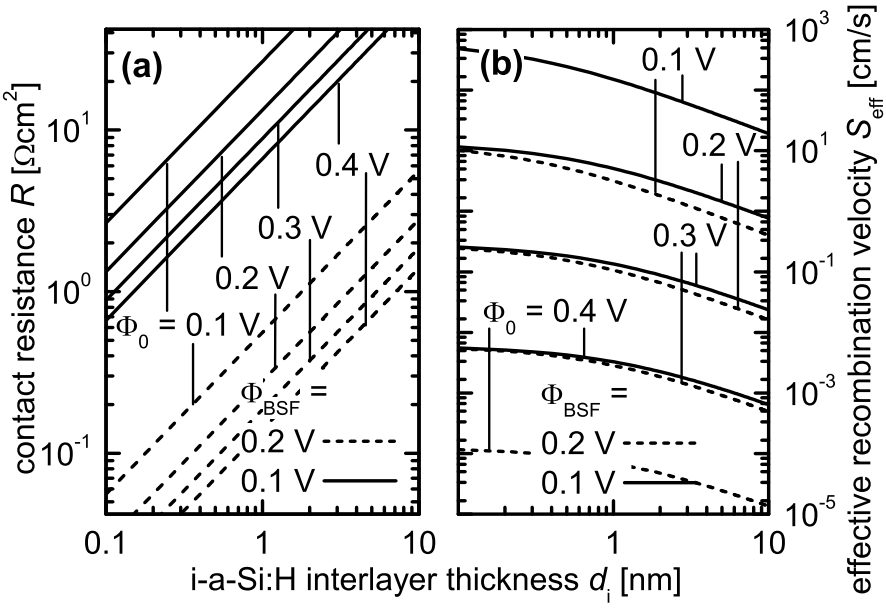

Fig. 6.7: a) Calculated zero bias contact resistance R and b) effective surface recombination velocity S_{eff} versus the intrinsic interlayer thickness d_{i}. For an i-a-Si:H layer thickness $d_{\text{i}} = 3$ nm, the series resistance is already critical for usage in solar cells.

Figure 6.7a visualizes that an i-a-Si:H layer thickness $d_{\text{i}} = 3$ nm as experimentally determined (see chapter 5) to be necessary for a good surface passivation, leads to a series resistance that is already slightly too high for usage in a solar cell. The resistance R_{s} is then larger than 0.2 Ωcm^2 even for a built in back surface field potential of $\Phi_{\text{BSF}} = 0.2$ eV inside the c-Si base and a potential $\Phi_0 = 0.4$ eV in the i-a-Si:H layer. For such a high Φ_{BSF} value and a base doping of $N_{\text{A}} = 1.5 \times 10^{16}$, the Fermi level already tangents the valence band edge at the c-Si/a-Si:H interface. With a lower back surface potential $\Phi_{\text{BSF}} = 0.1$ eV, the series resistance is always pronouncedly too high for usage in a solar cell, no matter how thick the i-a-Si:H layer and no matter how strong the potential in the i-a-Si:H.

Figure 6.7b shows, that the calculated effective surface recombination velocity $S_{\text{eff,MAX}}$ is lower than 1000 cm/s for nearly all assumed potentials and i-a-Si:H

layer thicknesses. The model assumes that the a-Si:H/c-Si interface recombination velocity is zero and that the i-a-Si:H layer is totally homogeneous. In reality, recombination takes place as well at the a-Si:H/c-Si interface and the first i-a-Si:H nanometers cover the c-Si surface spatially inhomogeneous. Hence, measured S values are higher than what the model predicts.

Figure 6.8 shows the resistance R (Fig. 6.8a) and the effective surface recombination velocity S_{eff} (Fig. 6.8b) for different potentials Φ_{BSF} and Φ_0. Figure

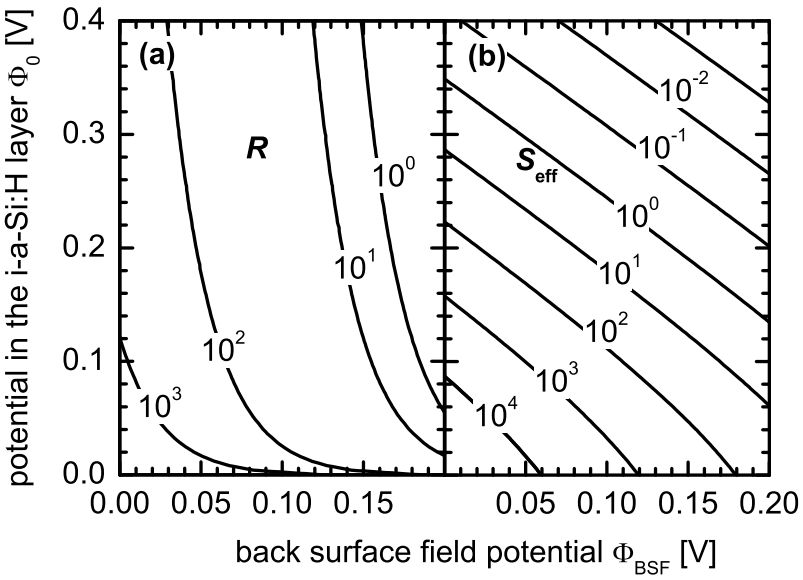

Fig. 6.8: a) Zero bias contact resistance R of Eq. (6.9) calculated with an intrinsic layer thickness of $d_{\text{i}} = 1$ nm and a valence band offset of $\Delta\ E_{\text{V}} = 0.45$ eV, plotted vs. the potentials Φ_{BSF} in the c-Si base and Φ_0 in the i-a-Si:H layer. The resistance depends *much stronger* on the c-Si back surface potential than on the potential in the i-a-Si:H. b) The effective surface recombination S_{eff} velocity from Eq. (6.16) calculated with $d_{\text{i}} = 1$ and a conduction band offset of $\Delta\ E_{\text{C}} = 0.05$ eV depends equally on both potentials.

6.8a visualizes that the contact resistance R depends much stronger on the built in back surface potential in the c-Si base than on the potential in the i-a-Si:H

layer. Besides, low enough series resistances to avoid significant resistive losses in heterojunction solar cells are only achievable for $\Phi_{BSF} > 0.15$ eV. Thus, the critical point that determines the series resistances in a heterojunction back contact of a p-type c-Si solar cell is the hole concentration at the c-Si/a-Si:H interface. The higher the hole concentration and the closer the fermi level to the valence band edge at this junction, the lower the series resistance. As Fig. 6.8b shows, S_{eff} depends equally on both potentials. The effective surface recombination velocity S_{eff} is basically controlled by the *sum* of the potentials in the c-Si base and the i-a-Si:H layer. The higher the sum of the potentials, the lower is S_{eff}.

6.5 Solar cell results and analysis

Figure 6.9a shows a sketch of a solar cell with full area a-Si:H/ZnO:Al back contact, Fig. 6.9b a sketch of a cell with the alternative aluminum dot back contact. The

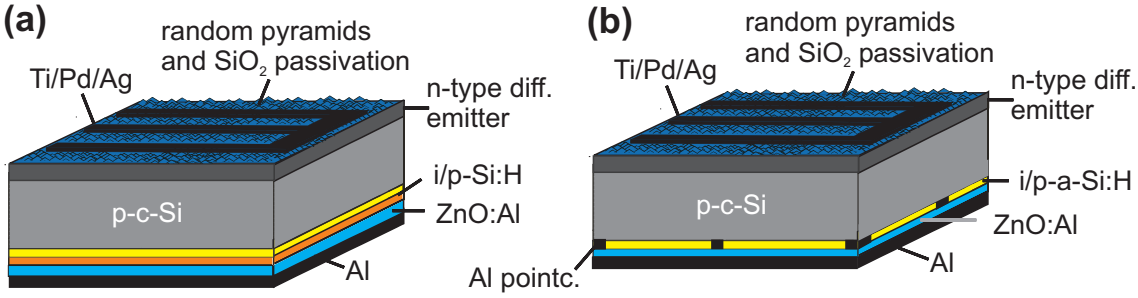

Fig. 6.9: Sketch of the full area a-Si:H/ZnO:Al back contact (a) and the a-Si:H/Al-point back contact (b). The a-Si:H layer system consists in both cases of an undoped a-Si:H layer and a second p-type doped layer. Contact (a) has a very highly p-type doped μc-Si:H layer on top of the i-a-Si:H layer. Therewith forms a low Ohmic contact to the ZnO:Al without additional Al-point contacts.

Al point contact scheme uses an a-Si:H layer system consisting of intrinsic and p-type a-Si:H. Before the ZnO:Al sputtering, the aluminum is evaporated onto the a-Si:H through a shadow mask with circular openings of a diameter 200 μm and a distance of 1 mm. Maier et al showed that the BSF of the p-type a-Si:H layer is not mandatory for the Al point back contact and it is also possible to fabricate high-efficiency devices with such a back contact by only using i-a-Si:H [92].

Figure 6.10 shows the current/voltage and the power/voltage characteristics of the best independently measured cell with full area triple layer a-Si:H back contact (cell area $A = 1$ cm^2). The device has an efficiency $\eta = 21$ %, confirmed by the Fraunhofer Institute for Solar Energy Systems (ISE), Freiburg. Table 6.2

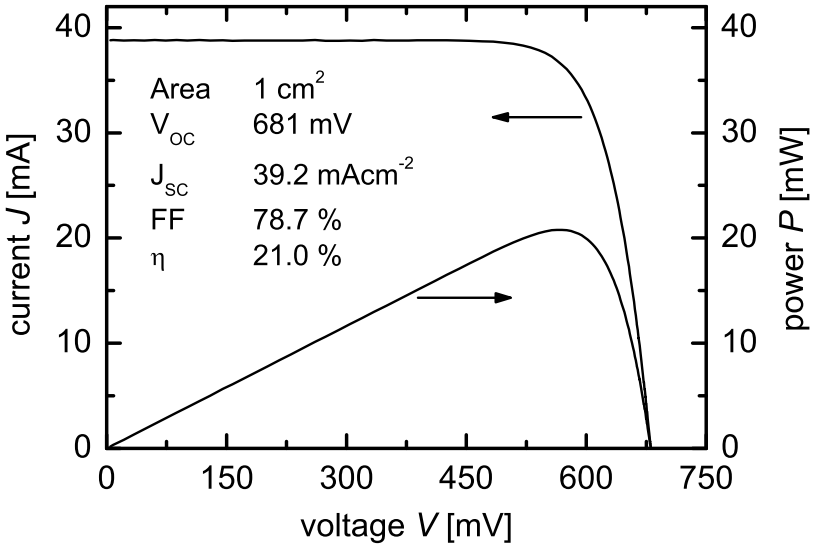

Fig. 6.10: Current/voltage and power/voltage curve of the best solar cell with full area a-Si:H/ZnO:Al back contact under standard test conditions as measured by Fraunhofer Institute (ISE) Freiburg.

summarizes the photovoltaic output parameters open circuit voltage $V_{\rm oc}$, short circuit current density $J_{\rm sc}$, fill factor FF, and power conversion efficiency η of the cell from Fig. 6.10 together with another solar cell with the same triple layer a-Si:H back contact (samples 'triple-a' and 'triple-b'). The table also shows our best cell with double layer a-Si:H back contact (sample 'double'). Note that the base doping $N_{\rm A}$ of this cell is higher (bulk resistivity $\rho_{\rm b} = 0.3$ Ωcm compared to $\rho_{\rm b} = 1$ Ωcm for the other devices). For comparison, the table also contains the data of one single layer p$^+$-μc-Si:H device (sample 'single'). It uses the same back contact as the double layer cell only *without* i-a-Si:H passivation interlayer. The best confirmed

solar cell with the Al-point contacts is also shown in the table (sample 'Al point'). Furthermore, to emphasize the performance of the a-Si:H back contacts, the table lists one device with full area Al back contact (sample 'Al').

Tab. 6.2: Photovoltaic output parameters open circuit voltage V_{OC}, short circuit current density J_{SC}, fill factor FF, and power conversion efficiency η under AM1.5G conditions of solar cells with different base resistivities ρ_b equipped with diffused emitters and a-Si:H or Al back contacts.

Back contact	ρ_b [Ωcm]	Area [cm^2]	V_{OC} [mV]	J_{SC} [mA/cm^2]	FF [%]	η [%]
triple-a*	1	4	679	38.8	77	20.2
triple-b*	1	1	681	39.2	78.7	21
double	0.3	2	665	39.7	81.0	21.4
single	1	1	641	38.5	80.1	19.7
Al point*	1	2	655	39.0	79.5	19.3
Al	1	4	620	36.4	77.5	17.5

*confirmed by Fraunhofer Institute (ISE), Freiburg

Concerning V_{oc}, 'double' and 'triple' clearly outperforms the 'single' back contact, emphasizing the important role of the intrinsic surface passivation layer to reach high efficiencies. The recombination velocity at the back side of the 'single' sample limits the open circuit voltage to $V_{oc} = 641$ mV. In terms of V_{oc}, the 'double' and 'triple' samples are superior to the point contact scheme, also due to the better back surface passivation. The local Al-points lead to a higher back surface recombination velocity. All heterojunction back contacts yield a higher open circuit voltage and therefore a higher efficiency than the full area Al back contact.

Concerning the fill factor FF, both single and double layer a-Si:H back contacts yield the highest values. The very high fill factor of 81 % of the double layer sample compared to the triple layer samples can be explained with the following argument: All back contacts are processed in different a-Si:H deposition runs. As it is very hard to reproduce an i-a-Si:H layer thickness d_i of around 2 to 3 nm, it may vary slightly between the samples. A slightly thinner i-a-Si:H layer of the 'double' compared to the 'triple' samples can cause a lower series resistance. The 'double' sample also has a lower base doping than the 'triples'. However, the influence of the

base doping on R_S of heterojunction back contacts is not yet evaluated. Section 6.5.1 performs an extended fill factor analysis on equally base doped cells with double and triple back contacts that use different i-a-Si:H layer thicknesses. The section shows that the double layer system is not superior to the triple layer system for the same base doping and the same i-a-Si:H layer thickness.

Figure 6.11 shows the comparison of the internal quantum efficiency IQE of the cell from Fig. 6.10 with the point contact cell. The IQE is measured with a bias illumination that corresponds to an intensity of 1 sun at AM 1.5 conditions. The lower surface recombination of the full area contact yields a higher IQE (curve a) in the wavelength regime 950 nm $\leq \lambda \leq$ 1050 nm if compared to the point contact cell (curve b). A plot of the inverse quantum efficiency IQE^{-1} versus the absorption

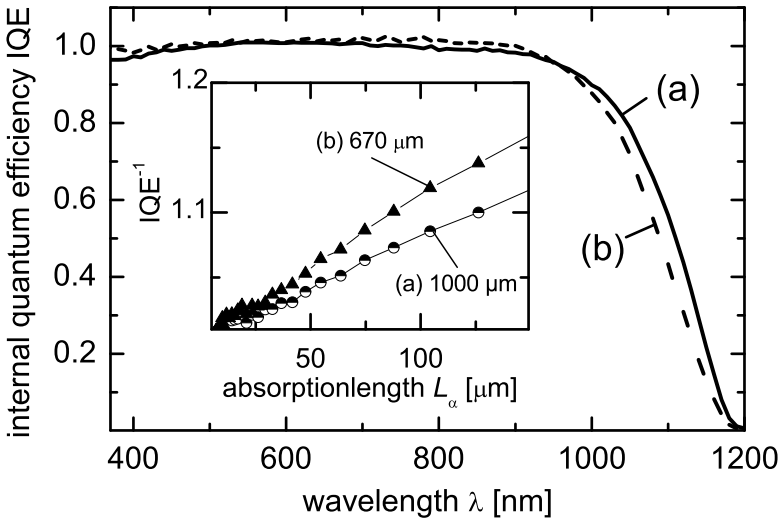

Fig. 6.11: Internal quantum efficiency of the cell triple-a (curve a) and the cell with Al point contacts (curve b) both from Tab. 6.2, measured by Fraunhofer Institute (ISE) Freiburg.

length as shown in the inset of Fig. 6.11 allows to determine the effective diffusion length from the slope of the measured data points [28]. This inset also depicts

the cell with point contacts (curve a) and the one with triple layer full area a-Si:H contact (curve b). For the triple layer contact cell, I find an effective diffusion length $L_{\mathrm{eff}} \approx 1000$ μm, a value that exceeds the cell thickness d by a factor of 4. From the ratio L_{eff}/d, I calculate the maximum possible value S_{MAX} for the back side recombination velocity according to [106]:

$$S_{\mathrm{MAX}} = \frac{D_{\mathrm{n}}/d_{\mathrm{Si}}}{L_{\mathrm{eff}}/d - 1}. \tag{6.18}$$

This equation is similar to Eq. (5.1) where S_{MAX} is calculated for symmetrically passivated samples. The symmetrical structure is considered in Eq. (5.1) by the factor 1/2. With a minority carrier diffusion coefficient of $D_{\mathrm{n}} = 27$ cm^2/s and $d_{\mathrm{Si}} = 250$ μm, I derive $S_{\mathrm{MAX}} \approx 360$ cm/s for the triple layer contact cell. For the point contact cell from Fig. 6.11 I find $L_{\mathrm{eff}} \approx 670$ μm and calculate $L_{\mathrm{eff}}/d \approx 2.7$ and $S_{\mathrm{MAX}} \approx 640$ cm/s. As a comparison, a back contact using a thermal oxide rear passivation and photolithographically opened local metal point contact delivers a surface recombination velocity $S_{\mathrm{back}} \approx 260$ cm/s [107].

6.5.1 Extended fill factor analysis

Figures 6.12a,b show the fill factor and the open circuit voltage as well as the FF x V_{oc} product of solar cells on 1 Ωcm boron doped base substrates equipped with full area double (Fig. 6.12a) and triple layer (Fig. 6.12b) a-Si:H back contacts plotted versus the intrinsic interlayer thickness. To specify the *real* intrinsic layer thickness in the back contact system is difficult and the values in the figure are approximations. To approximate the a-Si:H thickness on the wafers, I deposit thick test layers on glass substrates, measure the thickness and derive the deposition rate (comp. section 3.1.4). Using this deposition rate, I calculate the thickness of the a-Si:H layers on the wafers by linear extrapolation. Figure 6.12a shows that a $V_{\mathrm{oc}} = 640$ mV is already obtained without i-layer (single layer system, cell data also shown in Tab. 6.2). Insertion of the i-a-Si:H (double layer system) leads to an increase of V_{oc} with increasing layer thickness. A maximum $V_{\mathrm{oc}} = 687$ mV is achieved with an i-layer thickness of 4 nm. However, the fill factor decreases with increasing i-layer thickness, and, as Fig. 6.12a depicts, the fill factor drops drastically from 78.7 % to below 60 % between an i-a-Si:H layer thickness $d_{\mathrm{i}} = 3$ nm and $d_{\mathrm{i}} = 4$ nm.

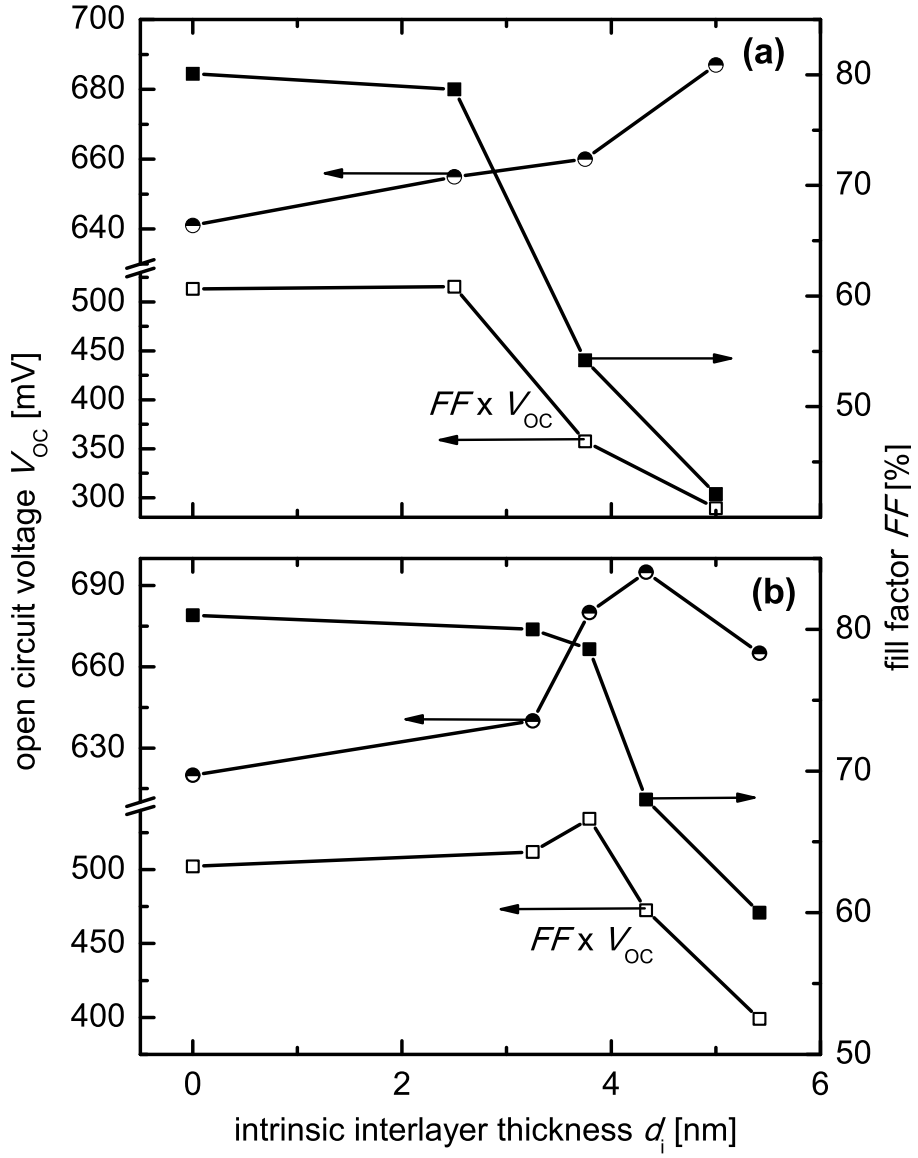

Fig. 6.12: Fill factor and open circuit voltage of solar cells with full area a-Si:H back contact versus the intrinsic interlayer thickness, (a) double layer system and (b) triple layer system. The fill factor decreases drastically due to an increased series resistance for an i-a-Si:H layer thickness $d_i \geq 2$ to 4 nm. The open circuit voltage behaves oppositely. Note that it is difficult to determine the *exact* i-a-Si:H layer thickness. The thickness d_i depends strongly on the deposition chamber conditions and the substrate holder conditions. Lines are guides to the eyes.

I use FF x V_{oc} as figure of merit instead of the efficiency because J_{sc} may differ between the cells due to slight differences in the optical properties (surface texture). The product FF x V_{oc} barely changes from $d_i = 0$ nm to $d_i = 2$ nm and then steeply drops. Thus, for a base resistivity 1 Ωcm one may conclude that there is no benefit from an i-a-Si:H layer underneath the $p^+ - \mu$c-Si:H layer (double layer system). However, as Tab. 6.2 shows, for a base resistivity of 0.33 Ωcm, the double layer system clearly outperforms the single layer system.

Figure 6.12b shows that for the triple layer system the increase of V_{oc} with increasing intrinsic layer thickness is more pronounced than in Fig. 6.12a whereas the decline of the fill factor at $d_i > 3$ nm is less dramatic as for the double layer system. For FF x V_{oc}, the triple layer system actually yields a maximum around $d_i = 3$ nm that combines a high $V_{oc} = 680$ mV with a high $FF = 78.7$ %. Figure 6.12 shows that, at least for the triple layer system (Fig. 6.12b), *there is a very small range for the i-a-Si:H layer thickness, where V_{oc} as well as FF are high.* As my experiments show, the range for a maximum cell efficiency is 2.5 nm $\leq d_i \leq$ 4 nm. The most challenging task when fabricating cells with double/triple layer a-Si:H back contacts is to *reliably* reproduce such a thin i-a-Si:H layer.

It is important to note, that for each intrinsic layer thickness depicted in Fig. 6.12 only one wafer has been prepared. Hence, I would not recommend to derive conclusions about the assets and drawbacks of the double or triple layer back contact system from the present results. However, Fig. 6.12 suggests that the i-layer only delivers a real benefit in the triple layer back contact. The difference between the two contact systems is the p-a-Si:H layer that is included in the triple layer system. The preparation of more solar cells with both back contacts using various base doping has to prove the role of this p-a-Si:H buffer layer.

The fill factor is generally the most unsatisfactory parameter for cells with double/triple layer a-Si:H back contacts. For all cells with very high open circuit voltages 679 mV$< V_{oc} <$ 683 mV, the fill factor is within an range 74 %$< FF <$ 78.6 %. Thus, I am interested whether these relatively low values result from a large series resistance R_s or from a non-ideal diode behavior expressed by an ideality factor $n_{id} > 1$. The relation Eq. (6.1) shows that the fill factor decreases monotonically with increasing R_s and n_{id}. There are well established analysis schemes that allow to derive R_s and n_{id} as long as these values do not depend on the voltage [108]. Unfortunately, in the case of double/triple layer a-Si:H back contact solar cells, n_{id} turns

out to be voltage dependent. In the following, I therefore use an analysis method to evaluate the fill factor losses [109]. This method bases on the $J_{sc}(\phi)/V_{oc}(\phi)$ method as outlined in Ref. [110]. Assuming a saturation current density $J_0(V_i)$ that depends on the internal voltage $V_i = V - JR_s$ I obtain

$$J = J_0(V - JR_s)\left[\exp\left(\frac{q(V - JR_s)}{kT}\right) - 1\right] - J_{sc} \tag{6.19}$$

where V denotes the voltage at the cell's terminals. Note that Eq. (6.19) differs from the conventional form of a $J(V)$ characteristics

$$J = J_0\left[\exp\left(\frac{q(V - JR_s)}{n_{id}kT}\right) - 1\right] - J_{sc} \tag{6.20}$$

that contains the ideality factor n_{id} and a *voltage independent* J_0. Neglecting the "1" in the square brackets and calculating the derivative $\mathrm{dln}(J - J_{sc})/\mathrm{d}V_i$ of Eqs. (6.19) and (6.20) leads to

$$\frac{1}{n_{id}} = 1 + \frac{kT}{q}\frac{\mathrm{d}}{\mathrm{d}V_i}\ln\left(J_0(V_i)\right). \tag{6.21}$$

Thus, Eq. (6.19) yields a voltage independent ideality factor only as long as $\mathrm{dln(J_0)/dV_i}$ is voltage independent.

According to Eq. (6.19), the short circuit current densities $J_{sc}(\phi)$ and the open circuit voltages $V_{oc}(\phi)$ at various illumination intensities ϕ are interrelated by

$$J_{sc}(\phi) = J_0(V_{oc}(\phi))\left[\exp\left(\frac{qV_{oc}(\phi)}{kT}\right) - 1\right]. \tag{6.22}$$

The series resistance R_s does not appear in Eq. (6.22). The analysis of $J_{sc}(\phi)/V_{oc}(\phi)$ curves is thus suitable to eliminate the influence of R_s. In this situation it furthermore holds $V_{oc} = V_i = V$ and one may derive $J_0(V)$ directly from experimental $J_{sc}/V_{oc}(\phi)$ data by using

$$J_0(V) = J_0(V_{oc}) = J_{sc}\left[\exp\left(\frac{qV_{oc}}{kT}\right) - 1\right]^{-1}. \tag{6.23}$$

Figure 6.13a depicts the $J_{sc}(\phi)$ versus $V_{oc}(\phi)$ characteristics of the triple-a cell from Tab. 6.2. As also shown in Fig. 6.13a, I obtain $J_0(V)$ with an obvious nonlinear dependence of $\ln(J_0)$ on V by using Eq. (6.23). The dependence of the saturation

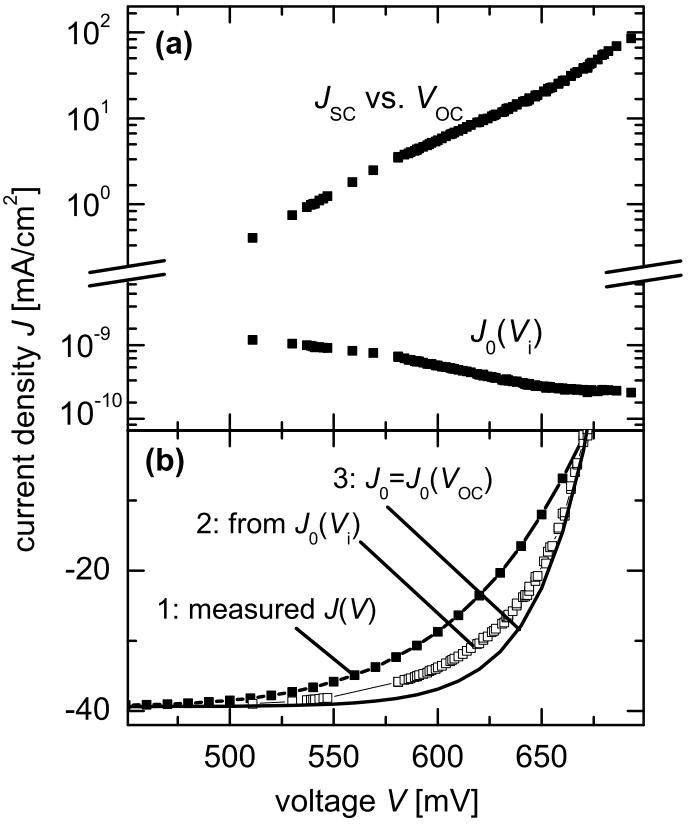

Fig. 6.13**:** (a) Short circuit current densities J_{SC} vs. open circuit voltages V_{OC} (upper curve) and the voltage dependant saturation current densities $J_0(V)$ obtained with the help of Eq. (6.23) (lower curve). (b) Comparison of current density vs voltage of the triple-a cell measured at simulated AM1.5 conditions together with two reconstructed curves 2 and 3. Curve 2 is obtained by shifting the $J_{SC}(V_{OC})$ curves from (a) by the short circuit current density J_{SC}(AM1.5). Curve 3 uses Eq. (6.22) assuming a constant J_0=$J_0(V_{OC})$. From the fill factors FF of the three curves I obtain the fill factor losses $\Delta FF_{n_{id}} = 2.5$ % and $\Delta FF_{RS} = 3$ % that are due to the non-ideal diode behavior and to resistive losses, respectively.

current density (J_0) on the Voltage V is explained by the injection dependence of the back surface recombination velocity S and, according to Eq. (2.13), J_0 depends on S. Figure 5.2 shows that S is high for low injection densities (respectively low voltages V) due to amphoteric defects and that S decreases with increasing injection density (respectively increasing voltage V).

I now construct a $J(V)$ characteristics by introducing the experimentally determined $J_0(V)$ into

$$J = J_0(V)\left[\exp\left(\frac{qV}{kT}\right) - 1\right] - J_{\mathrm{sc}}(\mathrm{AM1.5}). \tag{6.24}$$

As depicted in Fig. 6.13b, curve 2, this constructed $J(V)$ is just the $J_{\mathrm{sc}}(V_{\mathrm{oc}})$ curve shifted by the short circuit current density J_{sc}(AM1.5) at simulated AM1.5G illumination conditions. Thus, curve 2 is free of resistive effects and allows one to compare this curve with the real $J(V)$ characteristics (curve 1) of cell triple-a measured under simulated AM1.5 conditions. The measured fill factor FF_{M} is $FF_1 = 78.7$ % whereas that of the reconstructed curve 2 is $FF_2 = 81.7$ %. Thus, I obtain a fill factor loss $\Delta FF_{R_{\mathrm{s}}} = FF_2 - FF_1 = 3$ % due to resistive losses.

Also shown in in Fig. 6.13b, curve 3 is a third $J(V)$ that uses Eq. (6.22) as well but assumes a *constant* saturation current density using the value of J_0 at $V = V_{\mathrm{oc}}(AM1.5) = 681$ mV corresponding to the open circuit voltage of the triple-a cell at simulated AM1.5 conditions: $J_0 = J_0(V_{\mathrm{oc}}(\mathrm{AM1.5}))$. Curve 3 is now free of resistive effects and has an ideality factor of n_{id} of unity. The fill factor FF_3 of this ideal solar cell curve is $FF_3 = 84.2$ %, the same value that is derived by setting $V_{\mathrm{oc}} = 681$ mV, $R_{\mathrm{s}} = 0\ \Omega$, and $n_{\mathrm{id}} = 1$ into Eq. (6.1). By calculating $\Delta FF_{n_{\mathrm{id}}} = FF_3 - FF_2$ I can derive the fill factor loss due to the *non-ideal* diode behavior of my solar cells, i.e. due to the fact that the saturation current density J_0 is *larger* at the maximum power point than under open circuit conditions. For the triple-a cell, I calculate $\Delta FF_{n_{\mathrm{id}}} = 2.5$ %, showing that the resistive losses and the diode non-ideality approximately contribute with equal shares to the fill factor losses in full area a-Si:H contacted cells with high open circuit voltages.

By using the same analysis for the Al point contact cell from Tab. 6.2, I calculate $\Delta FF_{R_{\mathrm{s}}} = 2.9$ % and $\Delta FF_{n_{\mathrm{id}}} = 1.1$ % for this device. Hence, resistive losses have a similar significance in both cell types whereas the losses due to a non-ideal diode behavior are much more pronounced in the triple-a cell. I assume

that the carrier injection dependence of the recombination velocity at the c-Si/i-a-Si:H heterojunction for double/triple layer a-Si:H back contact solar cells *with very high open circuit voltages* is responsible for the diode non-ideality. As effective lifetime measurements and back side quantum efficiency measurements with bias light illumination show, the average recombination velocity in the point contact cell, the 'double' cell and the 'single' cell from Tab. 6.2 is on a higher level and depends much less on the carrier injection density.

6.5.2 Extended back side recombination velocity analysis

The effective recombination velocity S_{eff} at the back surface interface of solar cells with double/triple layer a-Si:H back contact depends on the excess carrier density, leading to a voltage dependent J_0 as described in section 6.5.1, which in turn results in a reduction in FF and V_{oc}. Such an injection dependence of S is also observed in a-Si:H coated lifetime samples, as Fig. 5.2 in chapter 5 shows. Section 6.5 derives the back side recombination velocity via the effective diffusion length from the standard front side EQE, measured at a *fixed* illumination intensity. However, if the light impinges on the front side, most electrons are generated near the front side as well as in the bulk and only a minor fraction near the back side. The illumination intensity at the back surface is unknown and low. This section evaluates the back side recombination velocity $S_{\text{B}}(\Phi)$ of solar cells with triple layer a-Si:H back contact in dependance of the illumination intensity Φ from back side EQE measurements with bias light illumination. The back side quantum efficiency measurement technique can in fact be performed easily on full area a-Si:H back contact devices because they can be fabricated bifacial by evaporating a metal grid back contact on the rear ZnO:Al conductive window instead of the full area metallization. The calculation of the back side quantum efficiency is described in appendix A.

Figure 6.14 shows the measured and simulated EQE of a solar cell with triple layer a-Si:H back contact under back side illumination with different bias light intensities. The cell uses an i-a-Si:H layer with a thickness of approximately 3 nm. The inset shows the S values derived from the simulated EQE and plotted versus the bias light intensity. The EQE measurement is performed with three different bias light intensities Φ_{BIAS}. With the highest bias light intensity $\Phi_{\text{BIAS}} = 1$ sun, the back contact exhibits the lowest surface recombination velocity $S = 130$ cm/s.

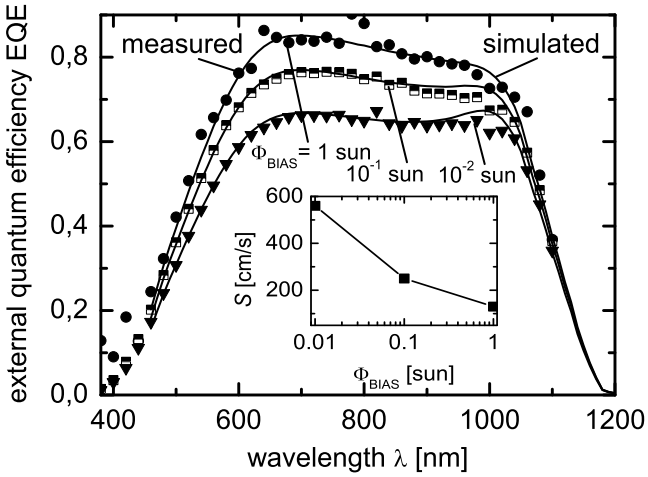

Fig. 6.14: Measured and simulated external back side quantum efficiency of a cell with full area a-Si:H back contact and intrinsic interlayer. The measurement is carried out at three different bias light intensities Φ_{BIAS}. The inset shows the surface recombination velocity derived from the EQE simulation plotted versus the light intensity. With $\Phi_{\mathrm{BIAS}} =$ 1 sun, the cell has the lowest surface recombination velocity $S = 130$ cm/s. For $\Phi_{\mathrm{BIAS}} = 10^{-1}$ sun, the simulation yields $S = 250$ cm/s and for $\Phi_{\mathrm{BIAS}} = 10^{-2}$ sun $S = 560$ cm/s.

With decreasing light intensity, the surface recombination velocity increases. For $\Phi_{\mathrm{BIAS}} = 10^{-1}$, the simulated EQE curve yields $S = 250$ cm/s and for $\Phi_{\mathrm{BIAS}} = 10^{-2}$ sun a value of $S = 560$ cm/s. The progression of S with decreasing Φ coheres with results obtained from effective lifetime measurements on a-Si:H coated wafers.

When comparing the current experiment with standard operating conditions with illumination from the front side, the impinging light is attenuated with $\exp(\alpha x)$, where α is an effective absorption coefficient for the solar spectrum. Therefore, the bis light intensity at the back side will be rather low. However, with sufficiently large bulk diffusion length, the Fermi level splitting will be constant throughout the complete solar cell and the injection level at the back side will correspond to 1-sun illumination from the back side.

Chapter 7

Heterojunction emitters

The following chapter presents the investigations on heterojunction emitters, i.e. the solar cell front side, starting with a literature review. The chapter is then divided into two parts: The first part summarizes the results from non-textured and the second part the results from textured solar cells.

7.1 Literature survey: a-Si:H emitters for p-type c-Si solar cells

The back contacts for p-type crystalline Si solar cells in chapter 6 use *p-type* a-Si:H or μc-Si-H layers. The emitter and solar cell front side of a p-type c-Si solar cell is equipped with a *n-type* amorphous Si layer. Amorphous emitters for c-Si solar cells have been widely studied during the past decades. Jensen et al. derived from modelling the cell's capacitance/voltage measurements that in the case of dominant interface recombination the p-a-Si:H/n-c-Si structure is superior concerning V_{oc} compared to its n-a-Si:H/p-c-Si counterpart [4]. This inherent disadvantage of the p-type heterojunction solar cell stems from the lower built in potential Φ_{B}, see section 2.5. To show the feasibility of industrial scale fabrication of a-Si:H/c-Si solar cells, Scherff et al. fabricated large area devices. They achieved an efficiency of $\eta = 12.9$ % on a cell area of 100 cm^2 with an a-Si:H emitter and a screen printed Al back contact [111]. Another point of interest is the addition of carbon into the emitter to increase its optical band-gap. The transmittance of light into the crystalline base is thereby enhanced leading to higher short circuit currents. However,

Müller et al. showed that the fill factor FF of such devices decreases with increasing carbon addition [112]. Orpella et al. deposited n-a-Si:C layers on p-type wafers as a source for a subsequent phosphorous emitter diffusion [113]. After PECVD deposition of the emitter, the phosphor diffuses into the p-type base by a subsequent annealing step. So far, no cell results have been reported, but the group achieved low emitter saturation current densities J_{0e} of $J_{0e} < 200 - 300$ fA/cm^2. Ulyashin et al. studied the dependence of the cell efficiency on the deposition temperature of a-Si:H emitters. A decrease in deposition temperature down to 100 °C decreased the cell efficiency only insignificantly [114]. Instead of using a-Si:H, Xu et al. fabricate n-type nano-crystalline emitters on p-type material [115]. So far, they achieve an efficiency of 14 % with solar cells that use a full area metal back contact. Garcia-Belmonte et al. perform impedance spectroscopy on solar cells with heterojunction emitters obtained by hot-wire CVD that incorporate an intrinsic film and observe an increased series resistance [116]. Jagannathan et al. used another deposition technique uses by fabricating magnetron sputtered heterojunction emitters [117]. However, these solar cells with a maximum efficiency of 10.9 % so far could not compete with devices fabricated by PECVD.

The present thesis fabricates solar cells with PECVD heterojunction emitters. To investigate their performance concerning V_{oc}, these emitters are applied to wafers equipped with a high efficiency back contact that has shown its capability in the *ipe* high efficiency standard process. Such an Al point back contact is also known from so-called PERC solar cells [94]. Solar cells from the *ipe* process that use diffused homojunction emitters combined with such a back contact reliably yield $V_{oc} \geq 670$ mV. In contrast to other research groups that use low quality full area Al back contacts which limit the cell performance, the PERC contact allows to explore the influence of the i-a-Si:H front surface passivation in the emitter on the cell's performance.

7.2 Solar cell front side passivation scheme and emitter

The requirements for an high-efficiency emitter and front side are:

- Passivated surface to achieve high open circuit voltages.

- High doping to achieve a steep band bending and a high built in potential Φ_B.
- Low optical reflectance for high short circuit currents.
- Low series resistance to reach high fill factors.

Figure 7.1a shows a sketch of the preparation sequence of an a-Si:H front side passivation scheme and emitter that meets all these requirements. The devices use 250

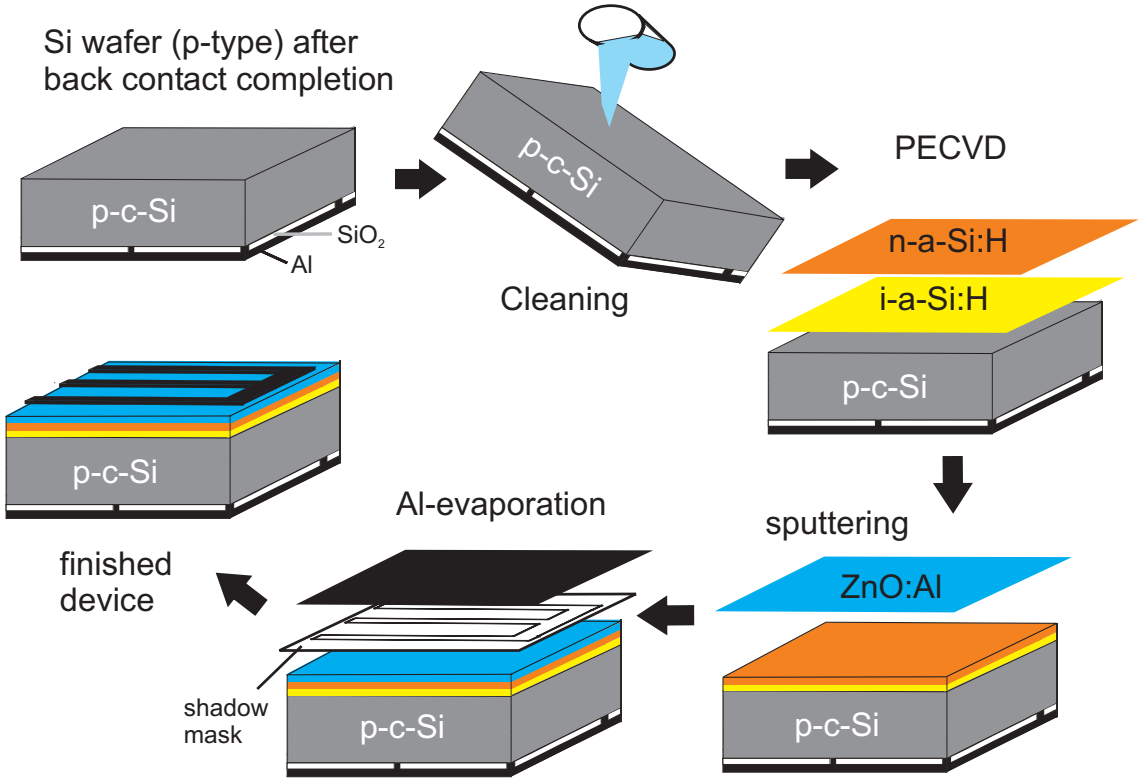

Fig. 7.1: Sketch of the preparation sequence for my cell devices equipped with heterojunction emitters. The samples use p-type $\rho = 1$ Ωcm wafers equipped with a high efficiency aluminum point back contact. The emitter consists of intrinsic and phosphorous doped a-Si:H together with a n-type ZnO:Al (non-textured samples) or ITO (textured samples) window layer. The Al contact grid evaporated through a shadow mask finishes the device.

μm thick boron-doped float-zone Si wafers with a resistivity $\rho = 1$ Ωcm. Thermal oxidation at 1000 °C forms a 200 nm thick masking oxide. A photolithography step

defines local contact areas and wet chemical etching of the SiO_2 opens small points within the oxide layer. Aluminium evaporation with a thickness of 2 μm onto the structured side completes the local metal back contact. A masking oxide protects the front surface of the wafer during the entire rear side processing. After back electrode completion, the front side masking oxide is removed by a dip in 5 % HF solution and the wafer is subsequently mounted into the PECVD setup to fabricate the emitter. An i-a-Si:H layer is deposited first for front side passivation. On top of the i-a-Si:H, a highly n-type a-Si:H emitter is deposited to obtain an asymmetrical pn-junction. The i- and n-layers are fabricated in two separate PECVD chambers to avoid cross-contamination. The i-a-Si:H layer used is the standard surface passivation layer of this thesis deposited onto the wafer with a silane flow of $[SiH_4]$ = 10 sccm, a chamber pressure of 0.52 mbar, a plasma frequency of ν_p = 13.56 MHz, and a glow discharge power of 8.8 mW/cm^2 at a substrate temperature T_S = 130 °C. The n-layers use phosphine (PH_3) as a doping gas, delivered in gas bottles with a dilution of 2 % in silane. The n-a-Si:H is deposited with diluted PH_3 flow of $[PH_3]$ = 2 sccm, an additional silane flow of $[SiH_4]$ = 2 sccm, a chamber pressure of 0.52 mbar, a plasma frequency of ν_p = 13.56 MHz, and a glow discharge power of 16.6 mW/cm^2. A low series resistance to the n-a-Si:H emitter and to the front contact grid is reached by subsequently sputtering either 80 nm ZnO:Al at room temperature or 80 nm ITO at 200 °C as a conductive window layer. The thickness of the TCO is adapted to achieve a low optical reflectance. The device is completed by evaporating 2 μm Al through a shadow mask that makes the front contact grid. After emitter completion, the devices require an annealing step at 200-220 °C for 10 min to achieve an optimum solar cell efficiency [86]. As for the double/triple layer a-Si:H back contact, the thickness of the i-layer has to be carefully tuned. Apart from its positive function as a surface passivation layer, the thin undoped film causes drawbacks concerning the solar cell performance. Firstly, a-Si:H is a good absorber material but lacks electronic quality. If a-Si:H is used on the front side of a high quality crystalline Si base, it absorbs light but the thereby generated carriers recombine before they can be collected. The a-Si:H interlayer therefore reduces the total short circuit current of the device. Secondly, the intrinsic a-Si:H interlayer has a high resistivity and hampers the current transport through the solar cell. A decrease of the fill factor caused by a high series resistance but also by an increased diode ideality factor is therefore observed in heterojunction devices with intrinsic

interlayer, similar as described for cells with double/triple layer a-Si:H back contact in chapter 6. To achieve a maximum solar cell performance, it is desired to minimize the thickness d_i of the intrinsic interlayer. However, the i-a-Si:H film has to be thick enough to obtain a good passivation of the c-Si surface and hence high V_{oc} values in solar cells. To determine the electric surface quality of the a-Si:H/c-Si emitter interface, I fabricate lifetime samples and measure τ_{eff} by the QSSPC technique.

Figure 7.2 shows the effective lifetime of such symmetrical n-a-Si:H/i-a-Si:H/p-c-Si/i-a-Si:H/n-a-Si:H samples. The inset shows the sample structure. The plot shows a variation of the intrinsic a-Si:H interlayer thickness of $d_i = 0$ - 5 nm. The phosphorous doped a-Si:H thickness is kept constant at $d_n = 40$ nm. I determine the effective minority carrier lifetime at an injection level that corresponds to an illumination with an areal power density of 100 mW/cm^2.

According to Fig. 7.2, low minority carrier lifetimes with values around $\tau_{eff} = 10$ μs are measured without intrinsic interlayer, i.e. when the n-type amorphous layer is directly deposited onto the Si wafer surface. When increasing the amorphous intrinsic interlayer thickness d_i, the minority carrier lifetime τ_{eff} also increases up to values $\tau_{eff} > 1$ ms. Above an interlayer thickness of $d_i \approx 2.5$ nm there is no further improvement observable in surface passivation quality. Therefore, all devices with heterojunction emitters in this thesis use such an approximately 2.5 nm thick i-a-Si:H layer. To achieve high short circuit currents, not only the intrinsic film but also the n-type doped a-Si:H emitter has to be as thin as possible. The contribution to the short circuit current of charge carriers generated within the n-a-Si:H can be neglected because their recombination probability is close to unity [118]. For all solar cells in this thesis, I therefore use an n-layer thickness d_n of only $d_n = 5$ nm.

7.3 Non-textured devices

Figure 7.3a shows a sketch of the non-textured devices equipped with heterojunction emitters [1]. Table 7.1 summarizes the photovoltaic output parameters of two solar cells from different wafers measured under AM1.5G conditions. Both use an approximately 2.5 nm thick intrinsic interlayer and an approximately 5 nm thick

[1] Solar cells use front side textures in order to decrease the optical reflectivity.

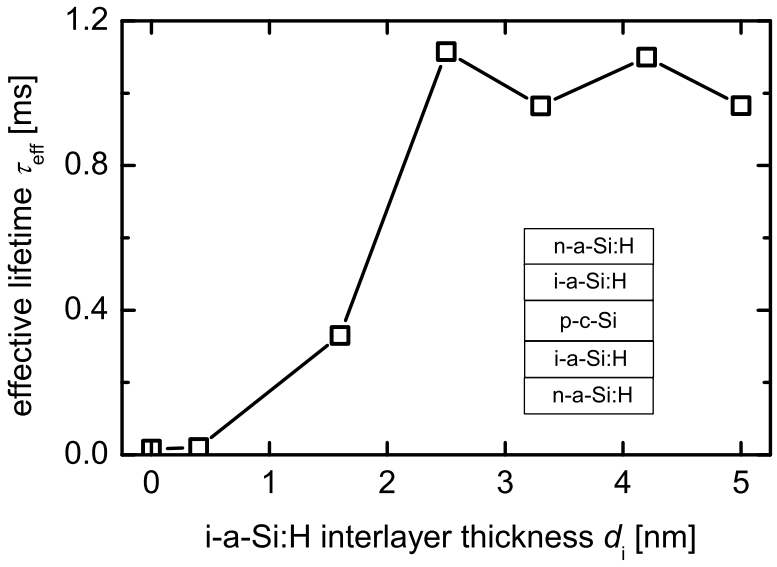

Fig. 7.2**:** Effective lifetime of p-type float-zone Si wafers with a resistivity of 1 Ωcm. The samples are symmetric with a double layer of intrinsic and highly phosphorous doped a-Si:H on each side. The intended application of the layer system is a front contact (emitter) of a p-type heterojunction solar cell. The inset shows the sample structure. The thickness of the n-a-Si:H layer is kept constant at 40 nm and the thickness of the i-a-Si:H interlayer is varied. The effective lifetime is determined at an injection level that corresponds to about 1 sun illumination at AM 1.5 conditions. The graph shows that a minimum intrinsic interlayer thickness of only about 2.5 nm is necessary to reach a good surface passivation. A further increase in thickness of the i-a-Si:H does not improve the effective lifetime. Lines are guides to the eye.

n-type amorphous emitter. The cell with the best efficiency $\eta = 17.4$ % (sample a-ZNO) has a high fill factor of $FF = 79$ % and an open circuit voltage of $V_{\mathrm{oc}} = 670$ mV. The other cell (sample b-ZNO) has higher open circuit voltage of $V_{\mathrm{oc}} = 683$ mV but also a lower fill factor of $FF = 76.4$ %. Most likely, the difference in fill factor and open circuit voltage is caused by a slight difference in i-a-Si:H layer thickness between the two wafers, as both, fill factor and open circuit voltage are very sen-

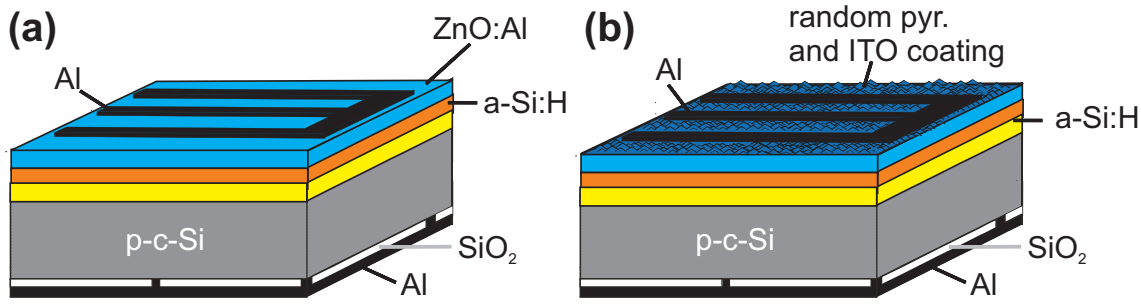

Fig. 7.3: Sketch of (a) flat and (b) textured solar cells fabricated on p-type $\rho = 1$ Ωcm FZ wafers equipped with a high efficiency PERC-type back contact. The emitter consists of intrinsic and phosphorous doped a-Si:H together with a n-type ZnO:Al (non-textured samples (a)) or ITO (textured samples (b)) window layer. The Al contact grid is subsequently evaporated through a shadow mask.

sitive on the i-a-Si:H layer thickness. Due to the fact that the deposition time for the 2.5 nm thick i-layer is very short, there are definitely slight thickness variations between different cell runs. Geiger showed, that the relatively low fill factors of the non-textured devices with n-a-Si:H emitter and i-a-Si:H interlayer mainly stem from increased diode ideality factors [119]. A similar observation as described in chapter 6 for the solar cells with double/triple a-Si:H layer back contact. Figure 7.4 shows

Tab. 7.1: Photovoltaic output parameters open circuit voltage V_{OC}, short circuit current density J_{SC}, fill factor FF, and power conversion efficiency η under AM1.5G conditions of two solar cells with heterojunction emitter and SiO_2/Al-point back contact. The cell area is $A = 4$ cm^2.

Wafer	V_{OC} [mV]	J_{SC} [mA/cm^2]	FF [%]	η [%]
a	670	32.7	79.0	17.4
b	683	32.5	76.4	17.0

the measured external quantum efficiency and the measured reflection of sample a. The simulation of the EQE, also depicted in Fig. 7.4 (straight line), is based on an optical model that assumes a stack of plane-parallel flat layers with abrupt

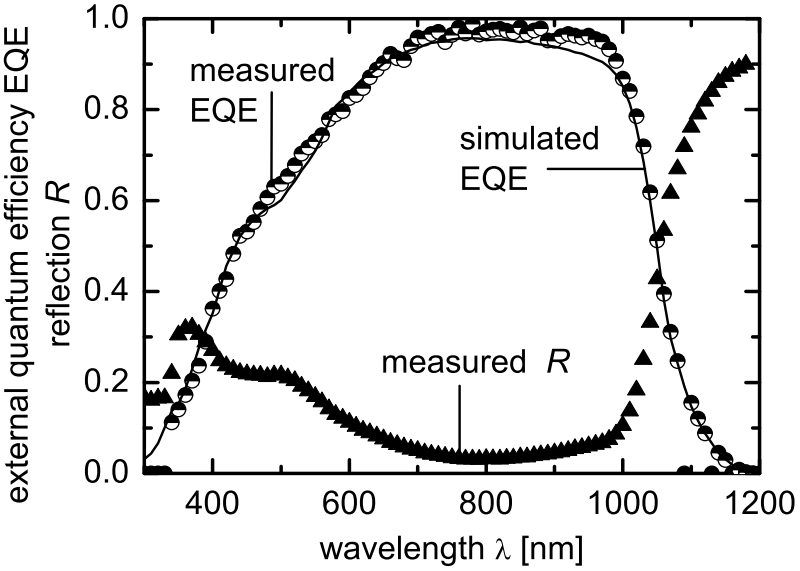

Fig. 7.4: Measured quantum efficiency (circles) and reflection (triangles) as well as simulated quantum efficiency (continuous line) of the sample a from Tab. 7.1

interfaces through which a plane wave propagates coherently [34]. I measure the external quantum efficiency with the light beam focused in between the grid contact fingers. The contact grid coverage is 5 %. When integrating the EQE over all wavelengths with the AM1.5 spectrum to derive the short circuit current density J_{sc}, I derive a value that is exactly 5 % higher than the J_{sc} that I get from the I/V-data. This agreement nicely demonstrates the accuracy of the I/V-measurement. For the simulation, I assume a thickness $d_{\mathrm{ZnO:AL}}$ of the ZnO:Al window layer $d_{\mathrm{ZnO:AL}} = 80$ nm, a total a-Si:H thickness $d_{\mathrm{a-Si:H}} = 10$ nm, a wafer thickness $d_{\mathrm{Si}} = 250$ μm, a rear oxide thickness $d_{\mathrm{ox}} = 200$ nm and an aluminum back contact thickness of $d_{\mathrm{Al}} = 2$ μm. Concerning the electronic properties of the crystalline base, I assume a collection efficiency $f_{\mathrm{C}} = 1$ and a surface recombination velocity S = 0, thus the simulated curve basically corresponds to the absorbance in the c-Si. The simulation of the EQE matches well with the measured data and shows that both surfaces are excellently passivated.

7.4 Textured devices

For the textured samples, as sketched in Fig. 7.3b, the front side is additionally etched in a KOH/isopropanol solution at a temperature of 80 °C for 20 minutes prior to the a-Si:H emitter fabrication and has therefore a random pyramid structure. Apart from the textured front side, these cells are similar to those described in section 7.3 and use the same PERC-type back contact and the same a-Si:H emitter.

However, using a textured c-Si surface and an a-Si:H emitter together with a ZnO:Al window layer does not lead to satisfying results. The devices then only yield very low open circuit voltages $V_{\mathrm{oc}} < 500$ mV and low fill factors FF < 60 %. From analyzing the current/voltage curves of the textured devices with ZnO:Al window layer, I derive that the low fill factors $FF < 60$ % stem from very high series resistances R_{S}. A low parellel resistance (shunt) that also lowers the fill factor, potentially occurring by a direct contact between the grid and the crystalline Si base due to an uneven ZnO:Al coverage, is *not* observed. A slightly increased R_{S} in textured devices compared to flat devices with the same TCO thickness can be expected and is caused by the enlarged effective path that carriers have to travel in the TCO. However, the measured series resistance in the textured devices with ZnO:Al window layer is much higher than one would expect.

Figure 7.5 shows a micrograph performed by scanning electron microscopy on a textured emitter coated with a ZnO:Al window layer. The TCO perfectly and homogeneously covers all pyramids, even the spiky tops. Olibet observed similar effects on textured heterojunction emitters with ZnO:Al window layers [120]. Maydell et al., however, achieve good fill factors and good V_{oc} values with textured emitters together with ZnO:Al window layers [121]. In my case, using indium doped tin oxide (ITO) instead of the ZnO:Al yields better results. The series resistance is now much lower and the open circuit voltage much higher than with ZnO:Al. Note that the improvement in series resistance is more than one order of magnitude but the sheet resistance of the ITO and the ZnO:Al are similar. The sheet resistance measured on 1 μm thick layers is $R_{\mathrm{sh}} = 6\ \Omega_{\mathrm{sq}}$ for the ITO and $R_{\mathrm{sh}} = 8\ \Omega_{\mathrm{sq}}$ for the ZnO:Al. It is an open question why the ITO on textured a-Si:H emitters yields much better results in this case.

Table 7.2 lists the photovoltaic output parameters open circuit voltage V_{oc}, short circuit current density J_{sc}, fill factor FF, and power conversion efficiency η

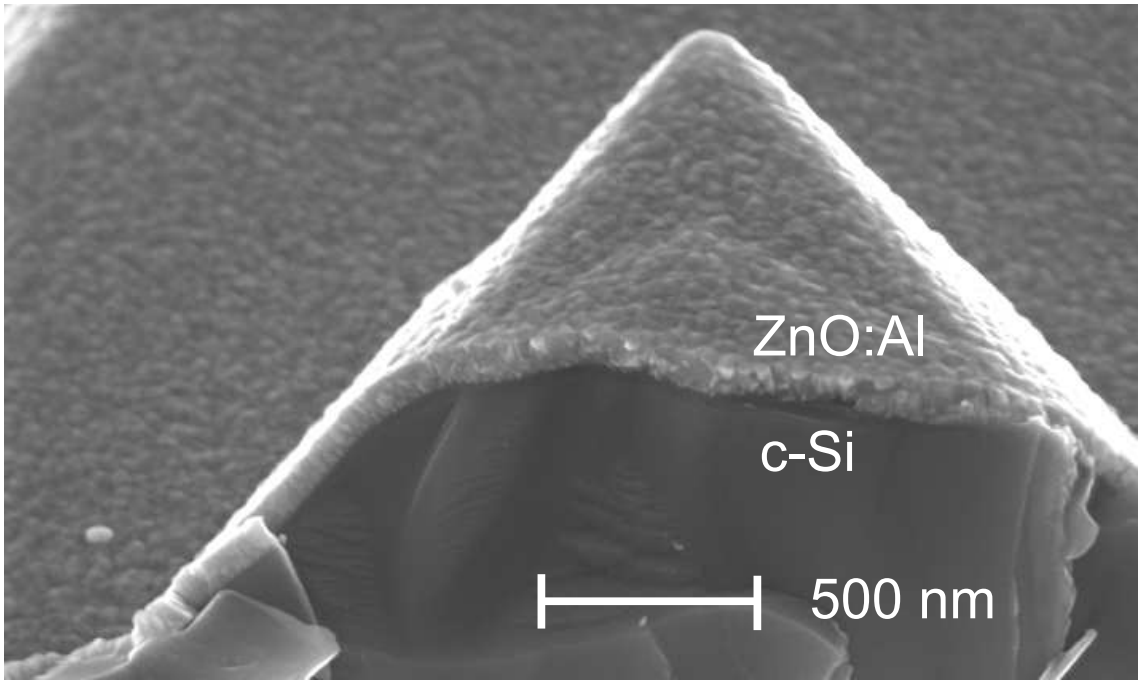

Fig. 7.5: Scanning electron micrograph cross section of a random textured monocrystalline Si surface coated with an a-Si:H emitter and a 80 nm thick ZnO:Al window layer. The ZnO:Al perfectly and homogeneously covers the spiky Si surface.

of two textured solar cells equipped with a-Si:H emitters and ITO window layers. For comparison, Tab. 7.2 shows one sample without intrinsic interlayer, sample c,

Tab. 7.2: Photovoltaic output parameters open circuit voltage V_{OC}, short circuit current density J_{SC}, fill factor FF, and power conversion efficiency η under AM1.5G conditions of two solar cells with heterojunction emitter and SiO_2/Al-point back contact. The cell area is $A = 2$ cm^2. Sample c is solely equipped with a n-a-Si:H emitter. Sample d uses an i-a-Si:H/n-a-Si:H emitter layer stack.

Wafer	V_{OC} [mV]	J_{SC} [mA/cm^2]	FF [%]	η [%]
c	612	36.7	73	16.4
d	660	37.7	74.3	18.5

and one with i-a-Si:H passivation film (sample d). Both cells have a comparable short circuit current density and fill factor. In terms of V_{oc}, the cell from wafer c with i-a-Si:H layer (V_{oc} = 660 mV) clearly outperforms to the cell without i-layer from wafer b (V_{oc} = 612 mV). The difference in V_{oc} emphasizes the role of the thin undoped film for surface passivation. Note that, with a modified n-layer using a lower phosphorous content, possibly higher open circuit voltages can be achieved even without an i-layer [122].

The most unsatisfactory parameter of the textured heterojunction emitter solar cells at the moment are the fairly low short circuit current and especially the low fill factor. I am confident that further experiments overcome the low short circuit current problem with a more homogeneous texture. The best cells concerning the short circuit current have already $J_{sc} \geq 38$ mAcm^{-2}. Much higher J_{sc} can not be expected with a full area i-a-Si:H/n-a-Si:H/ITO emitter due to the absorption that takes place in these three layers.

The question remains whether the low fill factors stem from a high series resistance R_S or from a non ideal diode behavior leading to an ideality factor $n_{id} > 1$. A fill factor analysis as described in section 6.5.1 performed on the cells of tab. 7.2 allows to separate the influence of diode ideality and series resistance on the fill factor. The results show that the cells have ideality factors close to unity. A non-ideal diode behavior in heterojunction solar cells stems from the injection dependence of the surface recombination velocity S, which is predominant in devices that use an intrinsic interlayer for surface passivation. Table 7.2 shows that the device *without* i-a-Si:H interlayer has an even *lower* fill factor than the device with i-layer. Hence, at present the losses on the fill factor due to a high series resistance are much more pronounced than the losses due to a non ideal diode behavior. In the textured heterojunction emitter solar cells, the intrinsic layer does currently not limit the fill factor, neither by its current hampering high resistivity nor by causing a non-ideal diode behavior.

Chapter 8

Complete heterojunction solar cells

The following chapter presents the results of solar cells that combine the heterojunction emitter from chapter 7 (front side) with the heterojunction back contact from chapter 6 (rear side). After a short literature review, the chapter is subdivided into two sections. The first section introduces the samples and the second section summarizes the device results of the present thesis.

8.1 Literature survey: p-type heterojunction solar cells

The research activities concerning heterojunction solar cells have significantly increased after Taguchi et al. showed the high efficiency potential of such devices that are completely fabricated at low temperature [2]. As Taguchi et al. fabricate their solar cells on *n-type* c-Si material, the extended interest of current research is to show the feasibility of high-efficiency *p-type* c-Si heterojunction solar cell fabrication [5]. Maydell et al. used a p-type wafer equipped with a n^+-a-Si:H emitter and a p^+-a-Si:H back side without intrinsic interlayers [121]. The front contact uses a ZnO:Al conductive window layer and the Al back contact was directly evaporated onto the p^+-a-Si:H film. They achieved an efficiency $\eta = 17.4$ % with $V_{oc} = 635$ mV. Most likely, the efficiency η of this device is limited by the high recombination velocity at the front and rear a-Si:H/c-Si interfaces due to the direct contact of the doped

a-Si:H with the c-Si. Muñoz et al. used a-Si:H emitters with intrinsic interlayer and heterojunction back contacts similar to the double layer back contact of this thesis, fabricated by the hot wire chemical vapor deposition technique [123]. However, they achieve only low efficiencies of $\eta = 13.1$ % with $V_{oc} = 617$ mV on a cell area of 1.4 cm^2. With the same deposition technique and the same device assembly, Wang et al. achieved $\eta = 18.1$ % with $V_{oc} = 666$ mV on a cell area of 1 cm^2 [7]. However, large scale a-Si:H fabrication with hot-wire CVD is not yet established and the industrial relevance of this technique is open. In contrast, PECVD for the deposition of a-Si:H is meanwhile widespread in the solar cell and flat panel industry.

This thesis uses a similar solar cell assembly as Wang et al. and Muñoz et al. but instead of the hot-wire CVD the a-Si:H layers are deposited by PECVD. The cell uses the combination of the back contact A from chapter 6 and the emitter from chapter 7.

8.2 Samples

Figure 8.1 shows a sketch of the complete p-type heterojunction solar cell. The

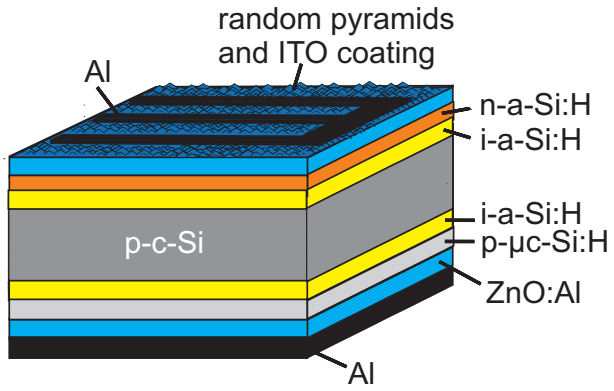

Fig. 8.1: Sketch of the solar cell device with both heterojunction front- and back side. The emitter consists of i/n-a-Si:H together with an ITO window layer. The back contact consists of a i-a-Si:H/p-μc-Si:H layer stack and a ZnO:Al dielectric mirror together with an Al back contact.

combination of the a-Si:H front side passivation scheme and emitter (described in chapter 7) with the full area a-Si:H back contact (shown in chapter 6) creates a high-

efficiency p-type heterojunction Si solar cell allowing the device fabrication without any high temperature step.

Tab. 8.1 summarizes the photovoltaic output parameters of such solar cells on three wafers, a-c. The best two cells of each wafer are shown. All cells in the

Tab. 8.1: Photovoltaic output parameters open circuit voltage V_{OC}, short circuit current density J_{SC}, fill factor FF, and power conversion efficiency η under AM1.5G conditions of solar cells with heterojunction emitter and heterojunction back contact.

Sample	Area [cm22]	V_{OC} [mV]	J_{SC} [mA/cm^2]	FF [%]	η [%]
a1	2	670	35.7	75.6	18.1
a2	2	668	35.9	75.5	18.1
b1	4	670	37.4	72.6	18.1
b2	1	663	36.7	74.3	18.1
c1	4	676	37.4	71	18.0
c2	4	678	37.2	70.5	17.8

table use the same triple layer back contact with i-a-Si:H interlayer thickness of 3 nm as described in chapter 6. The n-a-Si:H in the front side emitter slightly differs in thickness, wafer a has a thicker n-a-Si:H layer $d_{\mathrm{n-a-Si:H}} = 10$ nm, whereas wafers b and c have $d_{\mathrm{n-a-Si:H}} = 5$ nm. The thicker n-a-Si:H layer leads to a lower short circuit current of the cells on wafer a. For all cells, the fill factor that I obtain is the most unsatisfactory parameter. To find out whether the low FF is caused by a high series resistance R_{s} or by a non ideal diode behavior leading to an ideality factor $n_{\mathrm{id}} > 1$, I perform a fill factor analysis with the cells as described in chapter 6. The results show that both, a non ideal diode behavior and a high series resistance contribute to the low fill factors. I calculate the resistive losses on the fill factor by $\Delta FF_{R_{\mathrm{s}}} = FF_0 - FF_{\mathrm{M}}$ with FF_0 being the fill factor without resistive effects and FF_{M} the measured fill factor. For the cells shown in Tab. 8.1, I compute 3.6 % $\leq \Delta FF_{R_{\mathrm{s}}} \leq$ 8.6 % with an arithmetic mean at $\Delta FF_{R_{\mathrm{s}}} = 7.3$ %. For the fill factor loss due to the non-ideal diode behavior I construct $J(V)$ curves with ideality factors $n_{\mathrm{id}} = 1$ and calculate the loss by $\Delta FF_{n_{\mathrm{id}}} = FF_1 - FF_{\mathrm{M}}$, with FF_1 being the fill factor of the ideal curve and FF_{M} the measured fill factor. For the cells

shown in Tab. 8.1, I derive 3.3 % $\leq \Delta FF_{R_s} \leq$ 6.4 % with an arithmetic mean at $\Delta FF_{R_s} = 4.8$ %. These results show, that at present the losses on the fill factor due to a high series resistance are more pronounced than the losses due to a non ideal diode behavior. Further studies have to unveil the causes for the increased series resistance in order to achieve higher efficiencies with p-type heterojunction solar cells.

Conclusions and Outlook

This thesis shows that both high quality back contacts and emitters with excellent passivating and resistive properties to p-type c-Si are obtained by PECVD a-Si:H deposition. The best device with diffused emitter and heterojunction back contact delivers a confirmed efficiency $\eta = 21$ %. Using a high-quality back contact with thermal oxide passivation in combination with a heterojunction emitter, the best solar cell yields an efficiency $\eta = 18.5$ %. By combining both heterojunction front- and back contacts to a p-type c-Si solar cell that is completely fabricated at temperatures below 220 °C, a maximum efficiency of $\eta = 18.1$ % is achieved. However, analysis of the saturation current densities on the front side and of the charge carrier transport equations at the back side reveal that heterojunction solar cells based on p-type c-Si severely suffer from the band offset distribution at the a-Si:H/c-Si interface. The low condution band offset ΔE_{C} at the front side (emitter) leads to a lower built-in potential. Due to this situation, n-a-Si:H/p-c-Si emitters have a lower maximum open circuit voltage V_{oc} limit than their n-c-Si counterparts, and the front surface recombination is more pronounced. At the back contact, the large valence band offset $\Delta E_{\mathrm{V}\Delta}$ leads to a current hampering barrier for majority carriers that increases the series resistance. Due to these inherent disadvantages, p-type base heterojunction solar cells will most likely never reach the performance of their n-type counterparts. On n-type wafers, Sanyo achieves now efficiencies in excess of 22 % [124].

Nevertheless, the presented a-Si:H back contact scheme for p-type solar cells overcomes the efficiency limitations of a standard thermally fired Al back contact and enables to fabricate high-efficiency p-type solar cells with diffused emitters. The heterojunction back contact leads to an increased open circuit voltage of such cells, even without the insertion of an intrinsic surface passivation layer. Ehling et al. applied the heterojunction back contact of this thesis to large area solar cells

equipped with diffused low-quality industrial emitters and screen printed contact grid. They have shown that a significant efficiency improvement is delivered by the novel back contact. Recently, a gain of up to 0.8 % in efficiency compared to the best Al back contact reference has been reported [125]. For a 30 MW solar cell production line, such an efficiency improvement would legitimate an invest of roughly 4 million EUR, assumed that the back contact deposition process needs consumables of 150.000 EUR annually and causes a yield loss of 2 % [126]. Note that the potential efficiency improvement of the a-Si:H back contact is much larger than 0.8 %. A combination of the novel back contact with a selective emitter should enable to fabricate industrial solar cells with efficiencies in excess of 19 %. Thus, together with an optimized emitter, the heterojunction back contact is able to deliver a total efficiency gain of more than 2 %.

Appendix A

Quantum efficiency model

A.1 Optical model

To calculate the transmission through the transparent back contact, I use an optical model that assumes a stack of plane-parallel flat layers with abrupt interfaces through which a plane wave propagates coherently [34]. Every layer k has a complex refractive index

$$\tilde{n_{\mathrm{k}}} = n_{\mathrm{k}} + i\kappa_{\mathrm{k}} \tag{A.1}$$

with the real part n (dispersion) and the imaginary part κ (absorption). With $\tilde{n_{\mathrm{k}}}$ one can calculate the reflexion coefficient r_{kl} and the transmission coefficient t_{kl} with the fresnel formalism:

$$r_{\mathrm{k,l}} = \frac{\tilde{n_{\mathrm{k}}} - \tilde{n_{\mathrm{l}}}}{\tilde{n_{\mathrm{k}}} + \tilde{n_{\mathrm{k}}}}, \tag{A.2}$$

$$t_{\mathrm{k,l}} = \frac{2\tilde{n_{\mathrm{k}}}}{\tilde{n_{\mathrm{k}}} + \tilde{n_{\mathrm{l}}}}. \tag{A.3}$$

I use a matrix formalism with as pointed out in Ref. [127] to describe the wave propagation in the layer system,

$$M^{\mathrm{I}}_{\mathrm{k,k+1}} = \frac{1}{t_{\mathrm{k,k+1}}} \begin{pmatrix} 1 & r_{\mathrm{k,k+1}} \\ r_{\mathrm{k,k+1}} & 1 \end{pmatrix}, \tag{A.4}$$

$$M^{\mathrm{P}}_{\mathrm{k}} = \begin{pmatrix} \Phi_{\mathrm{k}}^{-1} & 0 \\ 0 & \Phi_{\mathrm{k}} \end{pmatrix}, \Phi_{\mathrm{k}} = \exp\left(i\frac{\omega\tilde{n_{\mathrm{k}}}d_{\mathrm{k}}}{c_0}\right), \tag{A.5}$$

where Φ_{k} is a function of the layer thickness d_{k}, the frequency ω and the speed of light c_0. Matrix M^{I} describes the interfaces and matrix M^{P} the bulk. With Eqs. A.4 one calculates

$$\begin{pmatrix} E_0^+ \\ E_0^- \end{pmatrix} = M_{0,1}^{\mathrm{I}} M_1^{\mathrm{P}} \dots M_{\mathrm{k,k-1}}^{\mathrm{I}} M_l^{\mathrm{P}} M_{\mathrm{k,k+1}}^{\mathrm{I}} \dots M_1^{\mathrm{P}} M_{\mathrm{k,k+1}}^{\mathrm{I}} \begin{pmatrix} E_{\mathrm{m}}^+ \\ 0 \end{pmatrix} \tag{A.6}$$

$$\equiv M^{\mathrm{S}} \begin{pmatrix} E_{\mathrm{m}}^+ \\ 0 \end{pmatrix} \equiv \begin{pmatrix} g_{11} & g_{12} \\ g_{21} & g_{22} \end{pmatrix} \begin{pmatrix} E_{\mathrm{m}}^+ \\ 0 \end{pmatrix} \tag{A.7}$$

whereas E^+ is the transmitted and E^- the reflected amplitude of a system with m layers. The reflection R and the transmission T follows

$$R = \frac{\mid E_0^- \mid^2}{\mid E_0^+ \mid^2} = \frac{\mid g_{21} \mid^2}{\mid g_{11} \mid^2}, \tag{A.8}$$

$$T = \frac{n_{\mathrm{m+1}}}{n_0} \frac{\mid E_{\mathrm{m+1}}^- \mid^2}{\mid E_0^+ \mid^2} = \frac{n_{\mathrm{m+1}}}{n_0} \frac{1}{\mid g_{11} \mid^2}. \tag{A.9}$$

A.2 Electrical model

The quantum efficiency

$$IQE = \int_0^w g(x) f_{\mathrm{c}}(x) dx \tag{A.10}$$

depends on the normalized generation rate $g = G/\Phi$ and the collection efficiency $f_{\mathrm{c}}(x)$. To calculate the generation, multiple reflections of the light inside the solar cell have to be considered. For a solar cell illuminated from the rear, considering the *internal* reflections at the back- and front side lead to the generation rate

$$\begin{aligned} G = {} & \Phi\alpha(1 - R_{\mathrm{Bi}})[\exp(\alpha(x - d)) + R_{\mathrm{Fi}}\exp(-\alpha(x + d)) \\ & + R_{\mathrm{Bi}} R_{\mathrm{Fi}} \exp(\alpha(x - 3d)) + ...], \end{aligned} \tag{A.11}$$

with d as the cell's thickness, α as the absorption coefficient, R_{Bi} as the internal back side reflectance and R_{Fi} as the internal front side reflectance. This equation holds for a device with planar front- and back side. The devices in this thesis are textured on the front side. To approximate the generation for such a case, I make the following considerations. The first path of the light enters the device perpendicular to a planar surface and the beam of light is not refracted. On the textured front side,

the light is refracted at the pyramids. For an exact calculation of the generation, a total randomization of the angular distribution at the front side, i. e. Lambertian distribution, has to be taken into account. To simplify, I use an effective path angle of $\theta = 60°$ that holds for a complete randomization of the light according to Ref. [27]. Therewith, the generation rate writes as

$$\begin{aligned} G &= \Phi\alpha(1-R_{\mathrm{Bi}})[\exp(\alpha(x-d)) + R_{\mathrm{Fi}}\exp(-\alpha(x+d)/\cos\theta) \\ &\quad + R_{\mathrm{Bi}}R_{\mathrm{Fi}}\exp(\alpha(x-3d)/\cos\theta) + ...]. \end{aligned} \tag{A.12}$$

From the one-dimensional diffusion equation, the IQE of the first path $\mathrm{IQE}_{1\mathrm{st}}$ without internal front side reflection is described by

$$\begin{aligned} \mathrm{IQE}_{1\mathrm{st}} &= \frac{J_{\mathrm{sc}}}{q\phi_0} \\ &= \frac{\alpha L_{\mathrm{n}}}{\alpha^2 L_{\mathrm{n}}^2 - 1} \\ &\quad \left[\frac{\frac{D_{\mathrm{n}}\alpha}{S_{\mathrm{B}}} + 1 - (\cosh(\frac{d}{L_{\mathrm{n}}}) + \frac{D_{\mathrm{n}}}{S_{\mathrm{B}}L_{\mathrm{n}}}\sinh(\frac{d}{L_{\mathrm{n}}}))\exp(-\frac{d}{L_{\mathrm{n}}})}{\sinh(\frac{d}{L_{\mathrm{n}}}) + \frac{D_{\mathrm{n}}}{S_{\mathrm{B}}L_{\mathrm{n}}}\cosh(\frac{d}{L_{\mathrm{n}}})} - L_{\mathrm{n}}\alpha\exp(-\frac{d}{L_{\mathrm{n}}}) \right], \end{aligned} \tag{A.13}$$

calculated with the generation $G_{1\mathrm{st}} = \alpha\exp(\alpha(x-d))$. To derive the IQE for multiple internal reflections, I use a formalism according to Ref. [22]. For the light reflected at the front contact, Eq. (A.12) shows that an additional term $G_{2\mathrm{nd}} = -R_{\mathrm{Fi}}\cos\theta\ G_{1\mathrm{st}}(-\alpha/\cos\theta)$ adds to the total generation rate. Since the light travels in the opposing direction, the sign in the exponent switches and the IQE of the second path $\mathrm{IQE}_{2\mathrm{nd}}$ therefore follows

$$\mathrm{IQE}_{2\mathrm{nd}} = -R_{\mathrm{Fi}}\cos\theta\ \mathrm{IQE}_{1\mathrm{st}}(-\alpha/\cos\theta). \tag{A.14}$$

For an infinite number of reflections, the IQE calculates from a geometrical sum to

$$\mathrm{IQE} = \frac{\mathrm{IQE}_{1\mathrm{st}}(\alpha/\cos\theta) - \mathrm{IQE}_{2\mathrm{nd}}}{1 - R_{\mathrm{Fi}}R_{\mathrm{bi}}\exp(-2\alpha d)} - \mathrm{IQE}_{1\mathrm{st}}(\alpha/\cos\theta) + \mathrm{IQE}_{1\mathrm{st}}(\alpha). \tag{A.15}$$

The IQE does not take into account the reflection at the ZnO:Al back contact and the absorption in the ZnO:Al as well as the a-Si:H layers that occur in the heterojunction back contacts before the light enters the c-Si absorber. Thus, to fit the measured external quantum efficiency data, I use the calculated transmission from section A.1, Eq. (A.8) to derive

$$\mathrm{EQE} = T\ \mathrm{IQE}. \tag{A.16}$$

The transmission T considers the reflection at the ZnO:Al and the absorption in the ZnO:Al as well as a-Si:H layers. The reflection mainly depends on the ZnO:Al layer thickness and the absorption in the wavelength regime of the EQE measurement is mainly influenced by the a-Si:H layer thickness.

Publication list

1. P. J. Rostan, J. Maier, T. Kirchartz, U. Rau, F. Einsele, R. Merz, M. B. Schubert and J. H. Werner, *a-Si:H/c-Si Heterojunction Solar Cells on p-type c-Si Wafers*, Techn. Digest of the 17th Internat. Photovolt. Sol. En. Conf., Fukuoka (2007) p. 391

2. C. Ehling, M. B. Schubert, R. Merz, P. J. Rostan, and J. H. Werner, *0.4 % Efficiency Gain by Novel Back Contact*, Techn. Digest of the 17th Internat. Photovolt. Sol. En. Conf., Fukuoka (2007) p. 404

3. P. J. Rostan, S. Keller, A. Hauser, J. Haase, I. Melnyk, P. Fath, A. Eder, A. Pollak, R. Hendel, and H. N. Nussbaumer, *New Generation Production Technology for c-Si Solar Cells*, in Proc. of the 22nd Europ. Photovolt. Sol. En. Conf., Milano (2007) p. 1539

4. F. Einsele, P. J. Rostan, M. Schubert, and U. Rau, *Recombination and resistive losses at ZnO/a-Si:H/c-Si interfaces in heterojunction back contacts for Si solar cells*, Journal of Applied Physics, **102**, 094507

5. F. Einsele, P. J. Rostan, and U. Rau, *Resistive Losses at c-Si/a-Si:H/ZnO Contacts for Heterojunction Solar Cells*, in Mater. Res. Soc. Symp. Proc., San Francisco (2007) p. 0989-A18-04

6. P. J. Rostan, U. Rau and J. H. Werner, *TCO/(n-type)a-Si:H/(p-type)c-Si heterojunction solar cells with high open circuit voltage*, in Proc. 21^{st} Europ. Photovolt. Solar En. Conf., edited by W. Palz, H. Ossenbrink, and P. Helm (WIP Renewable Energies, München, 2006) p. 1181

7. J. Mattheis, P. J. Rostan, K. Orgassa, U. Rau, and J. H. Werner, *Carrier*

collection in Cu(In,Ga)Se_2 solar cells with graded band gaps and transparent ZnO:Al back contacts, Solar Energy Materials and Solar Cells, **91**, 689 (2007)

8. P. J. Rostan, U. Rau, V. X. Nguyen, T. Kirchartz, M. B. Schubert, and J. H. Werner, *Low-temperature a-Si:H/ZnO/Al back contacts for high-efficiency silicon solar cells*, Solar Energy Materials and Solar Cells **90**, 1345 (2006)

9. P. J. Rostan, C. Berge, U. Rau, and J. H. Werner, *Anodizing method yielding multiple porous seed layers for the epitaxial growth of mono-crystalline Si films*, J. Echem. Soc. **153**, 133 (2006)

10. W. Brendle, V. X. Nguyen, K. Brenner, P. J. Rostan, A. Grohe, E. Schneiderlöchner, R. Preu, U. Rau, G. Palfinger, and J. H. Werner, *Low temperature back contact for high efficiency silicon solar cells*, in Proc. 20^{th} Europ. Photovolt. Solar En. Conf., edited by W. Palz, H. Ossenbrink (WIP Renewable Energies, München, 2005) p. 705

11. K. v. Maydell, H. Windgassen, W. A. Nositschka, U. Rau, P. J. Rostan, J. Henze, J. Schmidt, and M. Scherff, *Basic electronic properties and technology of TCO/a-Si:H(n)/c-Si(p) heterostructure solar cells: A German network project*, in Proc. 20^{th} Europ. Photovolt. Solar En. Conf., edited by W. Palz, H. Ossenbrink (WIP Renewable Energies, München, 2005) p. 822

12. P. J. Rostan, U. Rau, V. X. Nguyen, T. Kirchartz, M. B. Schubert, and J. H. Werner, *21 % efficient Si solar cell with a low-temperature a-Si:H/ZnO back contact*, in Proc. 15^{th} Intern. Photovolt. Sc. & En. Conv., edited by Y. Qinghao (Shanghai Scientific & Technical Publishers, China, 2005) p. 214

13. P. J. Rostan, C. Berge, U. Rau, and J. H. Werner, *Epitaxial mono-crystalline Si thin-films grown on self standing porous Si seed layers for solar cells*, in Proc. 15^{th} Intern. Photovolt. Sc. & En. Conv., edited by Y. Qinghao (Shanghai Scientific & Technical Publishers, China 2005) p. 630

14. P. J. Rostan, U. Rau, V. X. Nguyen, T. Kirchartz, M. B. Schubert, and J. H. Werner, *21 % efficient Si solar cell using a low-temperature a-Si:H back contact*, in Proc. 15th Workshop on Crystalline Silicon Solar Cells and Modules: Materials and Processing, edited by B. L. Sapori (NREL Report Nr. BK-520-38573, Golden CO, 2005) p. 214

15. O. Tobail, P. Khanna, J. Rostan, K. Brenner, M. B. Schubert, and J. H. Werner, in Proc. 2nd International Conference on Advances in Eng. Sciences and Technologies, Cairo, Egypt (2005) p. 96

16. P. J. Rostan, J. Mattheis, G. Bilger, U. Rau and J. H. Werner, Formation of transparent and Ohmic ZnO:Al/$MoSe_2$ Contacts for Bifacial Cu(In,Ga)Se_2 Solar Cells and Tandem Structures, Thin Solid Films, **480/481**, 67 (2005)

17. J. Mattheis, P. J. Rostan, U. Rau, and J. H. Werner, *Carrier collection in Cu(In,Ga)Se_2 solar cells with transparent ZnO:Al back contacts*, in Technical Digest of the 14th international Photovoltaic Science and Engineering Conference, edited by K. Kirtikara (Thailand, Bangkok, 2004) p. 593

Bibliography

[1] M. Tanaka, M. Taguchi, T. Matsuyama, T. Sawada, S. Tsuda, S. Nakano, H. Hanafusa, and Y. Kuwano, Jap. J. Appl. Phys. **31**, 3518 (1992).

[2] M. Taguchi, K. Kawamoto, S. Tsuge, H. Baba, T. Sataka, M. Morizane, K. Uchihasi, N. Nakamura, S. Kyiama, and O. Oota, Prog. Photovolt.: Res. Appl. **8**, 503 (2000).

[3] M. Tanaka, S. Okamoto, S. Tsuge, and S. Kiyama, in *Proc. 3rd World Conf. Photovolt. En. Conv.*, edited by K. Kurosawa, L. Kazmerski, B. McNellis, C. Wronski, and W. Sinke (Arisumi Printing, Japan, 2003), p. 955.

[4] N. Jensen, R. M. Hausner, R. B. Bergmann, J. H. Werner, and U. Rau, Prog. Photovolt.: Res. Appl. **10**, 1 (2002).

[5] K. von Maydell, H. Windgassen, W. A. Nositschka, U. Rau, P. J. Rostan, J. Henze, J. Schmidt, M. Scherff, W. Fahrner, D. Borchert, S. Tardon, R. Brüggemann, H. Stiebig, and M. Schmidt, in *Proc. of the 20th Europ. Photovolt. Solar En. Conf.*, edited by P. W.Palz, H. Ossenbrink (WIP Renewable Energies, München, 2005), p. 822.

[6] S. E. C. Limited, *HIT Photovoltaic Module*, Promotion Leaflet (2006).

[7] T. H. Wang, E. Iwnaiczko, M. R. Page, D. H. Levi, Y. Yan, V. Yelundur, H. M. Branz, A. Rothagi, and Q. Wang, in *Proc. 4th World Conf. Photovolt. En. Conv.* (IEEE, New York, 2006), p. 1439.

[8] K. Yamamoto, M. Yoshimi, T. Suzuki, T. Nakata, T. Sawada, A. Nakajima, and K. Hayashi, in *Proc. 28th IEEE Photovolt. Spec. Conf.* (IEEE, New York, 2001), p. 1428.

[9] L. E. Antonuk, J. Yorkston, W. Huang, J. Boudry, E. J. Morton, and R. A. Street, in *Proc. SPIE Vol. 1896* (IEEE, Bellingham, 1993), p. 18.

[10] P. Würfel, *Physik der Solarzellen* (Spektrum Verlag, Heidelberg, 2000).

[11] J. Nelson, *The Physics of Solar Cells* (Imperial College Press, London, 2003).

[12] P. Würfel, Physica E **14**, 18 (2002).

[13] P. Würfel, *Physik der Solarzellen* (Spektrum Verlag, Heidelberg, 2000), p. 102.

[14] U. Rau, G. Kron, and J. H. Werner, J. Phys. Chem B **107**, 13547 (2003).

[15] T. Tiedje, E. Yablonovitch, G. D. Cody, and B. G. Brooks, IEEE Trans. Electr. Devices **ED-31**, 711 (1984).

[16] M. A. Green, IEEE Trans. El. Dev. **ED-31**, 671 (1984).

[17] W. Heywang and K. Zaininger, in *Silicon: Evolution and Future of a Technology*, edited by P. Siffert and E. Krimmel (Springer-Verlag, Berlin, 2004), pp. 25–46.

[18] J. Dziewior and W. Schmid, Appl. Phys. Lett. **31**, 346 (1977).

[19] W. Shockley and W. T. Read, Phys. Rev. **87**, 835 (1952).

[20] R. N. Hall, Phys. Rev. **87**, 387 (1952).

[21] N. Jensen, *Heterostruktursolarzellen aus amorphem und kristallinem Silizium*, Ph.D. thesis, Universität Stuttgart (2001), pp. 44–46.

[22] T. Kirchartz, *Reciprocity between electroluminescent and photovoltaic action of solar cells - Theory and Experiments*, Diploma Thesis, Universität Stuttgart (2007).

[23] N. Jensen, U. Rau, and J. H. Werner, Mat. Res. Soc. Symp. Proc. **609**, A.13.1.1 (2000).

[24] M. Farrokh, R. Baroughi, R. Jeyakumar, Y. Vygranenko, F. Khalvati, and S. Sivoththaman, J. Vac. Sci. Technol. A **22**, 1015 (2004).

[25] O. von Roos and T. Landsberg, J. Appl. Phys. **57**, 4746 (1985).

[26] R. Brendel, M. Hirsch, R. Plieninger, and J. H. Werner, IEEE Trans. Electron Devices **43**, 1104 (1996).

[27] P. A. Basore, in *Proc. 23rd IEEE Photovolt. Spec. Conf.* (IEEE, New York, 1993), p. 147.

[28] M. Spiegel, B. Fischer, S. Keller, and E. Bucher, in *Proc. 28th IEEE Photovolt. Spec. Conf.* (IEEE, New York, 2000), p. 311.

[29] S. Kolodinski, J. H. Werner, T. Wittchen, and H. J. Queisser, Appl. Phys. Lett. **63**, 2405 (1993).

[30] H. J. Hovel, in *Semiconductors and Semimetals*, edited by R. K. Willardson and A. C. Beer (Academic Press, New York, 1975), vol. 11, p. 25.

[31] D. K. Schröder, IEEE Trans. El. Dev. **44**, 160 (1997).

[32] R. A. Sinton and A. Cuevas, Appl. Phys. Lett. **69**, 2510 (1996).

[33] W. Warta, Phys. Stat. Solidi **203**, 732 (2006).

[34] K. Orgassa, *Coherent optical analysis of the ZnO/CdS/Cu(In,Ga)Se_2 thin film solar cell*, Ph.D. thesis, Universität Stuttgart (2004), pp. 114–116.

[35] R. Swanepoel, J. Phys. E: Sci. Instrum. **16**, 1214 (1983).

[36] B. G. Yoon, C. Lee, and J. Jang, J. Appl. Phys. **60**, 673 (1986).

[37] W. Beyer and H. Overhof, Semicond. and Semimet. **21**, 257 (1984).

[38] G. Bruno, P. Capezzuto, and A. Madan, *Plasma deposition of amorphous silicon-based materials* (Academic Press, Burlington, MA, 1995), p. 4.

[39] F. B. Ellis, R. G. Gordon, W. Paul, and B. G. Yacobi, J. Appl. Phys. **55**, 4309 (1984).

[40] S. R. Kurtz, J. Proscia, and R. G. Gordon, J. Appl. Phys. **59**, 249 (1986).

[41] C. Koch, *Niedertemperaturabscheidung von Dünnschichtsilizium für Solarzellen auf Kunststofffolien*, Ph.D. thesis, Universität Stuttgart (2002), p. 110.

[42] R. C. Chittick, J. H. Alexander, and H. F. Sterling, J. Electrochem. Soc. **116**, 77 (1969).

[43] G. Bilger, *Präparation und Dotierung von amorphem Silizium durch die Kathodenzerstäubung*, Ph.D. thesis, Universität Stuttgart (1992), p. 16.

[44] T. Tiedje, B. Abeles, D. L. Morel, T. Moustakas, and C. R. Wronski, Appl. Phys. Lett. **36**, 695 (1980).

[45] E. Vallat-Sauvain, U. Kroll, J. Meier, A. Shah, and J. Pohl, J. Appl. Phys. **87**, 3137 (2000).

[46] H. Fritzsche, Solar En. Mat. **3**, 447 (1980).

[47] H. Overhof and P. Thomas, *Electronic Transport in Hydrogenated Amorphous Semiconductors* (Springer-Verlag, Berlin, 1989).

[48] R. A. Street, *Hydrogenated Amorphous Silicon* (Cambridge University Press, Cambridge, 1991).

[49] G. M. Ferreira, C. Chen, R. J. Koval, J. M. Pearce, C. R. Wronski, and R. W. Collins, J. Non-Cryst. Solids **338-340**, 694 (2004).

[50] J. Perrin, P. R. Cabarrocas, B. Allain, and J. M. Friedt, Jap. J. Appl. Phys. **27**, 2041 (1988).

[51] A. Matsuda, J. Non-Cryst. Solids **59**, 767 (1983).

[52] J. Meier, R. Flückiger, H. Keppner, and A. Shah, Appl. Phys. Lett. **65**, 860 (1994).

[53] L. Houben, *Plasmaabscheidung von mikrokristallinem Silizium: Merkmale der Mikrostruktur und deren Deutung im Sinne von Wachstumsvorgängen*, Ph.D. thesis, Heinrich-Heine-Universität Düsseldorf (1998), p. 25.

[54] J. H. Kerspe, F. Braunschweig, P. Flecher, W. Juhr, J. G. Lentges, G. Reich, F. Schittko, F. Tinner, and W. Umrath, *Vakuumtechnik in der industriellen Praxis* (expert-verlag, Ehningen, 1993), pp. 322–330.

[55] A. Al Tarabsheh, *Amorphous silicon solar cells*, Ph.D. thesis, Universität Stuttgart (2007).

[56] M. Zeman, J. v. d. Heuvel, B. Pieters, M. Kroon, and J. Willemen, *Advanced Semiconductor Analysis*. TU Delft, handbook (2003).

[57] G. W. Neudeck and A. K. Malhotra, J. Appl. Phys **46**, 239 (1975).

[58] R. Platz, *Amorphous silicon for optimized multi-junction Solar cells: Materials study an cell design* (UFO Atelier für Gestaltung & Verlag GbR, Konstanz, 1999), p. 34.

[59] S. Wieder, *Amorphous silicon solar cells: Comparison of p-i-n and n-i-p structures with zinc-oxide front contact*, Ph.D. thesis, Forschungszentrum Jülich (1999), p. 9.

[60] W. E. Spear and P. G. Le Comber, Solod State Comm. **17**, 1193 (1975).

[61] C. C. Tsai, Phys. Rev. B **19**, 2041 (1979).

[62] R. A. Street, D. K. Biegelsen, and J. C. Knights, Phys. Rev. Lett. **49**, 1187 (1982).

[63] R. A. Street, J. Zesch, and M. J. Thompson, Appl. Phys. Lett. **43**, 672 (1983).

[64] K. Pierz, W. Fuhs, and H. Mell, Phil. Mag. B **63**, 123 (1991).

[65] J. A. Reimer, R. W. Vaughan, and J. C. Knights, Phys. Rev. B **24**, 3360 (1981).

[66] W. E. Spear, D. Allan, P. Le Comber, and A. Ghaith, J. Non-Cryst. Solids **35 & 36**, 357 (1980).

[67] A. G. Aberle, Prog. Photovolt.: Res. Appl. **8**, 473 (2000).

[68] J. Y. Lee and S. W. Glunz, Solar En. Mat. & Solar Cells **90**, 82 (2006).

[69] W. Brendle, V. X. Nguyen, A. Grohe, E. Schneiderlöchner, U. Rau, G. Palfinger, and J. H. Werner, Prog. Photovolt.: Res. Appl. **14**, 653 (2006).

[70] W. Brendle, *Niedertemperaturrückseitenprozess für hocheffiziente Siliziumsolarzellen*, Ph.D. thesis, Universität Stuttgart (to be published).

[71] J. Schmidt, M. Kerr, and A. Cuevas, Semicond. Sci. Technol. **19**, 164 (2001).

[72] I. Martín, M. Vetter, A. Orpella, J. Puigdollers, A. Cuevas, and R. Alcubilla, Appl. Phys. Lett. **79**, 2199 (2001).

[73] S. Dauwe, J. Schmid, and R. Hezel, in *Proc. 29th IEEE Photovolt. Spec. Conference* (IEEE, New York, USA, 2002), p. 1246.

[74] A. Froitzheim, K. Brendel, L. Elstner, W. Fuhs, and M. Schmidt, J. Non-Cryst. Solids **299-302**, 663 (2002).

[75] I. Martín, M. Vetter, A. Orpella, C. Voz, J. Puigdollers, R. Alcubilla, A. V. Kharchenko, and P. Roca, Appl. Phys. Lett. **84**, 1474 (2004).

[76] M. Garín, U. Rau, W. Brendle, I. Martín, and R. Alcubilla, J. Appl. Phys. **98**, 093711 (2005).

[77] S. Olibet, E. Vallat-Sauvain, and C. Ballif, in *Proc. of the 21th Europ. Photovolt. Solar En. Conf.*, edited by W. Palz, H. Ossenbrink, and P. Helm (WIP Renewable Energies, München, 2006), p. 1366.

[78] R. Stangl, A. Froitzheim, M. Schmidt, and W. Fuhs, in *Proc. 3rd World Conf. Photovolt. En. Conv.*, edited by K. Kurosawa, L. Kazmerski, B. McNellis, C. Wronski, and W. Sinke (Arisumi Printing, Japan, 2003), p. 1005.

[79] A. B. Sproul, J. Appl. Phys. **76**, 2851 (1994).

[80] H. Haverkamp, Personal communication (2007).

[81] T. H. Wang, E. Iwnaiczko, M. R. Page, D. H. Levi, Y. Yan, V. Yelundur, H. M. Branz, A. Rothagi, and Q. Wang, in *Proc. 31st IEEE Photovolt. Spec. Conf.* (IEEE, New York, 2005), p. 955.

[82] W. Kern, J. Electrochem. Soc. **137**, 1887 (1990).

[83] C. C. Tsai and H. Fritsche, Solar En. Mat. **1**, 29 (1979).

[84] D. K. Biegelsen, R. A. Street, C. C. Tsai, and J. C. Knights, Phys. Rev. B **20**, 4839 (1979).

[85] C. Spinella, S. Lombardo, and F. Priolo, J. Appl. Phys. **84**, 5383 (1998).

[86] U. Rau, V. X. Nguyen, J. Mattheis, M. Rakhlin, and J. H. Werner, in *Proc. 3rd World Conf. Photovolt. En. Conv.*, edited by K. Kurosawa, L. Kazmerski, B. McNellis, C. Wronski, and W. Sinke (Arisumi Printing, Japan, 2003), p. 1124.

[87] S. De Wolf and G. Beaucarne, Appl. Phys. Lett. **88**, 022104 (2006).

[88] I. Sakata, M. Yamanaka, and R. Shimokawa, Jap. J. Appl. Phys. **44**, 7332 (2005).

[89] P. J. Cousins, D. H. Neuhaus, and D. E. Cotter, J. Appl. Phys. **95**, 1854 (2003).

[90] M. Schaper, J. Schmidt, H. Plagwitz, and R. Brendel, Prog. Photovolt.: Res. Appl. **13**, 381 (2005).

[91] H. Plagwitz, M. Nerding, N. Ott, H. P. Strunk, and R. Brendel, Prog. Photovolt.: Res. Appl. **12**, 47 (2004).

[92] J. Maier, *Gesputterte und aus der Gasphase abgeschiedene a-Si:H Schichten für a-Si:H/c-Si Heterosolarzellen*, Diplomarbeit, Universität Stuttgart (2006).

[93] E. Schneiderlöchner, R. Preu, R. Ludemann, and S. W. Glunz, Prog. Photovolt.: Res. Appl. **10**, 29 (2002).

[94] A. W. Blakers, A. Wang, A. M. Milne, J. Zhao, and M. A. Green, Appl. Phys. Lett. **55**, 1363 (1989).

[95] M. A. Green, Solid-State Electronics **20**, 265 (1977).

[96] J. M. Essick and J. D. Cohen, Appl. Phys. Lett. **58**, 1232 (1989).

[97] M. Sebastiani, L. Di Gaspare, G. Capellini, C. Bittencourt, and F. Evangelisti, Phys. Rev. Lett. **75**, 3352 (1995).

[98] C. G. Van de Walle and L. Yang, J. Vac. Sci. Technol. B **13**, 1635 (1995).

[99] J. Schäfer, J. Ristein, S. Miyazaki, and L. Ley, J. Vac. Sci. Technol. A **15**, 408 (1997).

[100] Y. J. Song, M. R. Park, E. Guliants, and W. A. Anderson, Solar En. Mat. & Solar Cells **64**, 225 (2000).

[101] F. Einsele and U. Rau, Personal communication (2006).

[102] M. J. Thompson, N. M. Johnson, R. J. Nemanich, and C. C. Tsai, Appl. Phys. Lett. **39**, 274 (1981).

[103] M. Vukadinovíc, F. Smole, M. Topič, R. E. I. Schropp, and F. A. Rubinelli, J. Appl. Phys. **96**, 7289 (2004).

[104] E. A. Schiff, R. I. Devlen, H. T. Grahn, and J. Tauc, Appl. Phys. Lett. **54**, 1911 (1989).

[105] G. Juska, K. Arlauskas, J. Kocka, M. Hoheisel, and P. Chabloz, Phys. Rev. Lett. **75**, 2984 (1995).

[106] M. Hirsch, U. Rau, and J. H. Werner, Solid-State Electronics **38**, 1009 (1995).

[107] W. Warta, S. W. Glunz, J. Dicker, and J. Knobloch, Prog. Photovolt.: Res. Appl. **8**, 465 (2000).

[108] J. H. Werner, Appl. Phys. A. **47**, 291 (1988).

[109] T. Kirchartz, *Analyse von Heterosolarzellen aus amorphem und kristallinem Silizium*, Studienarbeit, Universität Stuttgart (2005).

[110] A. G. Aberle, S. R. Wenham, and M. A. Green, in *Proc. 23rd IEEE Photovolt. Spec. Conf.* (IEEE, New York, 1993), p. 133.

[111] M. Scherff, H. Wingassen, Y. Ma, H. Stiebig, and W. R. Fahrner, in *Proc. 15th Intern. Photovolt. Sc. & En. Conv.*, edited by Y. Qinghao (Shanghai Scientific & Technical Publishers, China, 2005), p. 991.

[112] T. Müller, Y. L. Hunag, M. Scherff, and W. R. Fahrner, in *Proc. 15th Intern. Photovolt. Sc. & En. Conv.*, edited by Y. Qinghao (Shanghai Scientific & Technical Publishers, China, 2005), p. 367.

[113] A. Orpella, M. Vetter, R. Ferrè, I. Martìn, J. Puigdollers, C. Voz, and R. Alcubilla, Solar En. Mat. & Solar Cells **87**, 667 (2004).

[114] A. G. Ulyashin, R. Job, M. Scherff, M. Z. Gao, W. R. Fahrner, D. Lyebyedyev, N. Roos, and H. C. Scheer, Thin Solid Films **403**, 359 (2002).

[115] Y. Xu, Z. H. Hu, H. W. Diao, Y. Cai, S. B. Zhang, X. B. Zeng, H. Y. Hao, X. B. Liao, E. Fortunato, and R. Martins, J. Non-Cryst. Solids **352**, 1972 (2006).

[116] G. Garcia-Belmonte, J. García-Cañadas, I. Mora-Seró, J. Bisquert, V. Cristóbal, J. Puigdollers, and R. Alcubilla, Thin Solid Films **514**, 254 (2006).

[117] B. Jagannathan, W. A. Anderson, and J. Coleman, Solar En. Mat. & Solar Cells **46**, 289 (1997).

[118] N. Jensen, U. Rau, R. M. Hausner, S. Uppal, L. Oberbeck, R. B. Bergmann, and J. H. Werner, J. Appl. Phys. **87**, 2639 (2000).

[119] M. Geiger, *Strom/Spannungs- und Kapazitäts/Spannungs-Analyse an a-Si:H/c-Si Heterosolarzellen*, Studienarbeit, Universität Stuttgart (2005).

[120] S. Olibet, Personal communication (2006).

[121] K. von Maydell, E. Conrad, and M. Schmidt, Prog. Photovolt.: Res. Appl. **14**, 289 (2006).

[122] K. von Maydell, L. Korte, A. Laades, S. R., E. Conrad, F. Lange, and M. Schmidt, J. Non-Cryst. Solids **352**, 1958 (2006).

[123] D. Muñoz, C. Voz, M. Fonrodona, I. Martín, A. Orpella, M. Vetter, J. Puigdollers, R. Alcubilla, D. Soler, J. Escarre, J. Bertomeu, and J. Andreu, in *Proc. of the 20th Europ. Photovolt. Solar En. Conf.*, edited by P. W. Palz, H. Ossenbrink (WIP Renewable Energies, München, 2005), p. 996.

[124] S. Taira, Y. Yoshimine, B. Toshiaki, M. Taguchi, H. Kanno, T. Kinoshita, H. Sakata, E. Maruyama, and M. Tanaka, in *Proc. of the 22nd Europ. Photovolt. Solar En. Conf.*, edited by W. Palz, H. Ossenbrink, and P. Helm (WIP Renewable Energies, München, 2007), p. in print.

[125] C. Ehling, Personal communication (2007).

[126] P. J. Rostan, S. Keller, A. Hauser, J. Haase, I. Melnyk, P. Fath, A. Eder, A. Pollak, R. Hendel, and H. N. Nussbaumer, in *Proc. of the 22nd Europ. Photovolt. Solar En. Conf.*, edited by W. Palz, H. Ossenbrink, and P. Helm (WIP Renewable Energies, München, 2007).

[127] O. S. Heavens, *Optical Properties of Thin Solid Films* (Butterworths, London, 1955), p. 69.

Acknowledgement

Last but not least I would like to express my gratitude to:

- Prof. Dr. Jürgen H. Werner for giving me the opportunity to make my PhD at the *ipe*. Looking back at my time at his institute, I have to admit that the drill was a quite valuable experience. Every time when I read a publication or when one of my colleagues gives me a report I think: "Oh my goodness, this is not a right table!" or "Oh dear, what a bad graph!" I am happy in such moments for what I learned at the *ipe*. When I have to listen to speeches and talks accompanied by slides I also think back to to my Jürgen-H.-Werner-school attendance. I learned a lot about how to prepare slides, how to hold a speech and how to guide the listeners. It is no surprise, that *ipe* talks at conferences are qualitatively always amongst the best. Besides of what I learned form Jürgen H. Werner, I appreciate very much that I had heaps of freedom for my work and excellent working conditions.

- Prof. Dr. Uwe Rau for being my tutor. So far, I don't know anybody with a comparable combination of genuine physical and social skills. At times when I questioned my work and when I thought about quitting my PhD he always had the right words to make me continue with delight. Without his help, I would have never been able to get such a deep insight into semiconductor physics. Besides, without his commitment of being my tutor I would have never started with my PhD. So, I take a very very deep bow for Uwe Rau who is now Professor at the University of Aachen. Kudos to you or in German ein dreifaches Hoch! Hoch! Hoch! auf den Meister.

- Julian Mattheis for showing me how to slide on handrails at Q-Cells parties. Julian helped me a lot with programming simulations and with his theoretical

background knowledge. I am very happy that I got to know him at the *ipe* and he is now a very good friend of mine. I appreciate his manner to take the things easy. Stay cool, Julian!

- Thomas Kirchartz for supporting me with theoretical knowledge. His work during the Studienarbeit boosted my understanding of a-Si:H/c-Si heterojunctions. I am very glad that he helped me a lot even after his Studiearbeit was finished! From the physical understanding he directly follows the master. Thus, I take another bow for Thomas. Hats off!

- Dr. Gerhard Bilger for fruitful discussions and his magic all-repairing hands that work, work and work, no matter what day- or nighttime.

- Werner Wille for always providing amusement and excellent IT support. I am deeply sad that this extremely decent fellow got sick now. Werner, my best wishes for you and I very much hope that you'll soon get well.

- Brigitte Lutz, Leo Bauer, Anton Riss and Christiane Köhler for excellent technical support.

- Dr. Willi Brendle for excellent teamwork concerning high-efficiency back contacts.

- Viet Nguyen for performing heaps of measurements and depositions.

- Thomas Kirchartz, Matthias Geiger and Johannes Maier for their great work and for choosing me as their tutor.

- Florian Einsele and Christian Ehling for continuing the work on a-Si:H/c-Si heterostructures.

- Dr. Christine v. Rekowski, Lydia Gräter and Isabel Kessler for great administration.

- Thomas Schlötzer for introducing me into the secrets of wine tasting.

- All other *ipe* students, especially Dr. Gerda Gläser, Dr. Thomas Schlenker, Dr. Christopher Berge, Dr. Peter Grabitz, Caroline Carlsson, Ainhoa Esturo-Breton, Mawuli Ametowobla, Lorenz Eisenmann, Dr. Viktor Laptev as well

as all the newbies for the great *ipe* spirit and lots of intense social activities (please, don't think too far below the belt here...).

Erklärung

Hiermit erkläre ich, dass ich die vorliegende Dissertation "a-Si:H/c-Si heterojunction front- and back contacts for silicon solar cells with p-type base" selbständig verfasst und nur die angegebenen Hilfsmittel verwendet habe.

Stuttgart, den 31.10.2010

Philipp Johannes Rostan